TECHNICAL INNOVATIONS IN GRADIENT ARRAY SYSTEMS FOR MRI APPLICATIONS

A DISSERTATION SUBMITTED TO

THE GRADUATE SCHOOL OF ENGINEERING AND SCIENCE

OF BILKENT UNIVERSITY

IN PARTIAL FULFILLMENT OF THE REQUIREMENTS FOR

THE DEGREE OF

DOCTOR OF PHILOSOPHY

IN

ELECTRICAL AND ELECTRONICS ENGINEERING

By

Reza Babaloo

February 2023

TECHNICAL INNOVATIONS IN GRADIENT ARRAY SYSTEMS FOR MRI APPLICATIONS

By Reza Babaloo

February 2023

We certify that we have read this dissertation and that in our opinion it is fully adequate, in scope and in quality, as a dissertation for the degree of Doctor of Philosophy.

Ergin Atalar(Advisor)

Hitay Özbay

Behçet Murat Eyüboğlu

Emine Ulkü Sarıtaş Çukur

Emre Kopanoğlu

Approved for the Graduate School of Engineering and Science:

Orhan Arıkan
Director of the Graduate School

ABSTRACT

TECHNICAL INNOVATIONS IN GRADIENT ARRAY SYSTEMS FOR MRI APPLICATIONS

Reza Babaloo
Ph.D. in Electrical and Electronics Engineering
Advisor: Ergin Atalar
February 2023

In Magnetıc Resonance Imaging, gradient array coils have lately been employed in a variety of applications, such as field profiling. This capability of array technology can be used to minimize electric fields induced by gradient waveforms. For this purpose, a whole-body gradient array with all three gradients is being investigated. Gradient current amplitudes are optimized to produce a target magnetic field within a desired region of linearity (ROL) while minimizing induced electric fields. By reducing the diameter of ROL, generating a target gradient within a slice, and relaxing the linearity error, array coil electric fields are significantly reduced compared to a conventional coil. When a linear gradient is required in a small region, higher gradient strengths and slew rates can be achieved without exceeding peripheral nerve stimulation thresholds.

Because of a high number of channels in the array design, feedback controllers significantly raise the system cost due to the expensive current sensors used for gradient current measurements. Thus, a nonlinear second-order feed-forward controller is introduced for the gradient array chain. The feed-forward controller is then modified to update the controller coefficients based on thermal behavior prediction to deal with time-varying parameters caused by temperature-dependent resistances. Gradient current measurements and MRI experiments are conducted to show the effectiveness of the proposed method.

In the scope of this thesis, novel applications and hardware solutions are proposed to make array technology valuable and feasible.

Keywords: Gradient array, Nonlinear characterization, Feed-forward controller, Droop compensation, Field Optimization, Adjustable region of linearity, Minimum electric field, Peripheral nerve stimulation.

ÖZET

MR UYGULAMALARI İÇİN GRADYAN DİZİ SİSTEMLERİNDEKİ TEKNİK YENİLİKLER

Reza Babaloo
Elektrik ve Elektronik Mühendisliği, Doktora
Tez Danışmanı: Ergin Atalar
Şubat 2023

Manyetik Rezonans Görüntülemede gradyan sargı dizileri için son zamanlarda manyetik alan profili oluşturmak gibi birçok uygulama öne sürülüyor. Çoklu sargı dizilerini kullanmak sekansların tanımladığı gradyan manyetik alanın değişimiyle oluşan elektrik alanı an aza indirmede kullanılabilir. Bu amaç doğrultusunda bir tüm vücut sargı dizisi incelenmiştir. Çoklu sargıların belirli bir doğrusallık bölgesinde istenen manyetik alanı oluşturması için her bir sargıya verilmesi gereken en uygun akım değerleri hesaplanmıştır. Belirtilen doğrusallık bölgesini küçülterek, sadece bir kesit içerisinde bakılarak ve istenilen doğrusallıktan sapma değerini gevşeterek oluşan elektrik alanı halihazırda bulunan yöntemlere göre büyük bir ölçüde azaltmak mümkündür. Küçük bir alan içinde doğrusal gradyan manyetik alan istendiğinde periferik sinir stimülasyonu sınırlarına takılmadan daha yüksek bir gradyan şiddeti ve değişim hızı kullanılabilir.

Gradyan sargı dizilerinde geri beslemeli kontrol sistemi kullanmak, kullanılan yüksek kanal sayısı ve her kanalda olması gereken pahalı akım sensörleri sebebiyle sistemin toplam maliyetini büyük oranda arttırmaktadır. Bu sebeple doğrusal olmayan ikinci derece ileri beslemeli bir kontrol sistemi önerilmiştir. Bu metodun etkisini göstermek için gradyan sargıların akım ölçümleri ve manyetik rezonans görüntüleme (MRG) deneyleri yapılmıştır. Sistemdeki direnç parametreleri sıcaklığa bağlı ve dolaylı yoldan zamana bağlı olduğu için sistemin termal davranışı modellenmiş ve ileri beslemeli kontrol sistemi bu modele göre değiştirilmiştir.

Bu tezin kapsamında çoklu gradyan dizilerini daha değerli ve uygulanabilir kılmak için yeni uygulamalar ve donanım tabanlı çözümler öne sürülmüştür.

Anahtar sözcükler: Gradyan dizisi, Doğrusal olmayan tanımlama, İleri beslemeli kontrolör, Droop düzeltmesi, Alan optimizasyonu, Ayarlanabilir doğrusallık bölgesi, Minimum elektrik alanı, Periferik sinir stimülasyonu.

Acknowledgement

Although I am not comfortable condensing the priceless memories I have shared with amazing people into a few pages, I couldn't ignore the possibility that these pages will serve as a reminder of those memories for me and the people who supported me during my PhD training.

First and foremost, I'd like to express my heartfelt gratitude to Prof. Ergin Atalar. His enthusiasm for teaching and research has piqued my interest in learning how to teach and conduct research. His suggestions and contributions to my scientific, academic, and personal lives were outstanding. He was very supportive in personal matters and always pointed me in the right direction when I was lost. It was an honor to work with him. Thank you so much for everything.

I'd like to thank my jury members for devoting their valuable time to this dissertation and providing insightful feedback. Prof. Hitay Özbay and Prof. Behçet Murat Eyüboğlu were very gracious in attending my numerous committee meetings on short notice and continuously commenting on my work. I'd also like to thank Prof. Emine Ülkü Sarıtaş Çukur and Prof. Emre Kopanoğlu for their instructive feedback on this thesis.

I want to thank Süheyl Taraghinia, Manouchehr Takrimi, Volkan Açikel, Koray Ertan, and Ege Aydın for their assistance in completing my thesis. I thank my best friends, Bahram Khalichi, Alireza Sadeghi-Tarakameh, Ehsan Kazemivalipour, for their encouragement and contributions to both my academic and personal lives.

I am grateful to all UMRAM family for providing a productive research and social environment. Specifically, I thank Aydan Ercingöz and Elif Ünal for their patient attitude regarding administrative issues. I also thank Cemre Arıyürek, Said Aldemir, Bilal Taşdelen, Uğur Yılmaz, Mert Bozkurt, Ziba Arghiani, Abdullah Erkam Arslan, Mehmet Emin Öztürk, Elnaz Mahmoodi, Fatma Gül Uyar, and Metin Can Isık for being great group members.

The office life at UMRAM would have been too boring without Musa Aslandoğdu, Nurbanu Alparslan, Elif Bilge, and Berkay Giziroğlu. We had great coffee times and small talk sessions when we needed a break.

I'd like to thank my family for their unwavering support throughout my life.

Finally, I can't think of a way to thank my beloved wife, Fatemeh Babaloo. She is my constant source of joy. She has not only tolerated all of my stress, but she has also given me the power I require to move forward in life. Throughout my PhD studies, she has been by my side in both good and bad times. She has always supported me in every decision I have made and has always wanted the best for me.

I should stop here, but I'd like to thank other colleagues, friends, and family members for their assistance and support.

Contents

1 Introduction **1**

2 Minimum Electric Field Gradient Array Design **6**

2.1 Introduction 6

2.2 Background 9

2.3 Methods 11

2.3.1 Field calculations 11

2.3.2 First design: Z gradient only 12

2.3.3 Second design: X, Y, and Z gradients 13

2.3.4 Performance validation 15

2.4 Results 16

2.4.1 First design: Z gradient only 16

2.4.2 Second design: X, Y, and Z gradients 19

2.5 Discussion 24

3 Nonlinear Droop Compensation for Gradient Current Waveforms **27**

3.1 Introduction 27

3.2 Methods 29

3.2.1 Gradient Power Amplifier and PWM generation 29

3.2.2 Modified State-Space Averaging 30

3.2.3 Single-channel gradient system 32

3.2.4 Multi-coil gradient system 33

3.2.5 Control Architecture 35

3.2.6 SSA model and Feed-forward control simulations 37

3.2.7 Hardware setup 38

3.2.8 Gradient Current Measurements 39
3.2.9 MRI Experiments 40
3.3 Results 40
3.3.1 State Space Averaging method 40
3.3.2 Feed-forward control simulations 42
3.3.3 Gradient Current Measurements 43
3.3.4 MRI experiments 44
3.4 Discussion 46

4 Adaptive Feed-forward Control of Gradient Currents Using Gradient Heating Prediction 50
4.1 Introduction 51
4.2 Methods 51
4.2.1 First approach: Measuring the temperature 51
4.2.2 Second approach: Measuring electrical parameters 53
4.2.3 Controller implementation and MRI experiments 55
4.3 Results 56
4.4 Discussion 60

5 Discussion and Conclusion 61

A Digital Feedback Design for Mutual Coupling Compensation in Gradient Array System 76
A.1 Introduction 76
A.2 Methods 77
A.3 Results 79
A.4 Discussion 81

B Design and Implementation of High Switching Frequency Gradient Power Amplifier Using eGaN Devices 82
B.1 Introduction 82
B.2 Methods 83
B.3 Results 85
B.4 Discussion 85

List of Figures

2.1 Strength-duration curve. 9

2.2 PNS and hardware thresholds. 10

2.3 (**A**) Half of the X coil quarter (5 and 3 loops in a bundle for primary and shield, respectively). (**B**) Half of the Z coil. Both the primary and shield coils consist of 48 bundles with 5 loops per bundle. . . 14

2.4 Comparison of conventional and array coils. Both coils have almost similar performance. The current RMS for the conventional and array coils are 330A and 350A, respectively. 16

2.5 Comparison of spherical and disk-shaped ROLs. The linearity error for the spherical ROL is 4.2% and for the disk-shaped ROL is 2.1%. The currents RMS for the spherical and disk-shaped ROLs is 350A and 250A, respectively. 17

2.6 B-field and E-field of array coil when optimized for a disk-shaped ROL at $z = +75mm$ and $z = -75mm$. 18

2.7 Comparison of average induced E-fields within body volume. . . . 20

2.8 Comparison of gradient array and conventional coil. The maximum linearity error is the same for both designs; however, by using a slightly higher current RMS in the array coil, the maximum E-field is reduced for all three gradients. 21

2.9 The left column depicts the $|E|_{max}$ with respect to the linearity error. Conventional designs have almost perfect linearity in a small ROL (120mm). The gradient array coil can generate the desired gradient with the same linearity while the induced E-field is minimized. By optimizing the feeding current with different linearity errors, it is possible to reduce the E-fields even further. The right column displays the E-field for X, Y, and Z gradients (array) at a 5% linearity error. 23

2.10 E-field plots for all gradients when the linearity is required within a disk in the z-direction (20mm thickness). First row: disk at the iso-center, second row: the disk is shifted in the positive z direction. 24

2.11 Off-center oblique slice: the slice is chosen in X+Y axis (at 0.1m distance from the center with 40mm thickness), the other two can be used as phase encoding or readout direction. For the slice selection gradient there is a 36% increase in PNS thresholds. For the X-Y+Z and X-Y-2Z axes, PNS thresholds are increased by 22% and 21%, respectively. 25

3.1 (**A**) Full-bridge power amplifier configuration (**B**) The center-aligned approach for two periods of PWM. The waveforms for the high-side transistors (T_1 and T_3) are shown in the figure. The low-side transistors (T_2 and T_4) are switched with the complementary logic. 31

3.2 A single circuit variable (the inductor current, for example) time dependence over a period of PWM (T) with the PWM's on and off duration. The duty cycle, $d(n)$, is defined as the ratio of T_{on} to (T). 32

3.3 (**A**) single-channel gradient system circuit including amplifier, power supply with parallel decoupling capacitor, and the gradient coil. The green path shows the circuit during T_{on}, and the red one is for T_{off}. (**B**) PWMs for channel1 and channel2 assuming $d_1 > d_2$ and (**C**) Different states of two-channel system circuit which covers any combination of d_1, d_2. 34

3.4 (**A**) The overall gradient chain block diagram, including the feed-forward controller and different components of the gradient system. (**B**) Benchtop installation, which is located in the equipment room. (**C**) The imaging setup including gradient coil, RF coil, TR switch, and phantom. 37

3.5 Time response comparison of the topological model of gradient system (yellow) and the SSA model (purple). Red curve shows the average of topological model with ripples filtered out. (**A**) Constant duty cycle, $d = 0.5$. (**B**) Zoomed-view of a small region depicted by a square in panel A. The topological model average is precisely followed by the SSA model (normalized maximum error = 0.0012%). (**C**) Varying duty cycle (3kHz sinusoidal), and (**D**) Zoomed-view of the region specified by a square in panel C. Even in this case, varying duty cycle, the SSA gives an excellent approximation of the topological model (normalized maximum error = 0.16%). This error is duty cycle-dependent, and it increases as the duty cycle increases. The frequency of 3kHz (as an example) is used here, which is within the common range of gradient operation frequency. 41

3.6 Simulation results: (**A**) Calculated required duty cycles for linear first-order and nonlinear second-order models. (**B**) a zoomed-in view of the flat-top region, which clearly shows the difference between the output of linear and nonlinear controllers. (**C**) The gradient coil's current after applying the duty cycles acquired in (A). It demonstrates that the nonlinear controller compensates for the current droop over the flat top region. (**D**) a zoomed-in view of C for the flat-top period. 42

3.7 Experiment results. The comparison of the coils' currents generated using the linear and nonlinear models. The reference inputs are trapezoid waveforms with the amplitude of 50A and 10A for ch-1 and ch-2, respectively. Both channels have the same rise time ($200\mu s$). 43

3.8 Oscillations on the current after switching on/off the gradient coil inside the scanner (the red waveform). These oscillations are removed by using the gradient current transfer function and modifying the input waveform accordingly (the green one). 44

3.9 Phantom images acquired in the coronal plane using the GRE pulse sequence (single slice). The uncompensated and compensated images are taken by applying the currents provided with the linear and nonlinear models, respectively, as a readout gradient (in z direction, indicated by white arrow). The droop in the readout gradient when using the linear model results in image deformation (shrinking) indicated by yellow arrows. The normalized error images and the line profiles show a significant improvement in the image quality for the compensated image (acquired using the nonlinear model). 45

4.1 (**A**) the block diagram of gradient system with feed-forward controller, including the updating block. (**B**) Measurement setup. There are six temperature sensors; three of them measure the coil winding temperature, and the other three measure the ambient temperature. The average temperature is used in calculations. . . 52

4.2 The total system model that is separated by the electrical and thermal parts. All temperatures given are effective temperatures stemming from the lumped model. 54

4.3 Part of a single TR for a single slice of the multi-shot EPI pulse sequence used for imaging. The next shot for the same slice is scanned 156 ms later, making the effective TR for a single slice 156 ms. The next slice is scanned immediately after, which allows maximum use of the readout gradient. 55

4.4 Measured and predicted coil temperature are shown in (**A**), demonstrating the accurate prediction of coil temperature variations using the thermal equation. (**B**) depicts the coil current and resistance versus time when a constant voltage is applied to the coil, which indicates an exponentially increase in the resistance and consequently decrease in the current. 56

4.5 The red and green curves show the measured and predicted resistance, respectively. The difference between them is mainly due to the power amplifier heating, which is not considered in the prediction. Applying different current waveforms will result in different predictions; for example, a trapezoid (50A peak amplitude and 10% duty cycle) and EPI (±30A). 57
4.6 A 5-minute EPI waveform was applied to the coil, and the currents were captured at the start and end of the period. (**A**) show the currents without updating the coil resistance in the model, which results in a 17% reduction in the current amplitude after 5 minutes. Adding the updating feature will compensate for the reduction and provide the desired waveform during the operation period (**B**). . . 58
4.7 MRI experiment results without resistance prediction. 59
4.8 MRI experiment results with resistance prediction. 59

A.1 (**A**) the schematic of the gradient array system. A combination of feed-forward and feedback provides the desired voltage. Generated PWM signals will amplify and apply to the gradient coil. The analog data coming from the current sensor will be digitized and used in the feedback loop. (**B**) All the system can be shown by 3 transfer function blocks in the frequency domain. $G_p(s)$ contains all the analog part. $G_m(s)$ and $G_c(s)$ are the model of system and controller transfer functions, respectively. 78
A.2 Simulations: gradient coil current for feed-forward only, feedback only, and feed-forward+feedback controllers. 80
A.3 Experiments: gradient coil current for feed-forward only, feedback only, and feed-forward+feedback controllers. 80
A.4 Image simulations, ideal case and for each controller (first row), difference images (second row). 81

B.1 Simplified circuit diagram of 150V/50A half-bridge for gradient array applications using eGaN transistors. Two parallel transistors are used as a switching element. Two of these modules are used for one full bridge driver. 84

B.2 Circuit diagram and fabricated differential one stage LC filter. Cut-off frequency is about 50kHz to attenuate ripple current with 1MHz frequency. Capacitor values are decreasing towards our switching frequency which degrades attenuation ratio. 84

B.3 (**A**) Measured PWM signals at the input (bottom) and output (top) of the H-bridge with 150V supply without load at 1MHz effective switching frequency. (**B**) Temperature increase of GaN transistors to 38°C from room temperature for about five minutes of operation condition in (A). 85

B.4 (**A**) Measured trapezoidal current waveform with 50A flat top amplitude and 0.25A/μs slew rate with filter. (**B**) Temperature of eGaN transistors to 45°C from room temperature for the current on (A) with 10% duty cycle and five minutes of operation. Zoomed version of the current is shown in Figure B.5 86

B.5 Zoomed current (top) and voltage (bottom) applied to the coil without (**A**) and with (**B**) filter. Peak-to-peak ripple current is reduced more than twelve times by using the LC filter. Small resistance of the coil (about 200$m\Omega$) requires small voltage levels and PWM duty cycle. 86

List of Tables

2.1 Gradient coil performance values 19

2.2 PNS parameters ΔG_{min} (mT/m units) and SR_{min} (T/m/s units) 24

Chapter 1

Introduction

Magnetic Resonance Imaging (MRI) is a powerful non-invasive medical imaging modality that is primarily based on sensitivity to the presence and properties of water, which accounts for 70% to 90% of most tissues. Because the properties and amount of water in tissue can change substantially with disease and injury, MRI is a highly sensitive diagnostic technique. In its most advanced, MRI has the ability to image not only anatomy and pathology, but also organ function [1], in-vivo chemistry [2], and brain connectivity [3].

Magnetic field gradient coils, commonly abbreviated as "gradient coils" are used in MRI scanners to provide spatial encoding within an imaging volume. They are made up of formed conductors (wires or thin sheets) through which current flows to generate the gradient field. In conventional MRI, three independent orthogonal sets of gradient coils (X, Y, and Z) are present, each controlled by its own gradient amplifier. Time-varying gradient coil currents produce variation in the intensity of the static field B_0 in each direction (z component of the magnetic field). The spatial variation in B_0 causes a change in frequency of precessing spins, and these changes are used for the purposes of slice selection, frequency encoding, and phase encoding.

In modern MRI, high strength and high slew rate gradient coils are demanded for higher image quality and faster imaging. Higher maximum gradient strength (G_{max}) is essential for applications which require high amplitude gradient waveforms, such as diffusion weighted imaging (DWI). Higher G_{max} enables shorter diffusion gradients for a desired b-value, resulting in shorter echo times (TE), higher image SNR, and the possibility of higher spatial resolution or higher b-values [4]. A higher slew rate (SR) is desired to reduce acquisition time for applications such as echo planar imaging (EPI) [5]. Commonly used DWI sequences combine an EPI readout and faster SR translate to shorter echo spacings, resulting in increased SNR and less image distortion by mitigating motion artifacts.

Whole-body gradient coils have a G_{max} of less than 80 mT/m and a maximum SR of no more than 200 T/m/s. Because gradient coil inductance is proportional to the fifth power of coil radius, increasing G_{max} to higher than 80 mT/m necessitates significantly higher peak power (e.g., 8 MVA/axis to achieve 300 mT/m) [4, 6]. Despite this high-performance hardware, high G_{max} and high SR have not been achieved simultaneously due to physiologic limitations imposed by peripheral nerve stimulation (PNS) [7–11]. Rapid switching of strong magnetic fields (B-fields) induces electric fields (E-fields) within the human body, which may change the membrane voltage of a nerve fiber, resulting in nerve stimulation [12]. Therefore, the use of high-performance gradient coils has become significantly limited by PNS rather than hardware.

For the gradient coils design [13], some parameters must be considered during the design stage, such as gradient linearity error within a specific region, total inductance and power dissipation, torque and force, eddy current, and peripheral nerve stimulation. These parameters and field profiles cannot be changed after the gradient coils are manufactured; they can only be scaled by adjusting amplifier outputs.

Gradient array coils [14–17], also referred as “multi-coil gradients” [18–20] or “matrix gradient coils” [21, 22] have lately been employed in a variety of applications, including field profiling, simultaneous multi-slice excitation, local excitation, B_0 field shimming, and, in some cases, a combination of these. The gradient array is made up of multiple gradient coils that can be individually driven by independent gradient power amplifiers (GPAs). Gradient array coils can generate dynamically controllable magnetic field profiles within a customizable region of linearity (ROL), and the design parameters can be changed even after fabrication by adjusting the feeding currents.

The main motivations for this thesis are as follows: first, to increase PNS thresholds using gradient array technology. To this end, the current amplitudes of array elements are optimized to achieve a minimum E-field design while producing a target magnetic field profile. Minimum E-field design provides the opportunity to reach higher gradient strengths and slew rates without exceeding PNS thresholds. Second, to propose a new method for driving gradient array coils. Conventional gradient systems use closed-loop feedback controllers [23, 24], which require high-precision high-cost current sensors to track the command input precisely. Due to a high number of channels in an array design, feed-forward controllers might be preferable to avoid expensive current sensors. The proposed methods compensate for imperfections in the gradient hardware caused by GPAs and time-varying parameters.

The application of gradient array technology in minimization of the induced E-field, and thus, increasing PNS thresholds, is investigated in this thesis. The advantage of gradient arrays in field profiling and generating dynamically changeable gradients with different parameters within different shape ROL have already been demonstrated in the literature [14, 17]. The current amplitudes of an array coil can be optimized to generate a target magnetic field while reducing the induced E-fields. Firstly, we investigate a Z gradient array coil to exemplify the ability of array technology to reduce the E-fields. In this case, the optimization problem minimize the difference between the target and generated magnetic fields, and E-field thresholds are incorporated as a linear constraint alongside some other engineering constraints. Heterogeneous models are used for the E-field calculations. Secondly, a new optimization problem is introduced for a whole-body gradient array with all three gradients (X, Y, and Z). In this case, the optimization problem is defined as determining the amplitude of the currents so that the peak-induced electric field on the surface of a simplified body model is minimized while satisfying a set of constraints. Constraints are placed on the magnetic field at a set of points spanning the desired region of interest (desired gradient strength with specified linearity error), the maximum tolerable magnetic field at the cryostat, the maximum current that the hardware can supply, and torque. Minimum E-field design implies that higher gradient strengths and slew rates can be achieved without exceeding PNS thresholds if the required hardware is available.

In the continuation of this thesis, a nonlinear second-order model that includes the GPA and power supply is introduced for the gradient chain. Our aim is the investigation of nonlinearities associated with the GPA, and compensation for the imperfections of the GPA rather than those of the gradient coil. The state space averaging (SSA) method has been used in the literature [25–29] to model DC–DC power converters in a steady state linearized around an operating point. The modified SSA method is used to characterize the switching GPAs, both steady-state and transient behavior, by considering nonlinear equations. The accuracy of the SSA method primarily depends on the switching frequency of pulse width modulation (PWM) signals. In our case, this method is applicable because of high-switching PWM signals (1MHz). The digital inversion of the acquired model is then used in the feed-forward open-loop configuration to provide the required voltage to control the output gradient currents. Using a nonlinear controller compensates for the current droop in the plateau region of the trapezoidal gradient waveforms and provides slight corrections in the transients. As proof of concept, this study considers a Z gradient coil with two separate windings driven by two independent GPAs and power supplies. A nonlinear multi-input-multi-output feed-forward controller is applied. The output currents are measured for both linear and nonlinear controllers by applying a trapezoidal waveform at the input. Finally, MRI experiments are conducted to show the effectiveness of the proposed method.

To deal with the time-varying parameters of the gradient system, such as temperature-dependent resistances, an adaptive feed-forward controller is designed. The heating of the gradient system changes its characteristic, and without a feedback system, the gradient waveform distorts, resulting in image artifacts. The primary effect of temperature rise in the gradient coil winding is the increase in coil resistance. Feed-forward based controllers, preferable in gradient array systems and multi-coil designs, use a linear time-invariant model. However, the gradient heating makes the system time-variant. To address this issue, a method is proposed which predicts gradient coil thermal variation using the thermal differential equation and updates feed-forward controller parameters continuously. A second approach is introduced to consider the thermal variation of gradient coil windings and GPAs at the same time. The proposed methods are free from expensive current sensors, reducing the cost of the gradient array technology.

This thesis is organized as follows: Chapter 2 explains minimum electric field whole-body gradient array design, Chapter 3 investigates a new method for gradient system characterization and a nonlinear feed-forward controller for droop compensation of gradient waveforms, and Chapter 4 discusses gradient heating issues and how to design an adaptive feed-forward controller to compensate for time-varying parameters.

Chapter 2

Minimum Electric Field Gradient Array Design

Preface

Some contents of this chapter were presented at the Joint Annual Meeting of International Society for Magnetic Resonance in Medicine-European Society of Magnetic Resonance in Medicine and Biology [30]. The second design presented in this chapter was submitted and accepted for presentation at the Annual Meeting of International Society for Magnetic Resonance in Medicine in June 2023 [31]. Manouchehr Takrimi assisted in the calculation of torque matrix. The MATLAB code for generating the simplified body model is provided by Koray Ertan.

2.1 Introduction

The primary determinant of the peripheral nerve stimulation (PNS) thresholds for a given gradient coil is its region of linearity (ROL). A large ROL in whole-body gradient coils exposes large body areas to switching magnetic fields, leading to higher induced E-fields. Several short-body and dedicated head-insert gradient coils with small ROL were developed to increase gradient coils performance without causing PNS. For example, the compact 3T (C3T) head-gradient coil [32] can achieve a G_{max} of 80mT/m and 700T/m/s SR, the recently designed Microstructure Anatomy Gradient for Neuroimaging with Ultrafast Scanning (MAGNUS) gradient coil [33] can simultaneously provide 200mT/m G_{max} and 500T/m/s SR. Because these high-performance head gradient coils have a small ROL, they expose a smaller portion of the body to electromagnetic fields, allowing them to reach PNS thresholds at higher G_{max} and SR than whole-body gradient coils. These coils, however, are only intended for brain imaging, limiting their application. They also have concerns with active shielding, spatial linearity across the imaging field of view (FOV), and gradient heating.

PNS thresholds are evaluated after coil fabrication using experimental studies on healthy volunteers [34–36], which offer very limited perspectives into design modifications that may minimize PNS. Therefore, PNS characteristics have to be directly incorporated into the gradient coil design process. New gradient design algorithms were proposed to incorporate constraints on the E-fields, leading to PNS-optimized gradient coils. Davids et al. [37] introduced the PNS Oracle, which uses a coupled electromagnetic-neurodynamic model [12, 38] to relate the induced E-field to peripheral nerve activation. The PNS oracle was then integrated into the optimization process of gradient coil winding, allowing for the rapid assessment of thousands of candidate coil designs while iteratively approaching an optimal design with higher PNS thresholds. Roemer et al. [39] developed computationally efficient methods for evaluating the spatial distribution of E-fields over homogeneous body models with realistic dimensions, which were then integrated into the gradient coil optimization algorithm to achieve a minimum E-field gradient coil design [40].

Although these algorithms yield a PNS-optimized gradient coil, two critical issues remain unaddressed. First, engineering metrics such as ROL size and field linearity, hardware limits, eddy current, and torque are fixed parameters during the gradient coil design process and changing any of these parameters results in a different design and coil winding, which also affect PNS thresholds [11, 37].

Second, the PNS constraint is affected by the dimensions of the investigated body model as well as the body position inside the coil which is used for E-field calculations. For example, PNS thresholds differ between male and female body models, or when the design is optimized for head imaging but employed in a cardiac imaging body position, the improvements are reduced [41].

It has already been shown in the literature that additional coil elements [42,43] in the gradient coil configuration can increase the gradient performance while mitigating PNS issues, even after the coil has been manufactured. Recently introduced gradient array coils have been used for various applications and provide a higher degree of freedom for field profiling. In some applications such as DWI, the target ROL is limited to a single slice, and thus, no need to generate the gradients within a large region. Despite Conventional coils, array coils can provide target gradients with flexible linearity within an adjustable ROL by optimizing gradient current amplitudes. The winding patterns in the array design are fixed, but the driving currents can be adjusted based on the requirements of a particular scan. As a result, with a body-sized gradient array coil, it is possible to simultaneously achieve high G_{max} and SR without exceeding PNS thresholds, when the linear gradient is required in a small region.

In this chapter, we first look at how a Z gradient array coil can reduce induced E-fields on a heterogeneous body model by optimizing coil element currents. Then, we introduce a whole-body gradient array coil with all three gradients (X, Y, and Z), which can minimize the induced E-fields (maximize PNS thresholds) on a simplified body model surface while producing the target gradient. In each of the aforementioned cases, the optimization problem is different. In the first part, the maximum error between the target B-field and generated one is used as an objective function, while E-fields are considered in the constraints. In the second part, the objective function is the peak induced E-field, and B-fields are considered in the constraint. In both cases, the coil dimensions and winding patterns are fixed, while other engineering metrics, such as ROL, field linearity, torque, the magnetic field at the cryostat, and maximum applied current, are flexible.

2.2 Background

In MRI, rapidly changing magnetic fields of gradient coils can induce electric fields in human tissue, causing PNS. The human body nerves are at rest state in normal conditions, which means that there is a balance between the electric potential of the nerve axon intracellular and extracellular spaces [44]. However, if the electric field induced by the gradient coil exceeds a certain threshold, it can change the nerve membrane voltage, resulting in an action potential [44], which we call PNS. PNS is a sensation of tingling or tapping at certain exposure levels; however, patients may become uncomfortable or experience pain if exposed at levels higher than a threshold [8,10]. At extremely high levels, cardiac stimulation is also possible. However, the induction of cardiac stimulation [45] may occur at exceedingly large gradient fields (much higher than those currently used by commercially available MR scanners).

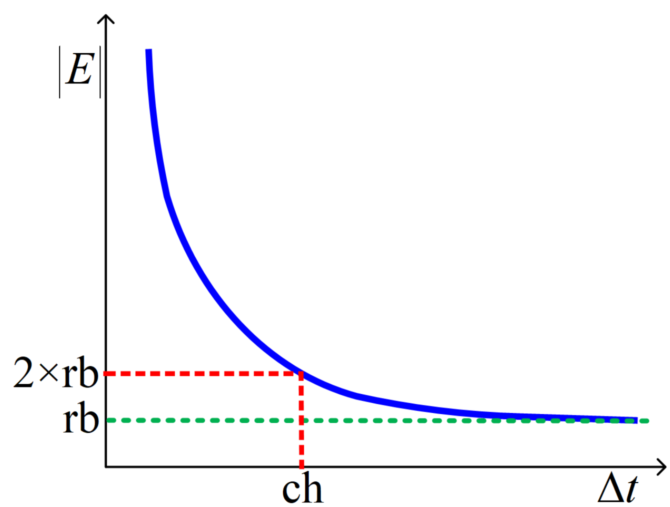

Figure 2.1: Strength-duration curve.

The IEC 60601-2-33 safety standard [46] specifies two methods for determining PNS thresholds: (1) computing PNS threshold parameters from peak E-fields on the surface of a uniform body model, and (2) experimental PNS measurements in human subjects. The E-field calculation method is based on a strength-duration relationship (Figure 2.1) that defines the minimum E-field applied for duration Δt. Rheobase (rb, minimum E-field to cause nerve stimulation) and chronaxie (ch, time constant for nerve stimulation) are PNS factors [39]. According to IEC regulations, rb $= 2.2$V/m and ch $= 360\mu$s can be used to determine PNS threshold from E-fields of body gradient coils. Converting the E-field strength-duration relationship to the linear magnetostimulation formula [47], where PNS metrics are given by intercept and slope, results in:

$$\Delta G_{stim} = \Delta G_{min} + \Delta \mathrm{t} SR_{min} \tag{2.1}$$

The PNS parameters ΔG_{min} and SR_{min} are the minimum gradient strength that causes stimulation at any switching time and the minimum slew rate that causes stimulation at any gradient strength, respectively, and are given by [47]:

$$\begin{aligned} \Delta G_{min} &= \frac{\mathrm{rb}}{E_{max}/SR}\mathrm{ch} \\ SR_{min} &= \frac{\mathrm{rb}}{E_{max}/SR} \end{aligned} \tag{2.2}$$

where E_{max}/SR is the maximum E-field per unit slew rate calculated on the body surface. Figure 2.2 shows PNS threshold and hardware limit of a body gradient coil.

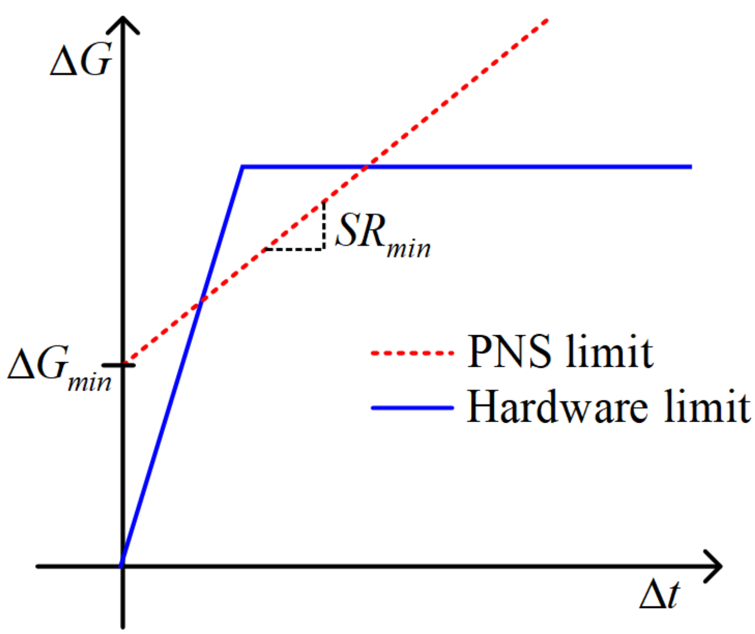

Figure 2.2: PNS and hardware thresholds.

2.3 Methods

2.3.1 Field calculations

In the array configuration, each channel is treated as a basis element. Therefore, the B-field profile and the induced E-field of each channel are computed when a unit current is applied to one of the channels while the others are zero. We use low-frequency magneto quasi-static solvers available in Sim4Life (Zurich MedTech, Switzerland) for field calculations. All calculations are performed with 1kHz sinusoidal currents. Given the linearity of Maxwell's equations, the total magnetic and electric fields can be expressed as a linear combination of basis elements.

For the B-fields, we combine the z component of magnetic field vectors at all sample points as columns of a matrix ($\mathbf{B}_{matrix}$). The total magnetic field then can be expressed as the product of this matrix and the feeding currents as follows:

$$B_{z,Total} = \mathbf{B}_{matrix} I = \begin{bmatrix} b_{z,1,1} & b_{z,1,2} & \cdots & b_{z,1,m} \\ b_{z,2,1} & b_{z,2,2} & \cdots & b_{z,2,m} \\ \vdots & \vdots & \ddots & \vdots \\ b_{z,n,1} & b_{z,n,2} & \cdots & b_{z,n,m} \end{bmatrix} \begin{bmatrix} i_1 \\ i_2 \\ \vdots \\ i_m \end{bmatrix} \tag{2.3}$$

where, $B_{z,n,m}$ is the magnetic field z component due to m^{th} coil at the n^{th} sample point.

For the E-fields, since the directions of electric field vectors are different at each sample point, the E-field matrices must be computed separately for each component of x, y, and z. The vector sum of these components multiplied by the currents yields the total E-field:

$$E_{Total} = \left(\mathbf{E}_x \hat{\imath} + \mathbf{E}_y \hat{\jmath} + \mathbf{E}_z \hat{k} \right) I \tag{2.4}$$

2.3.2 First design: Z gradient only

The Z gradient array coil is made up of primary and shield coils, each with 12 channels (10 wire loops per channel) and diameters/heights of 600/1000 and 750/1200mm, respectively. A conventional symmetric Z gradient coil (of the exact dimensions as the array coil) is designed with Sim4Life to provide a similar performance. For the E-field calculation, we use Duke ViP3 [48] heterogeneous body model including 305 tissues.

In conventional gradient coil designs, a set of arbitrary basis functions (for example, stream functions) with a particular shape and unknown amplitude are optimized to determine the efficient coil winding pattern [49]. In our case, the basis functions are an array of coils (channels) with a predefined winding pattern but unknown current amplitudes. The optimization problem is defined to minimize the maximum error between the desired B-field and generated one, subject to some linear constraints, as follows:

$$\begin{aligned} \min \quad & \|\mathbf{B}_{matrix}X - B_{desired}\|_\infty \\ \\ s.t. \quad & |\mathbf{B}_{cryostat}X| \leq B_c \\ & |\mathbf{E}_{Total}X| \leq E_{max} \\ & |X| \leq \ I_{max} \end{aligned} \tag{2.5}$$

where, vector X is the unknown current amplitudes of the Z coil, $\mathbf{B}_{cryostat}$ is a matrix of generated magnetic field on the cryostat (similar to $\mathbf{B}_{matrix}$), B_c is the maximum tolerable magnetic field on the cryostat, E_{max} is a threshold for maximum induced E-field, and I_{max} is the maximum current that gradient amplifiers can supply. To solve the optimization problem, “fmincon” function of MATLAB optimization toolbox is used. “fmincon” finds a constrained minimum of a scalar function of several variables starting at an initial estimate. This is generally referred to as constrained nonlinear optimization or nonlinear programming. The final solution is a local minimum that satisfies the constraints. We use interior-point algorithm with a random initial point and the optimization completes when the objective function is non-decreasing in feasible directions, to within the default value step tolerance.

2.3.3 Second design: X, Y, and Z gradients

This design employs a whole-body gradient array coil that is made up of X, Y, and Z gradients, including both the primary and shield coils. For the X gradient, we take a conventional coil winding (designed by Sim4Life MRI gradient coil feature) and break it down into multiple channels, which can be driven individually with different current amplitudes. The number of channels is chosen so that the total power consumption (volt $\times$ ampere) in the array design is comparable to that of the conventional design. Our aim is to drive the array coils with a series of low-cost gradient power amplifiers that are equivalent to a high-cost conventional power amplifier. Here, we consider a total of 96 channels (including primary and shield). As shown in Figure 2.3A, each quarter (out of 8 quarters) of the X coil (primary) is divided into 12 channels with 5 loops per channel. The Y gradient is configured in the same way. If the same current is applied to all channels, the X and Y array coils function as a conventional gradient coil. For the Z coil, the entire surface of the coil former is covered with circular loops uniformly spaced along the z axis. We assume that the Z gradient also has independent 96 channels in total. Figure 2.3B depicts half of the Z coil. The primary and shield arrays can be programmed to operate as a conventional Z gradient with the usual functionality. The diameter of X, Y, and Z primary coils are 690, 710, and 730mm, respectively.

For the E-field calculations of this case, we use the same family of body models introduced in [39]. From the six models representing the 2.5^{th}, 50^{th}, and 97.5^{th} percentile male and female adult populations, we choose the 50^{th} male model. It has already been demonstrated that PNS thresholds can be reliably predicted utilizing such simplified body models [39]. In our case, using this simplified upper body model (rather than heterogeneous body models) has a number of advantages. For example, because the model's interior electrical properties are uniform, the maximum induced E-field occurs on the surface of the body model. As a result, only the surface sample points need to be considered, which makes the E-field calculations computationally efficient.

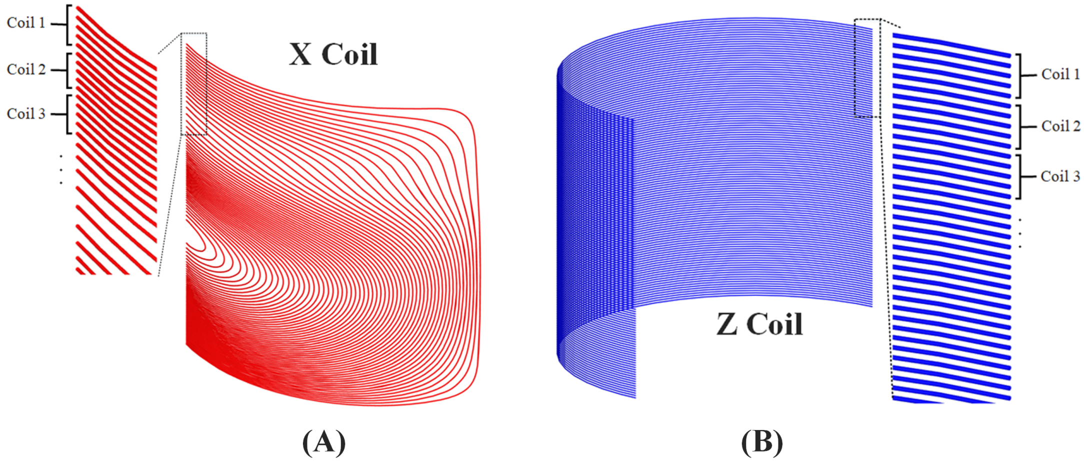

Figure 2.3: (**A**) Half of the X coil quarter (5 and 3 loops in a bundle for primary and shield, respectively). (**B**) Half of the Z coil. Both the primary and shield coils consist of 48 bundles with 5 loops per bundle.

The optimization problem is defined as determining the amplitude of the currents so that the peak induced electric field on the surface of the body model is minimized while satisfying a set of constraints. Constraints are placed on the desired magnetic field at a set of points spanning a specific region of interest (linearity error), the maximum tolerable magnetic field at the cryostat, the maximum current that the hardware can supply, and torque. The magnetic field on the cryostat is considered to incorporate eddy current issues. Although we only define a threshold here, advanced techniques that calculate total power dissipation in cryostat [50] can be used. Torque constraint is required for X and Y coils because when currents flow, they experience torque in a strong uniform magnetic field, which can cause vibrations.

Defining X as the vector of unknown coil currents, the optimization problem can be formulated as follows:

$$\begin{aligned} &\min \quad \|E_{Total}\|_\infty \\ &s.t. \quad \frac{\max(|\mathbf{B}_{matrix}X - B_{desired}|)}{\max(|B_{desired}|)} \leq \alpha \\ &\qquad |\mathbf{B}_{cryostat}X| \leq B_c \\ &\qquad |X| \leq I_{max} \\ &\qquad \mathbf{T}X = 0 \end{aligned} \tag{2.6}$$

α represents the maximum linearity error within the desired ROL. The matrix $\mathbf{T}$ includes the torque of basis elements in X and Y coils when a unit current is applied at a 1-Tesla uniform magnetic field (B_0).

2.3.4 Performance validation

For the first design, the E-fields induced by the array and conventional coils are compared while the B-field profiles are kept almost identical within a spherical ROL with 225mm radius. Then, E-fields of the disk-shaped ROL at different positions are simulated and compared with the conventional one. In this case, because the maximum E-field can occur within the volume of model rather than on the surface, the maximum intensity projections (MIP) of E-fields are reported.

For the second design, four different cases are investigated to validate the performance of the gradient array in minimizing the E-field in comparison to conventional coils: 1) spherical ROL with 225mm radius for body imaging: we call it standard mode operation because the array coil functions similarly to the conventional one with almost the same performance. 2) spherical ROL with 120mm radius: this case is ideal for imaging dedicated body parts such as the head, heart, breast, and prostate where the imaging region is smaller than the linear region generated by conventional coils. For this case, the gradient linearity error is swept to illustrate its effect on the induced E-field. 3) disk-shaped (slice) ROL: we consider a circular disk in the z direction (transverse slice) as a desired ROL and generate gradients in all three axes with the same functionality as a conventional design, first with the disk at the iso-center and then with a shifted disk in the positive z direction. 4) oblique off-center disk-shaped ROL: this is to indicate that array configuration is not limited to the Cartesian directions. In this case, we report the maximum magnitude of the induced E-field ($|E|_{max}$) which occurs on the surface of body model and the related PNS parameters, ΔG_{min} and SR_{min}.

The induced E-field depends on the body position inside the gradient coil. Here, we evaluate our method for positioning the head at the iso-center. In all cases, the slew rate is kept constant at 250T/m/s. The shielding performance is also consistent across all cases. The linearity error and root mean square (RMS) of the currents are the flexible parameters that will be compared to the conventional design.

2.4 Results

2.4.1 First design: Z gradient only

The winding patterns, the position of body model (head at the iso-center), B-fields and E-fields for symmetric conventional and array coils are shown in Figure 2.4. Both coils generate 40mT/m gradient strength with the 3.2% linearity error for Conventional one and 4.2% for the array. The currents RMS and maximum induced E-field are similar as well.

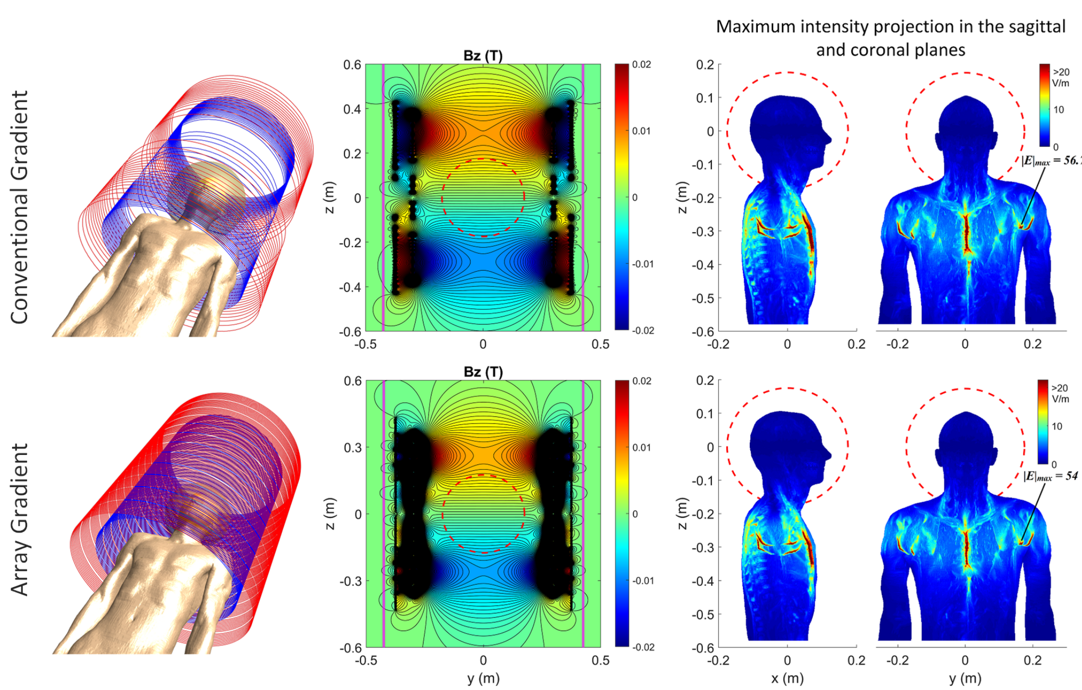

Figure 2.4: Comparison of conventional and array coils. Both coils have almost similar performance. The current RMS for the conventional and array coils are 330A and 350A, respectively.

Figure 2.5 compares the E-fields induced by the array coil when used as a conventional coil with a spherical ROL (upper row) and then as a disk-shaped ROL with optimized E-fields (buttom row). By optimizing the feeding currents, the array coil can produce the same gradient strength within a customizable disk-shaped ROL with a significantly lower E-field. The maximum E-field for a spherical ROL is 54V/m, while the maximum E-field for a disk-shaped ROL is 22.6V/m, representing a 58% reduction. This means that when linearity is required in a small ROL, the maximum gradient and slew rate can be increased without stimulating the nerves, which is promising for applications such as diffusion-weighted imaging. The gradient linearity error and current RMS are also lower for the disk ROL than for the spherical ROL.

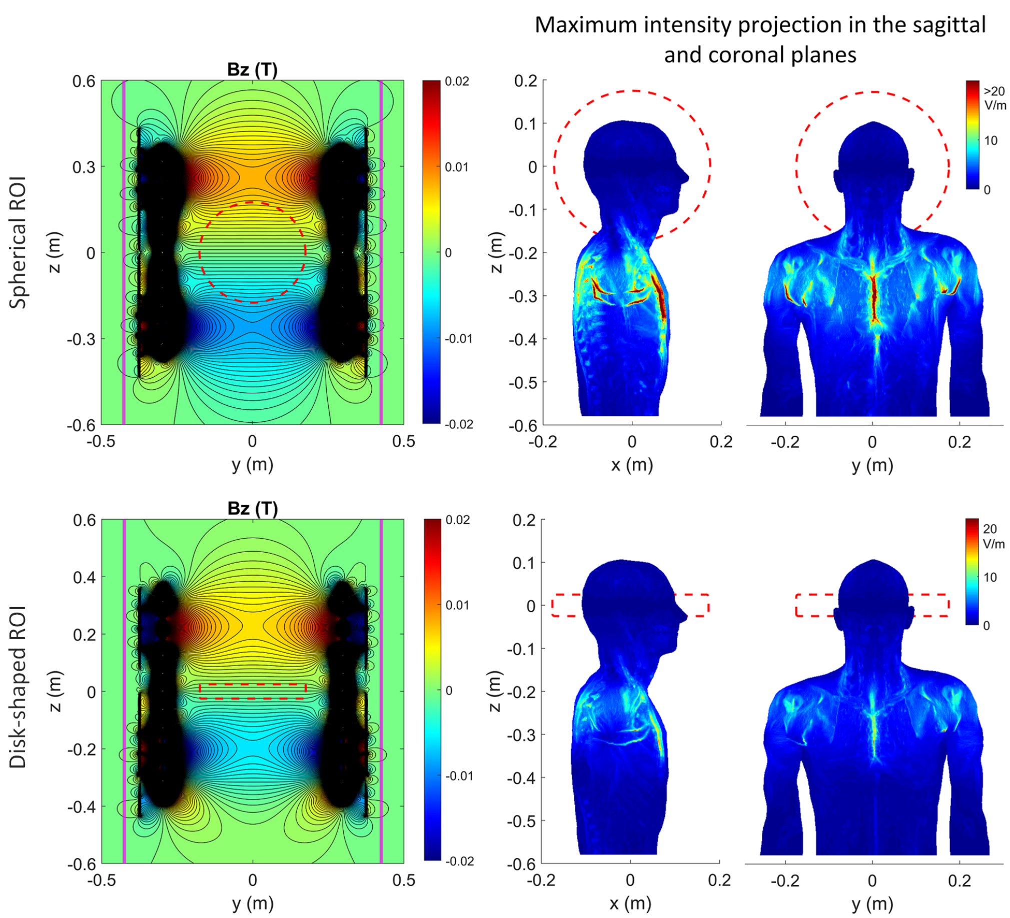

Figure 2.5: Comparison of spherical and disk-shaped ROLs. The linearity error for the spherical ROL is 4.2% and for the disk-shaped ROL is 2.1%. The currents RMS for the spherical and disk-shaped ROLs is 350A and 250A, respectively.

The disk position is also adjustable, and it can be moved superior/inferior to cover different areas. Figure 2.6 shows, for example, the results of disk at $z = +75mm$ and $-75mm$. Only the position of the linearity region has shifted; the gradient strength and slew rate remain unchanged. When moving the disk in a positive direction, the maximum induced E-field is 14.9V/m, which is reduced by a factor of 4 when compared to the conventional mode. For the disk shifted in the negative direction the maximum E-field is 21.7V/m. The maximum induced E-fields, gradient linearity error, and currents RMS for the different cases are reported in Table 2.1.

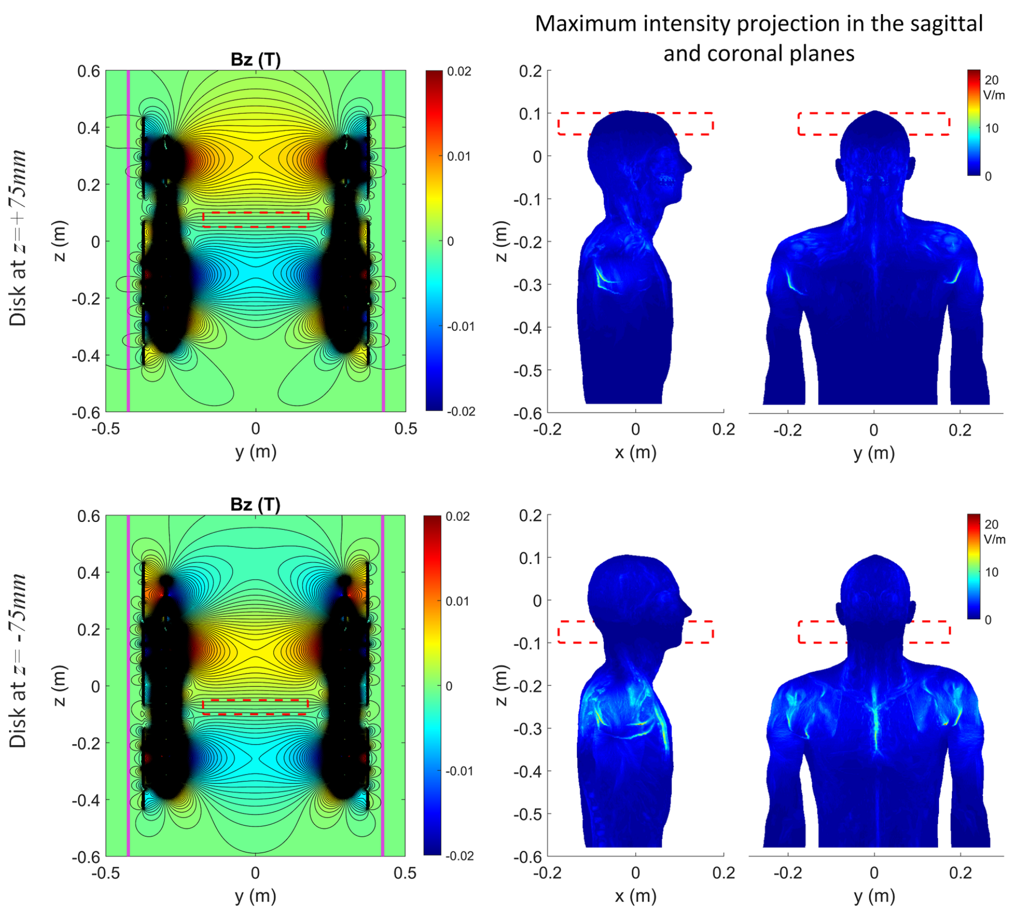

Figure 2.6: B-field and E-field of array coil when optimized for a disk-shaped ROL at $z = +75mm$ and $z = -75mm$.

In Figure 2.7, the average induced E-fields within body volume are compared for various ROL with and without E-field constraint in the optimization process. In a spherical ROL, for example, incorporating an E-field constraint reduces the

Table 2.1: Gradient coil performance values

	Maximum E-field (V/m)	Linearity error (%)	Currents RMS (A)
Conventional	56.7	3.2	330
Array (spherical ROL)	54	4.2	350
Array (Disk at iso-center)	22.6	2.1	250
Array (Disk at $z = +75mm$)	14.9	3.7	301
Array (Disk at $z = -75mm$)	21.7	6	345

average E-field by 22% but increases the linearity error by a factor of two. It is, however, still within an acceptable range (less than 10%). When the spherical ROL is compared to the disk-shaped ROL at the iso-center, the average E-field is reduced by 45%, and linearity improves as well. Adding an E-field constraint to the optimization for the Disk ROL at other positions also reduces the E-field but increases the linearity error and the currents RMS. The optimization problem used to obtain these results minimizes the difference between the generated and desired magnetic field (correspond to the linearity error). The E-field threshold is chosen so that the linearity error is within an acceptable range while also satisfying the currents constraint. Any modification to the constraints results in a new solution with different parameters.

2.4.2 Second design: X, Y, and Z gradients

Figure 2.8 demonstrates that the whole-body gradient array coil performs almost similarly to a conventional gradient coil. Because the winding patterns of the array and conventional coils are identical for the X and Y gradients, by applying the same current amplitude to all channels of the array, it will act as a conventional one. However, the optimization problem with E-fields as an objective function yields a different combination of the feeding currents. The winding patterns of the array and conventional coils are different for the Z gradient; however, by adjusting the optimization constraints, the array coil functions similar to the conventional one. Using different combinations of feeding currents, the array coil can achieve a lower $|E|_{max}$ than the conventional coil while the linearity error is fixed within the desired ROL for all three gradients. For example, the $|E|_{max}$ induced by the conventional Y gradient is 9.87V/m with a maximum linearity error of 4.18%, whereas an array coil induces 9.26V/m with

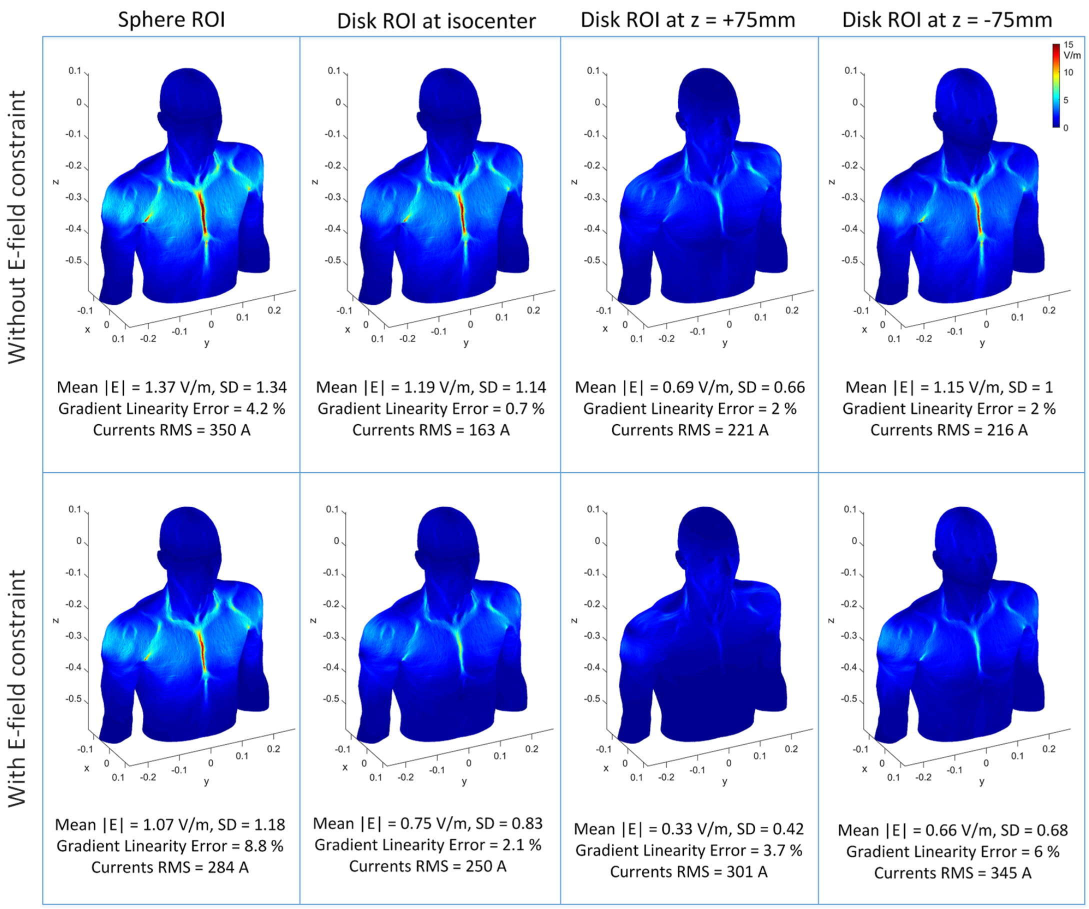

Figure 2.7: Comparison of average induced E-fields within body volume.

nearly the same linearity error. It is worth noting that, in this case, the gradient array consumes more power than the conventional in order to reduce the $|E|_{max}$ while producing the same gradient strength and slew rate.

Conventional coils are designed for a fixed ROL and have no flexibility in adjusting the size of the ROL. However, for some body parts imaging, like the head, such a large ROL (225mm radius) is not required. The linearity error is also fixed in conventional designs and cannot be altered after construction. Figure 2.9 depicts the ability of an array configuration to generate a target B-field within a small ROL with flexible linearity error while minimizing the $|E|_{max}$. The conventional coil has nearly perfect linearity within a 120mm radius spherical ROL, but the array coil can achieve the same linearity with less induced $|E|_{max}$. The Z gradient has the most significant reduction (28% with a 1% linearity error).

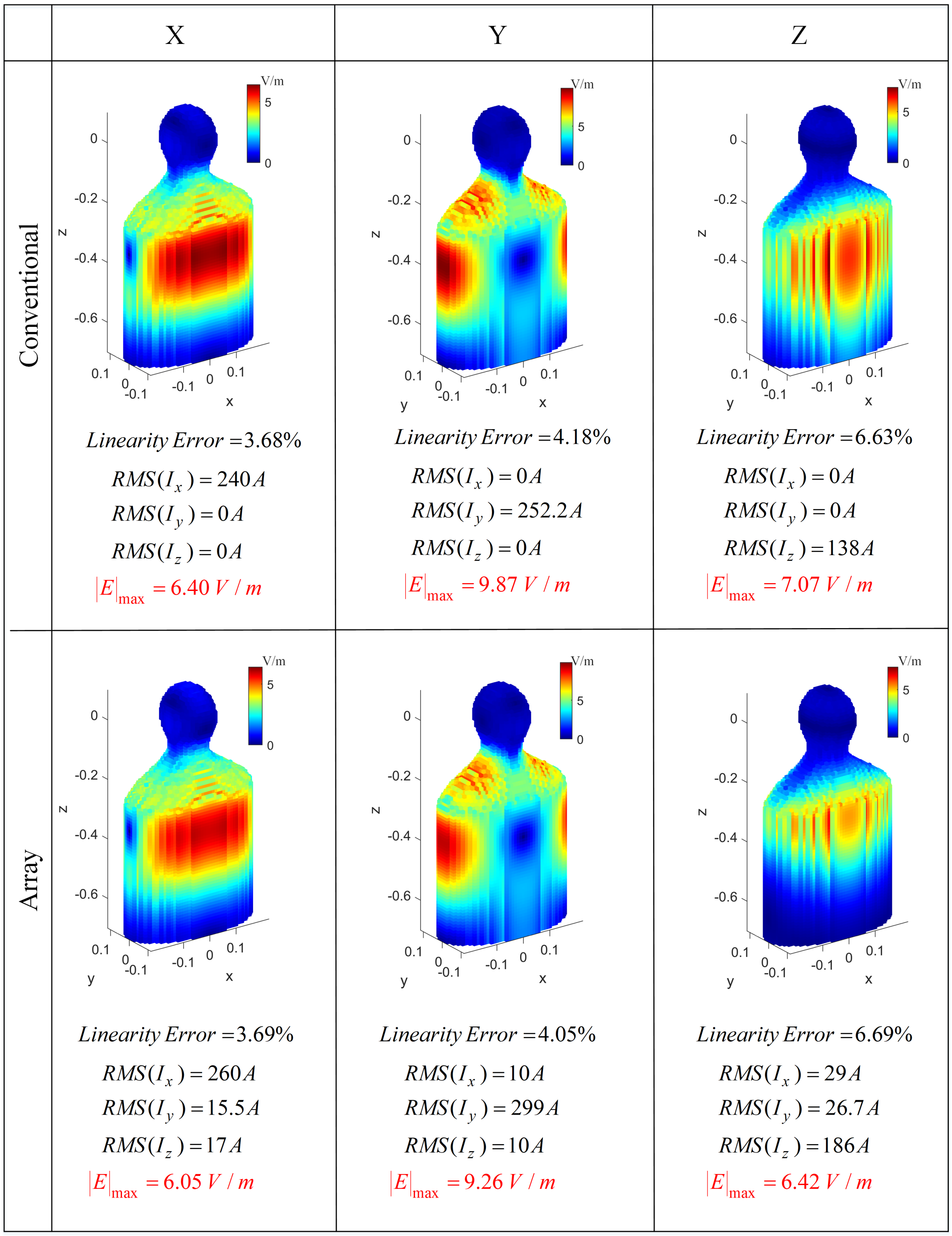

Figure 2.8: Comparison of gradient array and conventional coil. The maximum linearity error is the same for both designs; however, by using a slightly higher current RMS in the array coil, the maximum E-field is reduced for all three gradients.

In this case, ΔG_{min} is increased from 28mT/m (conventional) to 39mT/m (array), and similarly, SR_{min} is increased from 78T/m/s to 110T/m/s. Relaxing the linearity error can reduce $|E|_{max}$ even further. In Figure 2.9, each green square depicts a set of solutions for a specific linearity error (up to 5%). For example, adjusting the linearity error constraint to 5% in Z gradient the $|E|_{max}$ is reduce by 62% compared to the conventional coil, which corresponds to a 2.5-fold increase in PNS parameters. For X and Y coils, PNS parameters is increased by 38% and 25%, respectively. The performance of array design is higher for Z gradient because: first, the winding patterns of X and Y are identical with conventional coils, whereas this is not the case for Z coil. Second, the X and Y coils must be torque balanced (the equality constraint in the optimization problem), and it is impossible to reduce $|E|_{max}$ any further without compromising this balance.

Another feature of array configuration is that the target field can be generated within a disk-shaped (slice) ROL rather than a large spherical one. Figure 2.10 depicts the induced E-fields when the target field is generated in a circular disk in the z-direction, at $z = 0$ (upper row) and $z = 0.08m$ (bottom row). When the disk is placed at $z = 0$, and $z = 0.08m$, PNS parameters of Z gradient are increased 3-fold and 12-fold, respectively, compared to the conventional coil. The off-center slice (shifted in the positive z direction) is chosen at random to demonstrate the performance of the array configuration in increasing PNS thresholds. Lower induced E-fields are expected for this slice because the body area is less exposed to the electromagnetic fields.

Figure 2.11 illustrates the results of an oblique off-center slice. The slice is chosen in the X+Y direction with 40mm thickness at 0.1m distance from the center. Phase encoding and readout gradients can be chosen in a way to make three perpendicular axes, for example, X-Y+Z and X-Y-2Z. It can be seen from Figure 2.11 that with a fixed linearity error for both designs (conventional and array), the gradient array induces less E-field on the body model surface in comparison to the conventional gradient. The most significant increase in PNS thresholds is observed for the X+Y gradient (36%). The PNS parameters of conventional and array gradient coils are summarized in Table 2.2.

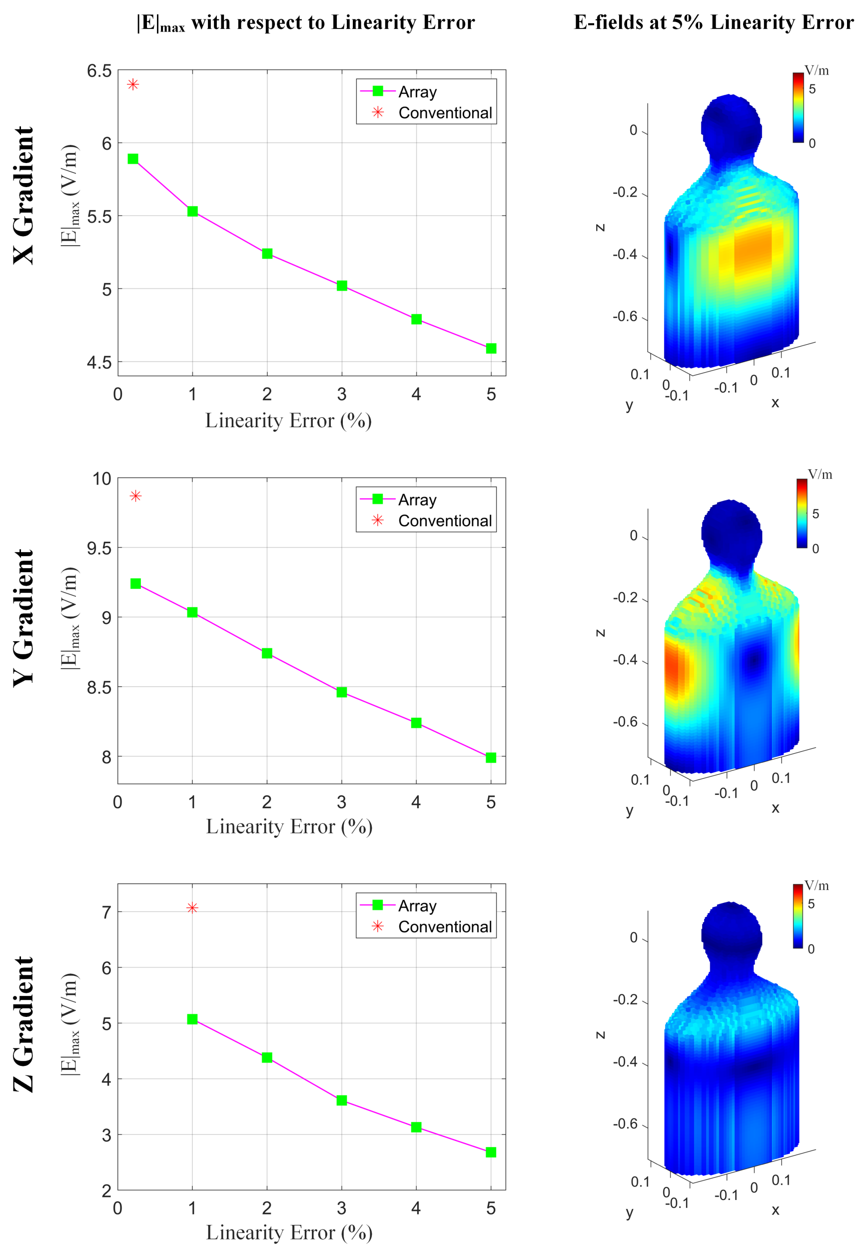

Figure 2.9: The left column depicts the $|E|_{max}$ with respect to the linearity error. Conventional designs have almost perfect linearity in a small ROL (120mm). The gradient array coil can generate the desired gradient with the same linearity while the induced E-field is minimized. By optimizing the feeding current with different linearity errors, it is possible to reduce the E-fields even further. The right column displays the E-field for X, Y, and Z gradients (array) at a 5% linearity error.

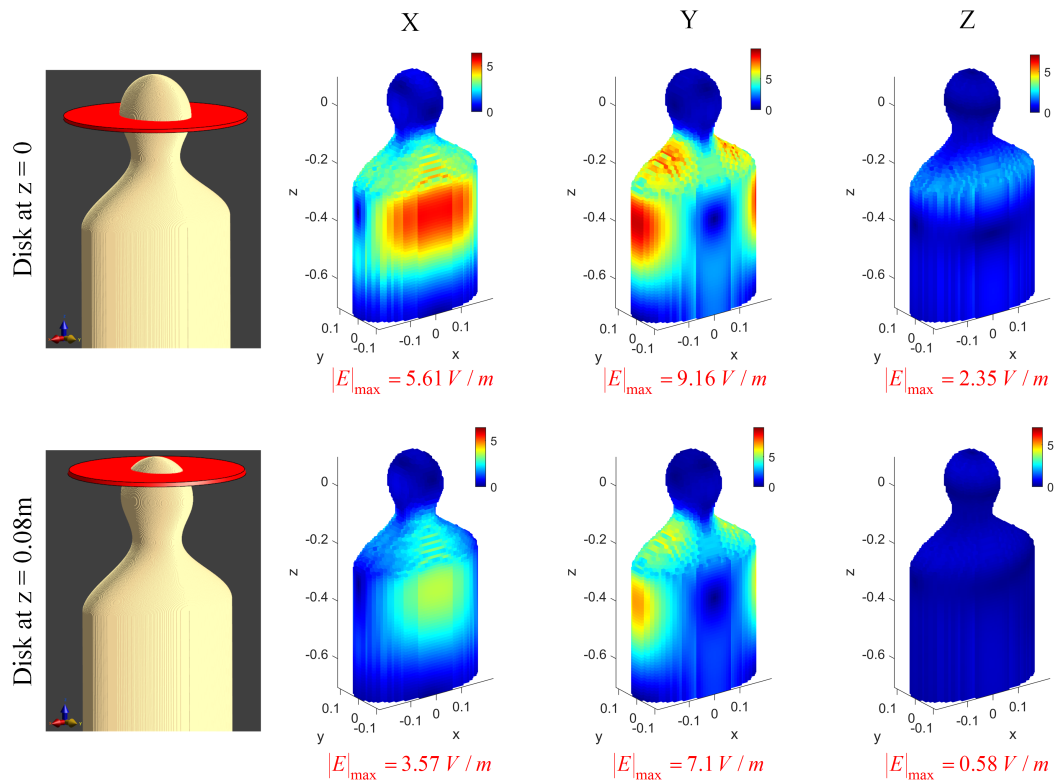

Figure 2.10: E-field plots for all gradients when the linearity is required within a disk in the z-direction (20mm thickness). First row: disk at the iso-center, second row: the disk is shifted in the positive z direction.

2.5 Discussion

In this work, we demonstrated that a whole-body gradient coil with an array configuration could minimize the induced E-field on the surface of a simplified body model while generating a target B-field with dedicated linearity error within a customizable ROL. Minimum E-field design implies that higher gradient strengths and slew rates can be achieved without exceeding PNS thresholds if the

Table 2.2: PNS parameters ΔG_{min} (mT/m units) and SR_{min} (T/m/s units)

	X		Y		Z	
	ΔG_{min}	SR_{min}	ΔG_{min}	SR_{min}	ΔG_{min}	SR_{min}
Conventional	31	86	20	55	28	78
Array (120mm ROL, 5% linearity error)	43	118	25	69	75	207
Array (Disk at $z = 0$)	35	98	22	60	84	234
Array (Disk at $z = 0.08m$)	55	154	28	77	341	948

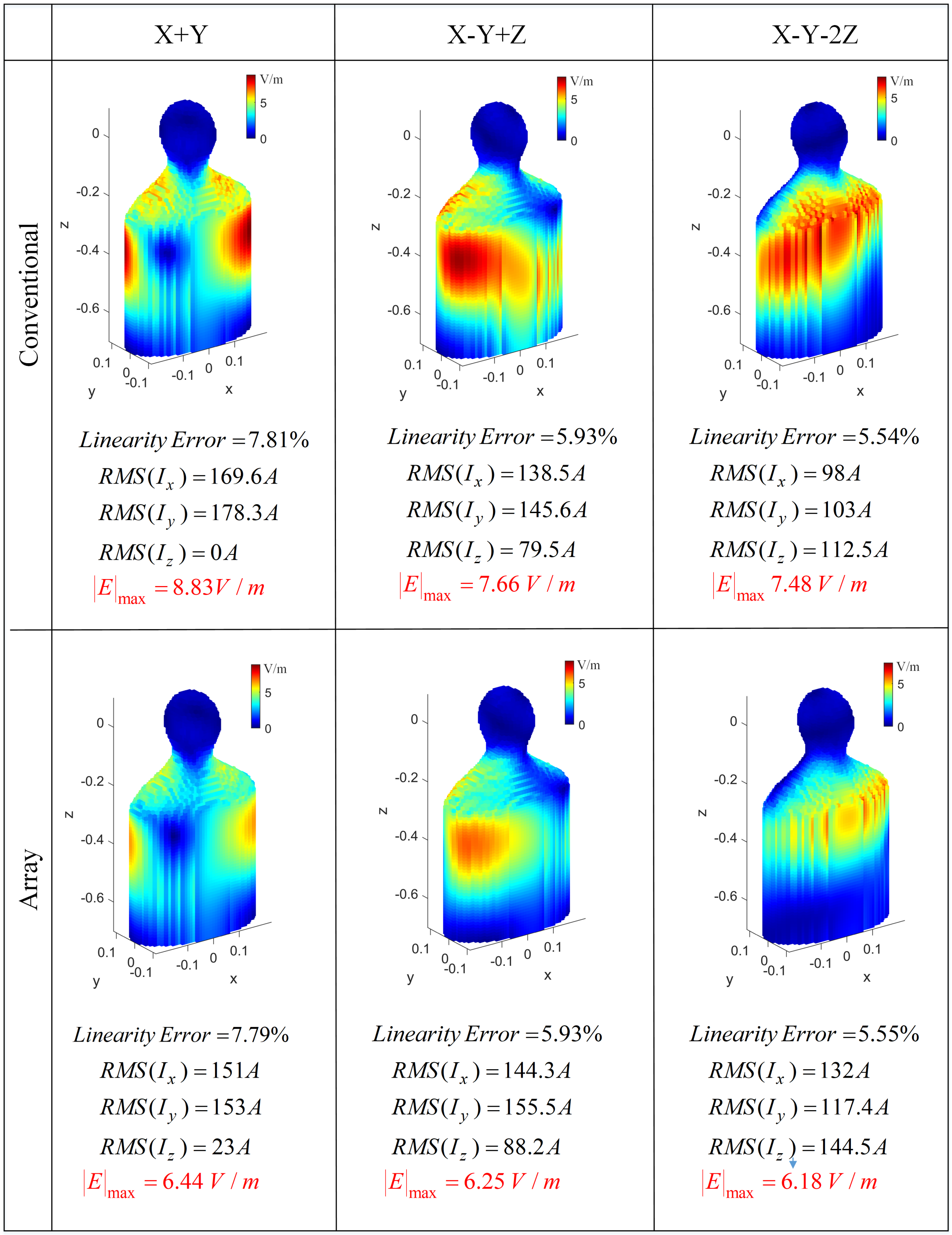

Figure 2.11: Off-center oblique slice: the slice is chosen in X+Y axis (at 0.1m distance from the center with 40mm thickness), the other two can be used as phase encoding or readout direction. For the slice selection gradient there is a 36% increase in PNS thresholds. For the X-Y+Z and X-Y-2Z axes, PNS thresholds are increased by 22% and 21%, respectively.

required hardware is available. Our findings demonstrated that the gradient array coil not only functions as a conventional coil but also outperforms conventional designs in various situations. Engineering metrics such as ROL size and linearity error may vary from scan to scan. The gradient array can apply the required currents that are optimized for a specific application.

We did not attempt to optimize the gradient array coil design in this preliminary work. For example, coil dimensions, X and Y coil winding patterns, shielding performance, and power consumption are chosen in a manner similar to a conventional gradient coil designed by Sim4Life software. We expect to reduce the $|E|_{max}$ even further with advanced gradient design techniques. Because the body model used in this study had uniform electrical properties, the maximum E-field always occurred on the surface of the body model. A similar performance in reducing E-fields of heterogeneous body models is expected.

The position of the body inside the scanner is another factor in determining the PNS thresholds. We calculated E-fields when the head was at the iso-center, but the E-fields can be calculated for any position, and an optimization problem can be solved for that position. In that case, only the feeding current combinations will change, with no modifications to the hardware.

Considering the E-fields at the exact location of nerves improves optimization performance; however, it requires extensive knowledge of the body nerves atlas. The reason for this is that having a high $|E|_{max}$ in a location where there is no nerve will not result in PNS, and considering all sample points on the body significantly limits the optimization problem. The optimization problem can be modified to maximize the gradient strength (with a constant slew rate) instead of minimizing E-fields. E-field (PNS) thresholds can be used as a nonlinear inequality constraint in this case. Alternatively, the gradient array coil can be optimized to achieve the highest possible gradient strength and slew rate without causing PNS.

Chapter 3

Nonlinear Droop Compensation for Gradient Current Waveforms

Preface

The contents of this chapter including figures and texts were firstly presented at the 29th Annual Meeting of International Society for Magnetic Resonance in Medicine [51] and were then published in Magnetic Resonance in Medicine journal with the title of ”Nonlinear droop compensation for current waveforms in MRI gradient systems” [52]. The gradient power amplifiers that are used in this chapter were provided by ASELSAN (Ankara, Turkey). Special thanks to Volkan Acikel and Soheil Taraghinia for their assistance with the amplifiers functionality.

3.1 Introduction

MRI scanners use three gradient coils to provide spatial encoding within an imaging volume. Gradient power amplifiers (GPAs) with high voltage and high current specifications drive the gradient coils. The current flowing through each coil has to follow a command waveform as accurately as possible to ensure good image quality. However, providing accurate gradient coil currents might be challenging due to hardware imperfections. Conventional gradient systems use closed-loop feedback controllers [23, 24] to precisely track the command input current. Thus, they require high-precision high-cost current sensors because small errors in the current result in artifacts in the images [23]. Recently introduced gradient array systems [14–17], multi-coil technique [18–20], and matrix gradient coils [21, 22], which are capable of generating dynamically controllable magnetic field profiles, utilize multiple gradient coils, and hence need many current sensors for the feedback loop, which significantly increase the system cost ($>$ \$600 per sensor). Therefore, feed-forward controllers might be preferable to avoid using measurement data and expensive current sensors.

In an ideal system, the gradient amplifiers are powered by a constant voltage at all times. However, in a practical system, the power supply loses its voltage gradually when it starts to deliver a high current. The gradual decrease of the supply voltage is called droop [53–55] and causes a gradual decrease in the current at the flat top of a gradient pulse if there is no feedback. To use feed-forward controllers effectively, at least an approximate system model should be available. Ertan et al. [15] considered a linear time-invariant (LTI) first-order model of the gradient system in the feed-forward, including only the gradient coil model. The GPAs were assumed to generate an ideal voltage source ignoring the potential droop in the supply. However, as discussed in this work, the droop is a nonlinear process that cannot be corrected with an LTI controller. Therefore, it is crucial to include the GPAs and power supply stages in the gradient system model to have an accurate nonlinear model to compensate for the droop.

Gradient chain characterization techniques such as gradient impulse response function (GIRF) [56–61] or gradient modulation transfer function (GMTF) [62,63] are also based on the assumption that the gradient system behaves as an LTI system. The information acquired from these techniques is used for trajectory correction in the image reconstruction procedure. Ideally, the gradient waveforms are controlled precisely such that trajectory correction is unnecessary.

Here, a nonlinear second-order model is introduced for gradient chain, including GPA and power supply. The focus of this work is the investigation of nonlinearities associated with the GPA and compensation for GPA's imperfections rather than the gradient coil's. The State Space Averaging (SSA) method has been used in the literature [25–29] to model the DC-DC power convertors in a steady-state, linearized around an operating point. We use the modified SSA method to characterize the switching GPAs, both steady-state and transient behavior, by considering nonlinear equations. The accuracy of the SSA method primarily depends on the switching frequency of pulse width modulation (PWM) signals. In our case, this method is applicable because of high-switching PWMs (1MHz). The digital inversion of the acquired model is then used in the feed-forward open-loop configuration to provide the required voltage to control the output gradient currents. Using the nonlinear controller compensates for the current droop in the plateau region of the trapezoidal gradient waveforms and provides slight corrections in the transients. As proof of concept, this study considers a Z gradient coil with two separate windings driven by two independent GPAs and power supplies. A nonlinear multi-input-multi-output feed-forward controller is applied. The output currents are measured for both linear and nonlinear controllers by applying a trapezoidal waveform at the input. Finally, the MRI experiments are conducted to show the effectiveness of the proposed method.

3.2 Methods

3.2.1 Gradient Power Amplifier and PWM generation

Switch-mode full-bridge GPAs [64, 65] are standard amplifier types to drive MRI gradient coils with high current levels in several hundred amperes. These amplifiers operate by rapidly switching back and forth between the supply rails, being fed by PWM signals. In PWM, the frequency of pulses remains fixed, but the duration of each pulse is modulated according to the corresponding duty cycle. The duty cycle is calculated by dividing the required voltage by the power supply voltage (either feed-forward or feedback controller).

$$d = \frac{v_{\mathrm{required}}}{V_{\mathrm{S}}} \tag{3.1}$$

Note that d has to be in the range of -1 to 1. The full-bridge amplifier configuration and center-aligned approach for PWM generation are shown in Figures 3.1A and 3.1B, respectively.

Considering a feed-forward configuration and for a given desired current waveform, $i(t)$, the required voltage, v_{required}, can be calculated by,

$$v_{\mathrm{required}}(t) = L\frac{di(t)}{dt} + Ri(t) \tag{3.2}$$

where, L and R represent the inductance and resistance of the gradient coil, respectively. This linear equation can be extended for the gradient array or multi-coil systems, in which case, the mutual inductance between the coils should be considered.

Equation 3.1 holds true if drain voltages of GPA MOSFETs are constant and equal to the supply voltage, which yields a first-order linear model for the gradient systems. In practice, however, the supply voltage is not constant.

3.2.2 Modified State-Space Averaging

The State-Space Averaging (SSA) approach is developed to characterize switching power converters [26]. The DC-DC power conversion is accomplished by repetitively switching between linear circuits with lossless storage components, inductances and capacitances. Assuming a single period of PWM, there are only two different states of the circuit: "on" and "off" (Figure 3.2). During the intervals T_{on} ($nT < t < t_{\mathrm{s}}$) and T_{off} ($t_{\mathrm{s}} < t < (n+1)T$), where t_{s} is the switching time, the following linear time-invariant differential equations describe the system:

$$\frac{d\,\mathbf{x}(t)}{dt} = \begin{cases} \mathbf{A}_{\mathrm{on}}\mathbf{x}(t) + \mathbf{b}_{\mathrm{on}} & nT < t < t_{\mathrm{s}} \\ \mathbf{A}_{\mathrm{off}}\mathbf{x}(t) + \mathbf{b}_{\mathrm{off}} & t_{\mathrm{s}} < t < (n+1)T \end{cases} \tag{3.3}$$

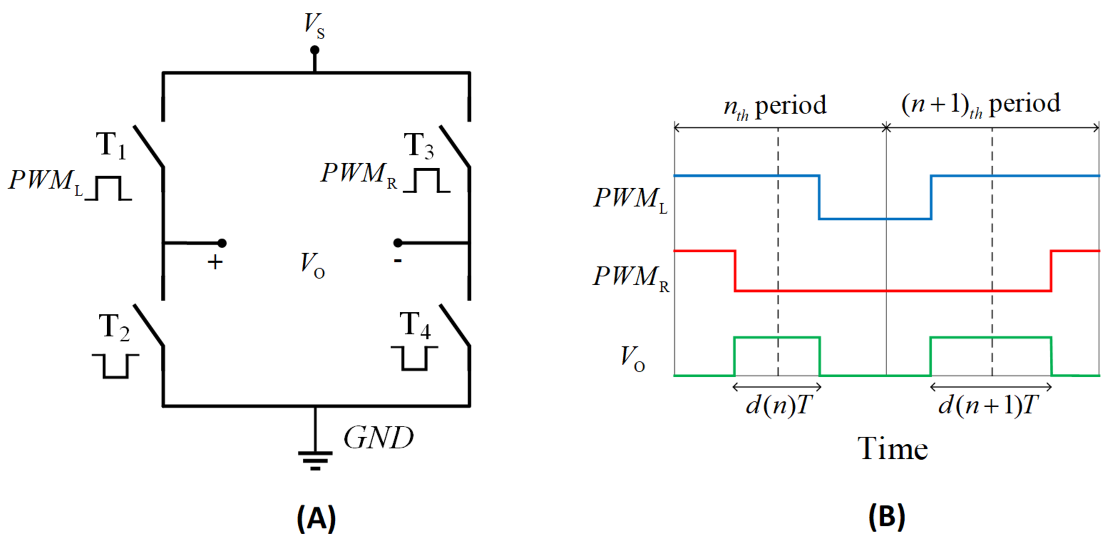

Figure 3.1: (**A**) Full-bridge power amplifier configuration (**B**) The center-aligned approach for two periods of PWM. The waveforms for the high-side transistors (T_1 and T_3) are shown in the figure. The low-side transistors (T_2 and T_4) are switched with the complementary logic.

This equation is the state-space representation of differential equations, where $\mathbf{x}$ is the state vector, composed of the inductor's current and capacitor's voltage. The state matrix $\mathbf{A}_{\text{on}}$ and the input vector $\mathbf{b}_{\text{on}}$ describe the circuit topology when it is in the "on" state. Likewise, $\mathbf{A}_{\text{off}}$ and $\mathbf{b}_{\text{off}}$ represent the "off" state. The corresponding solutions of the above equations are:

$$\mathbf{x}(t) = \begin{cases} e^{\mathbf{A}_{\text{on}}(t-nT)}\mathbf{x}(nT) + \mathbf{A}_{\text{on}}^{-1}\left(e^{\mathbf{A}_{\text{on}}(t-nT)} - \mathbf{I}\right)\mathbf{b}_{\text{on}}, & nT < t < t_s \\ e^{\mathbf{A}_{\text{off}}(t-t_s)}\mathbf{x}(t_s) + \mathbf{A}_{\text{off}}^{-1}\left(e^{\mathbf{A}_{\text{off}}(t-t_s)} - \mathbf{I}\right)\mathbf{b}_{\text{off}}, & t_s < t < (n+1)T \end{cases} \tag{3.4}$$

Knowing that, $t_s - nT = T_{\text{on}} = d(n)T$ and $(n+1)T - t_s = T_{\text{off}} = (1-d(n))\,T$, at $t = (n+1)T$:

$$\begin{aligned} \mathbf{x}\left((n+1)T\right) = e^{\mathbf{A}_{\text{off}}(1-d(n))T}\left[e^{\mathbf{A}_{\text{on}}d(n)T}\mathbf{x}(nT) + \mathbf{A}_{\text{on}}^{-1}\left(e^{\mathbf{A}_{\text{on}}d(n)T} - \mathbf{I}\right)\mathbf{b}_{\text{on}}\right] \\ +\mathbf{A}_{\text{off}}^{-1}\left(e^{\mathbf{A}_{\text{off}}(1-d(n))T} - \mathbf{I}\right)\mathbf{b}_{\text{off}} \end{aligned} \tag{3.5}$$

Now we use the first-order approximation of the fundamental matrix $e^{\mathbf{A}t} \approx \mathbf{I} + \mathbf{A}t$ and keep only the first-order terms. By defining $\mathbf{x}(n) = \mathbf{x}(nT)$, the following difference equation describes the general behavior of the circuit:

$$\mathbf{x}(n+1) = \underbrace{\left[\mathbf{I} + d(n)T\mathbf{A}_{\text{on}} + (1-d(n))\,T\mathbf{A}_{\text{off}}\right]}_{\mathbf{A}_{\text{avg}}}\mathbf{x}(n) + \underbrace{\left[d(n)T\mathbf{b}_{\text{on}} + (1-d(n))\,T\mathbf{b}_{\text{off}}\right]}_{\mathbf{b}_{\text{avg}}} \tag{3.6}$$

where T is the sampling period, $\mathbf{I}$ is the identity matrix, and $d(n)$ is the duty cycle of n_{th} period, which is the main input of the system in DC-DC power converters. $\mathbf{x}(n)$ and $\mathbf{x}(n+1)$ are the state vectors at the beginning and the end of the n_{th} period, respectively. The edge-aligned configuration is considered here for simplicity. However, it can be shown that the result is not a function of the phase, and thus the center-aligned PWM can be approximated with the same equation. Equation 3.6 describes the averaged behavior of the circuit, effectively smoothing out the switching ripple, and we call it the averaged model. In a linear system, the state matrix is a constant, and the input appears only in the additive term, $\mathbf{b}$. However, the state matrix in Equation 3.6 ($\mathbf{A}_{\text{avg}}$) incorporates the duty cycle, which is the input, making the system nonlinear, i.e. doubling the input does not simply double the output.

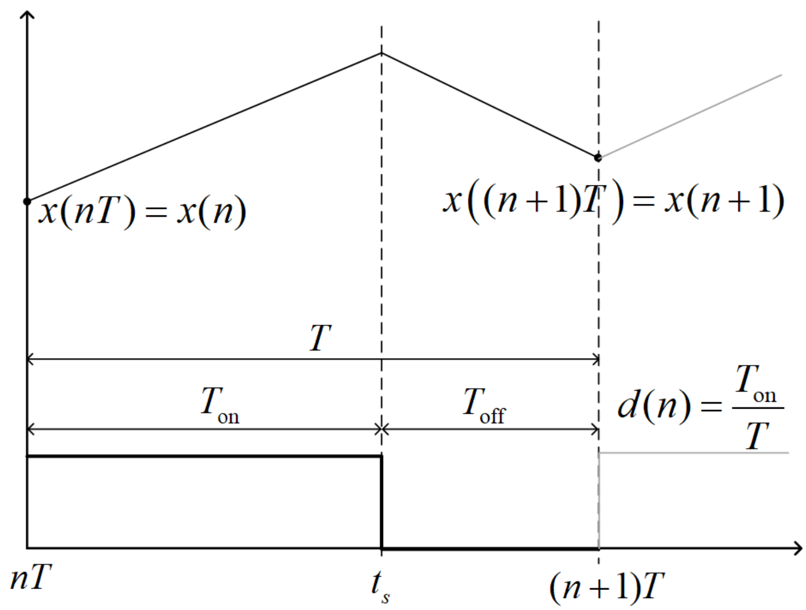

Figure 3.2: A single circuit variable (the inductor current, for example) time dependence over a period of PWM (T) with the PWM's on and off duration. The duty cycle, $d(n)$, is defined as the ratio of T_{on} to (T).

3.2.3 Single-channel gradient system

The gradient system considered here includes the gradient coil, gradient power amplifier, power supply stage, and PWM generation block. The gradient system's input is the duty cycle, and the output is the gradient coil current i_{GC}. Since the switching frequency of our GPA is high enough, the modified SSA technique introduced in the previous section is used to characterize the general behavior of the gradient system. Considering a single period of PWMs, the on and off states of the circuit, which are shown with green and red paths in Figure 3.3A, respectively, can be described with the following equations:

$$\frac{d}{dt}\begin{bmatrix} i_{\mathrm{GC}}(t) \\ v_{\mathrm{C}}(t) \end{bmatrix} = \begin{cases} \begin{bmatrix} -\frac{R_{\mathrm{GC}}}{L_{\mathrm{GC}}} & \frac{1}{L_{\mathrm{GC}}} \\ -\frac{1}{C} & -\frac{1}{R_{\mathrm{S}}C} \end{bmatrix} \begin{bmatrix} i_{\mathrm{GC}}(t) \\ v_{\mathrm{C}}(t) \end{bmatrix} + \begin{bmatrix} 0 \\ \frac{V_{\mathrm{S}}}{R_{\mathrm{S}}C} \end{bmatrix} & \text{for interval } T_{\mathrm{on}} \\ \begin{bmatrix} -\frac{R_{\mathrm{GC}}}{L_{\mathrm{GC}}} & 0 \\ 0 & -\frac{1}{R_{\mathrm{S}}C} \end{bmatrix} \begin{bmatrix} i_{\mathrm{GC}}(t) \\ v_{\mathrm{C}}(t) \end{bmatrix} + \begin{bmatrix} 0 \\ \frac{V_{\mathrm{S}}}{R_{\mathrm{S}}C} \end{bmatrix} & \text{for interval } T_{\mathrm{off}} \end{cases} \tag{3.7}$$

The state variables are the gradient coil current and the decoupling capacitor voltage. The averaged nonlinear model can be formulated as follow:

$$\begin{bmatrix} i_{\mathrm{GC}}(n+1) \\ v_{\mathrm{C}}(n+1) \end{bmatrix} = \begin{bmatrix} 1-\frac{TR_{\mathrm{GC}}}{L_{\mathrm{GC}}} & \frac{T}{L_{\mathrm{GC}}}d(n) \\ -\frac{T}{C}d(n) & 1-\frac{T}{R_{\mathrm{S}}C} \end{bmatrix} \begin{bmatrix} i_{\mathrm{GC}}(n) \\ v_{\mathrm{C}}(n) \end{bmatrix} + \begin{bmatrix} 0 \\ \frac{TV_{\mathrm{S}}}{R_{\mathrm{S}}C} \end{bmatrix} \tag{3.8}$$

This equation shows the inter-dependency of gradient current and capacitor voltage. If d is zero, at the steady-state, the gradient coil current, i_{GC}, is zero. The capacitor voltage, v_{C}, becomes equal to the supply voltage, V_{S}. When d becomes high, v_{C} starts to decrease. As a result, the gradient current cannot follow the value of d and gradually decreases. This event is called droop in the power electronics. The amount of droop depends on the circuit parameters and the magnitude of the current flowing the coil. As the gradient coil current increases, the droop increases nonlinearly. It is worthy of mentioning that if we consider only the gradient coil model (ignoring the capacitor and power supply nonideality), the resulting equation will be the first-order linear one used in previous works [15,66].

3.2.4 Multi-coil gradient system

The modified SSA technique can be used to characterize gradient systems with coupled coils as well. As a proof of concept, we write equations for a two-channel gradient only; however, it can be easily generalized for a high number of channels.

Assuming $d_1 > d_2$ (d_1: channel1 duty cycle, d_1: channel2 duty cycle), there are only three different circuit states. During the intervals $T_{\text{on}-\text{on}}, T_{\text{on}-\text{off}}, T_{\text{off}-\text{off}}$ (Figure 3.3B), the system can be described by a set of linear, time-invariant differential equations:

$$\frac{d\,\mathbf{x}(t)}{dt} = \begin{cases} \mathbf{A}_{\text{on}-\text{on}}\mathbf{x}(t) + \mathbf{b}_{\text{on}-\text{on}}\,, & \text{for interval } T_{\text{on}-\text{on}} \\ \mathbf{A}_{\text{on}-\text{off}}\mathbf{x}(t) + \mathbf{b}_{\text{on}-\text{off}}\,, & \text{for interval } T_{\text{on}-\text{off}} \\ \mathbf{A}_{\text{off}-\text{off}}\mathbf{x}(t) + \mathbf{b}_{\text{off}-\text{off}}\,, & \text{for interval } T_{\text{off}-\text{off}} \end{cases} \tag{3.9}$$

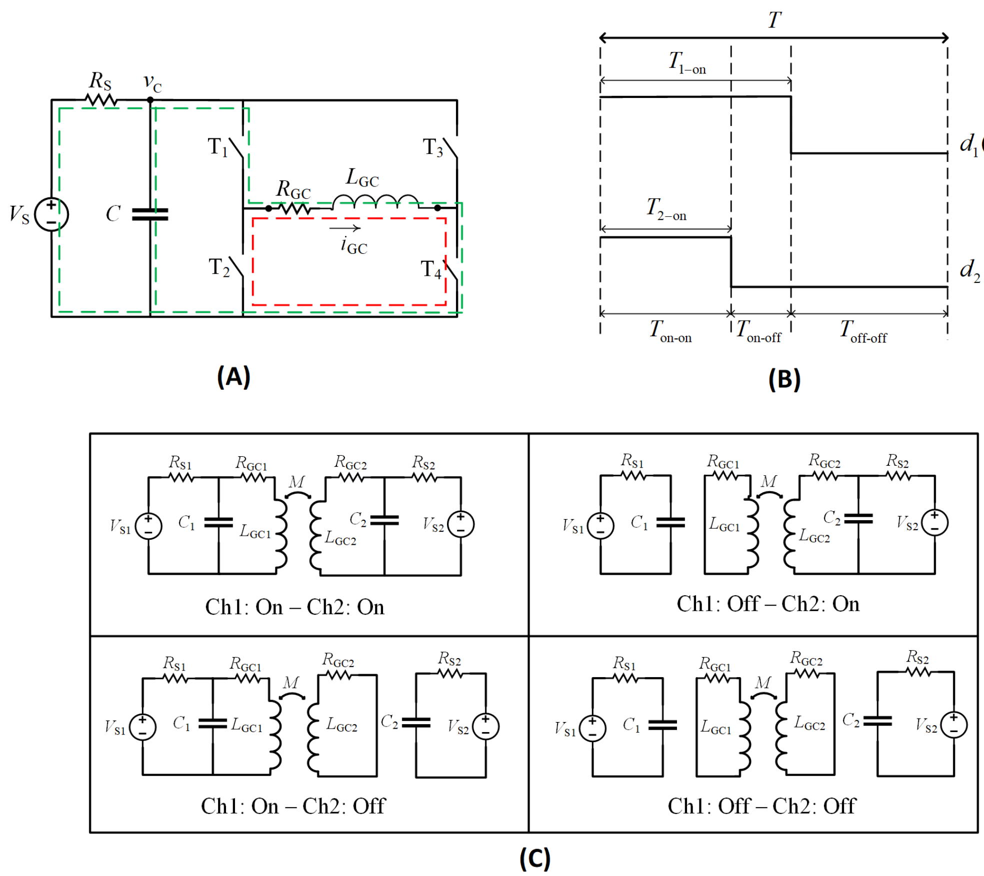

Figure 3.3: (**A**) single-channel gradient system circuit including amplifier, power supply with parallel decoupling capacitor, and the gradient coil. The green path shows the circuit during T_{on}, and the red one is for T_{off}. (**B**) PWMs for channel1 and channel2 assuming $d_1 > d_2$ and (**C**) Different states of two-channel system circuit which covers any combination of d_1, d_2.

Similar to the single-channel, under the rapid switching assumption, the circuit's general behavior can be described by a single difference equation:

$$\mathbf{x}(n+1) = \mathbf{A}\left(d_1(n), d_2(n)\right)\mathbf{x}(n) + \mathbf{b}\left(d_1(n), d_2(n)\right) \tag{3.10}$$

where, $\mathbf{x}$ is the state vector consists of gradient coils' current and capacitors' voltage. Matrices $\mathbf{A}$ and $\mathbf{b}$ are (K is the mutual inductance between the coils and $K = L_{\mathrm{GC1}}L_{\mathrm{GC2}} - M^2$):

$$\begin{gathered}
\mathbf{A}(n) = \begin{bmatrix} 1 - \frac{TR_{\mathrm{GC1}}L_{\mathrm{GC2}}}{K} & \frac{TL_{\mathrm{GC2}}}{K}d_1(n) & \frac{TMR_{\mathrm{GC2}}}{K} & -\frac{TM}{K}d_2(n) \\ -\frac{T}{C_1}d_1(n) & 1 - \frac{T}{R_{\mathrm{S1}}C_1} & 0 & 0 \\ \frac{TMR_{\mathrm{GC1}}}{K} & -\frac{TM}{K}d_1(n) & 1 - \frac{TR_{\mathrm{GC2}}L_1}{K} & \frac{TL_{\mathrm{GC1}}}{K}d_2(n) \\ 0 & 0 & -\frac{T}{C_2}d_2(n) & 1 - \frac{T}{R_{\mathrm{S2}}C_2} \end{bmatrix} \\
\mathbf{b} = \begin{bmatrix} 0 & 0 \\ \frac{TV_{\mathrm{S1}}}{R_{\mathrm{S1}}C_1} & 0 \\ 0 & 0 \\ 0 & \frac{TV_{\mathrm{S2}}}{R_{\mathrm{S2}}C_2} \end{bmatrix}
\end{gathered} \tag{3.11}$$

3.2.5 Control Architecture

The performance of the gradient system greatly depends on the selected control method. The feedback control (PID) method has been widely used to regulate the gradient current waveforms; however, this method limits the gradient system bandwidth and necessitates high-precision current sensors, raising the system's cost. On the contrary, feed-forward controllers do not need current measurements and have higher bandwidth but require an accurate system model. Although a linear model consisting of only gradient coil parameters (inductance and resistance) may provide a good approximation of the system, it does not cover the nonlinear behavior of GPAs and power supply stages. Therefore, improved characterization of the gradient system, which includes those nonlinearities, is essential.

To find the feed-forward controller, we use the inverse of the proposed averaged nonlinear model. The duty cycle is extracted from the desired gradient current waveform and calculated capacitor voltage in the discrete-time domain. As an example, for a single-channel gradient system, the following two recursive equations represent the inverse system (feed-forward controller):

$$d(n) = \frac{\frac{L_{\mathrm{GC}}}{T}\left(i_{\mathrm{dGC}}(n+1) - i_{\mathrm{dGC}}(n)\right) + R_{\mathrm{GC}} i_{\mathrm{dGC}}(n)}{v_{\mathrm{C}}(n)} \tag{3.12}$$

$$v_{\mathrm{C}}(n+1) = \left(1 - \frac{T}{R_{\mathrm{S}}C}\right) v_{\mathrm{C}}(n) - \frac{T}{C} d(n) i_{\mathrm{dGC}}(n) + \frac{T V_{\mathrm{S}}}{R_{\mathrm{S}}C} \tag{3.13}$$

where, $d(n)$ is the n_{th} PWM's duty cycle, $i_{\mathrm{dGC}}(n)$ and $v_{\mathrm{C}}(n)$ are the desired gradient current waveform and the calculated capacitor voltage, respectively. Since the desired current is known at all time points and the initial capacitor voltage is the supply voltage, $d(n)$ can be computed using Equation 3.12. The following values of $v_{\mathrm{C}}(n)$ will be calculated using Equation 3.13. The output of the feed-forward controller is the duty cycle, which will be used to generate the PWM signals. These equations can be easily extended to a high number of channels. Figure 3.4A depicts the block diagram of the feed-forward controller (inverse system) and the gradient system itself.

The Xilinx Virtex-VC707 evaluation board is used for the digital implementation of the feed-forward controller (Equations 3.12 and 3.13) and PWM signals generation. Center-aligned PWM with 500kHz switching frequency (1MHz effective frequency at the output, which leads to 1µs dwell time) is used to drive the GPAs' switches. The computation of feed-forward controller and PWM generation is fast enough to be completed within a dwell time, making the process real-time. The computational speed depends on the FPGA resources and the clock frequency used for calculations. In our case, the LUT (LookUp Table) utilization is 4503 out of 303600 (1.48%) for a single channel. The pipelined architecture is used to maximize the clock frequency. The resource utilization scales as the number of channels increases, but not linearly due to mutual couplings between channels. For a high number of channels, the FPGA resources may not be sufficient to compute all channels in parallel within a dwell time, resulting in a computational delay. However, it will not compromise real-time operation because a known fixed delay in an open-loop configuration can be easily handled by injecting the input signal in advance.

The resolution of PWMs has a significant impact on the nonlinear feed-forward controller's efficiency. High-resolution PWMs are required to be sensitive enough to detect small changes in the applied duty cycle. For this purpose, 400 MHz clock frequency is used as the main counter resulting in 10-bit resolution. Additional 5-bit is added by using delay elements of FPGA to achieve a 15-bit time resolution (78ps), which significantly reduces the digitization error in the gradient waveforms [67].

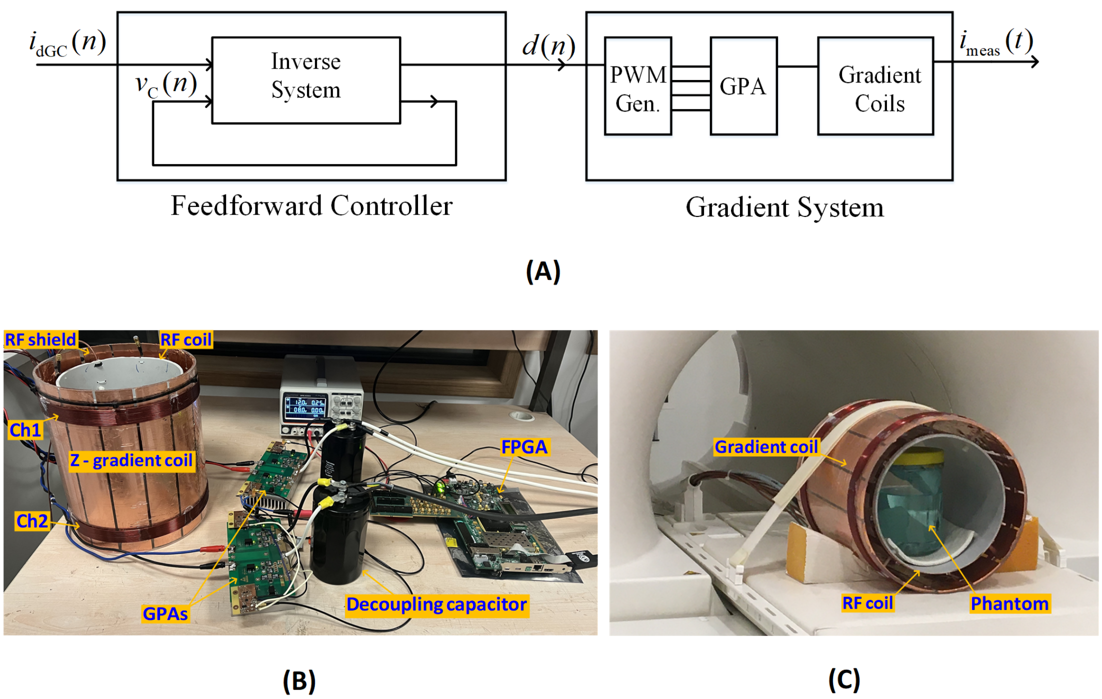

Figure 3.4: (**A**) The overall gradient chain block diagram, including the feed-forward controller and different components of the gradient system. (**B**) Benchtop installation, which is located in the equipment room. (**C**) The imaging setup including gradient coil, RF coil, TR switch, and phantom.

3.2.6 SSA model and Feed-forward control simulations

To demonstrate how accurately the SSA model follows the topological model, the responses of both models to two different inputs (constant and varying duty cycles) are compared in the simulation. The topological model is the exact circuit implementation, including the switching function (the circuit shown in Figure

3.3A). Gradient coil current simulations are also carried out using the linear and nonlinear controllers with a trapezoidal waveform as the input to illustrate the capability of the nonlinear controller in droop compensation.

Because the image quality directly depends on the integral of the gradient (current) waveform, the time integral of the desired test waveform is compared to the time integrals of waveforms generated using the linear and nonlinear controllers. MATLAB (R2020b, The MathWorks, Natick, MA) is used to conduct all simulations.

3.2.7 Hardware setup

Custom-built fast switching power amplifiers consist of new generation enhancement mode gallium nitride (eGaN) power transistors, which can operate in high-voltage, high-temperature, and high-frequency reliability, are used to provide the required voltage level to the gradient coil using the appropriate duty cycle. The fabricated GPAs are designed to be capable of 400V/100A operation ratings; however, smaller ratings were tested to be on the safe side. It is worth mentioning that our GPA costs less than $200, which is comparable to the existing low-cost gradient amplifiers [68, 69] but operates at higher power levels. The switching frequency in a conventional GPA is about 100kHz; however, by using eGaN transistors [70], it is possible to increase the switching frequency to 500kHz, which results in a reduction of current ripples without LC low-pass filters or other ripple attenuation techniques [71–73]. The dead time adjustments to avoid shoot-through currents are made by RC circuits on the GPAs board. Transistors temperature is monitored using a thermal camera to ensure that high switching frequency does not reduce the GPAs efficiency.

A two-channel Z gradient coil is used as a Maxwell pair, producing a linear gradient field inside the region of interest. Each coil is made up of 12 turns wound on a cylindrical Plexiglass with a diameter of 25cm. Both coils have almost the same inductance and resistance of 80uH and 200mΩ, respectively. The mutual inductance between the coils is approximately 25µH. The large bulk capacitors

(5600µF) connected to the power supply (V_S) are working to decouple the GPAs from the power supplies and provide the majority of the switching current required by the amplifier. The resistance between power supplies and GPAs was calculated by dividing the measured voltage difference by the current. These parameters are tuned to take into account the effect of cables as well as switches on-resistance (R_{ds-on}).

3.2.8 Gradient Current Measurements

As a proof of concept, two different trapezoids (one with 50A amplitude and the other with 10A) are applied as inputs to the first and second channels of the Z gradient coil. For both channels, the rise time and pulse duration are 200us and 8ms, respectively. Each channel is driven by an independent amplifier and power supply (Agilent-N8740A, 150V maximum voltage). The currents are measured using Agilent-1146B AC/DC current probe on the lab bench (Figure 3.4B).

Current measurements are also performed before imaging with the gradient coil placed into the scanner bore. Upon switching on/off the gradient coil, decaying oscillations are observed on the gradient current. While the exact mechanism is not well understood, the mechanical vibration [74, 75] caused by Lorentz forces and/or gradient-induced eddy currents [76] could be the possible sources of this oscillatory behavior.

Because nonlinearities in the system have already been corrected, LTI system theory and thus the gradient current transfer function can be used to compensate for these oscillations. The measured output current (with oscillations) is divided by the desired input in the frequency domain to obtain the current transfer function. Using this transfer function yields a pre-modified input that produces the desired trapezoid at the output.

3.2.9 MRI Experiments

MRI experiments are conducted on Siemens TimTrio 3T scanner. The imaging setup includes the gradient coils connected to the GPAs (outside the scanner room) via a feedthrough panel. Trapezoidal waveforms are used to drive both coils with opposite polarity to generate a linear gradient field. We use a home-built, homogeneous cylindrical phantom (diameter of 10cm) that consists of $CuSO_4$ solution at a concentration of 15 mM/L. A single coronal slice (x-z plane) is imaged using a GRE sequence (5mm slice thickness and 250mm field of view). During the experiments, the scanner Z gradient is inactivated, and the provided Z gradient coil is used to generate the required dephasing and readout gradients with 6.2mT/m strength in the z-direction. The total duration of dephasing and readout gradients are 2250µs and 4500µs, respectively, including the rise/fall times of 220µs. The TE/TR values are 10/20ms. The slice selection and phase encoding gradients are applied via the scanner. A trigger signal is taken from the scanner to synchronize the timings between system gradients and our applied gradient. For RF transmit and receive, a home-built shielded Tx/Rx birdcage coil is placed inside the gradient coil. Figure 3.4C shows the imaging setup.

3.3 Results

3.3.1 State Space Averaging method

Figure 3.5 depicts responses of SSA (Equation 3.8) and topological models to a constant duty cycle (Figure 3.5A) and a varying duty cycle (3kHz sinusoidal waveform, Figure 3.5C) for a single-channel gradient system, validating the accuracy of SSA method in approximating the circuit behavior. The normalized maximum error between the SSA model and the average of topological model (ripples filtered out) for the constant and varying duty cycle are 0.0012% and 0.16%, respectively. This error is duty cycle-dependent, and it increases as the duty cycle increases, as shown in Figure 3.5D. The current ripples (at the switching frequency) are visible in the topological model response (Figure 3.5B) due to GPAs switching behavior. Because of the lack of switching frequency parameters in the SSA model, it cannot simulate ripples.

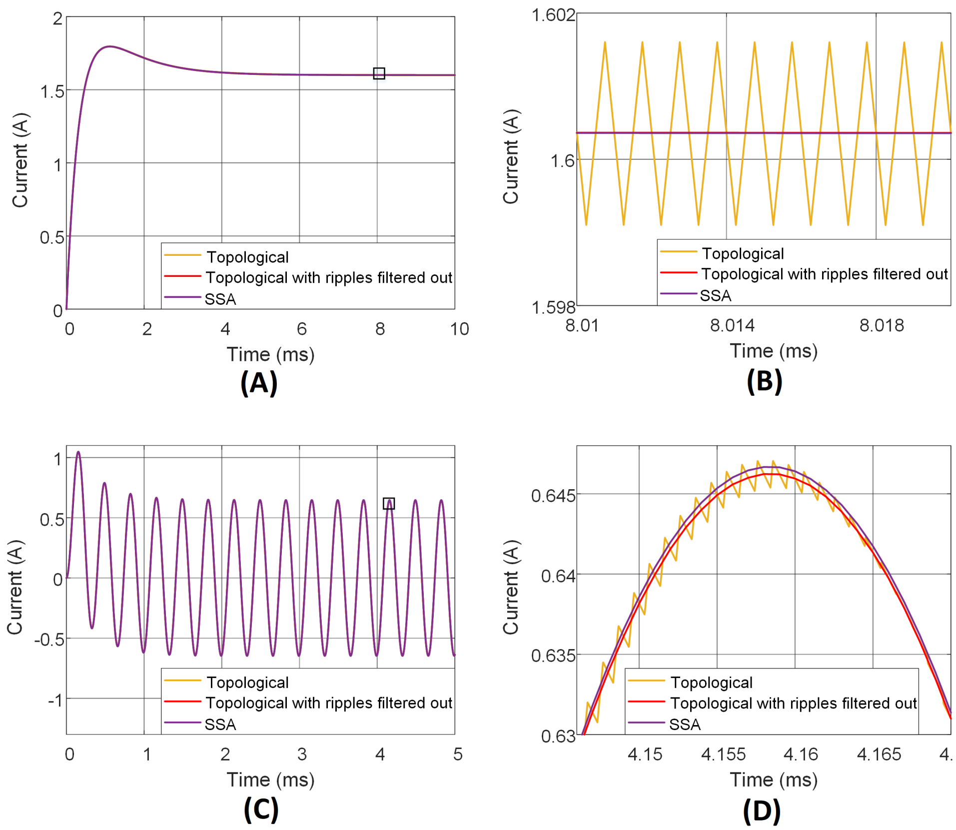

Figure 3.5: Time response comparison of the topological model of gradient system (yellow) and the SSA model (purple). Red curve shows the average of topological model with ripples filtered out. (**A**) Constant duty cycle, $d = 0.5$. (**B**) Zoomed-view of a small region depicted by a square in panel A. The topological model average is precisely followed by the SSA model (normalized maximum error $= 0.0012\%$). (**C**) Varying duty cycle (3kHz sinusoidal), and (**D**) Zoomed-view of the region specified by a square in panel C. Even in this case, varying duty cycle, the SSA gives an excellent approximation of the topological model (normalized maximum error $= 0.16\%$). This error is duty cycle-dependent, and it increases as the duty cycle increases. The frequency of 3kHz (as an example) is used here, which is within the common range of gradient operation frequency.

3.3.2 Feed-forward control simulations

Figure 3.6 compares the performance of the proposed nonlinear controller to that of the linear one when a trapezoidal input is applied. The linear controller produces a constant duty cycle during the flat-top; however, the nonlinear controller provides exponentially increasing duty cycles in that region to compensate for the droop. The maximum difference between these two, occurs near the end of flat-top showing 2.3% increase in the duty cycles.

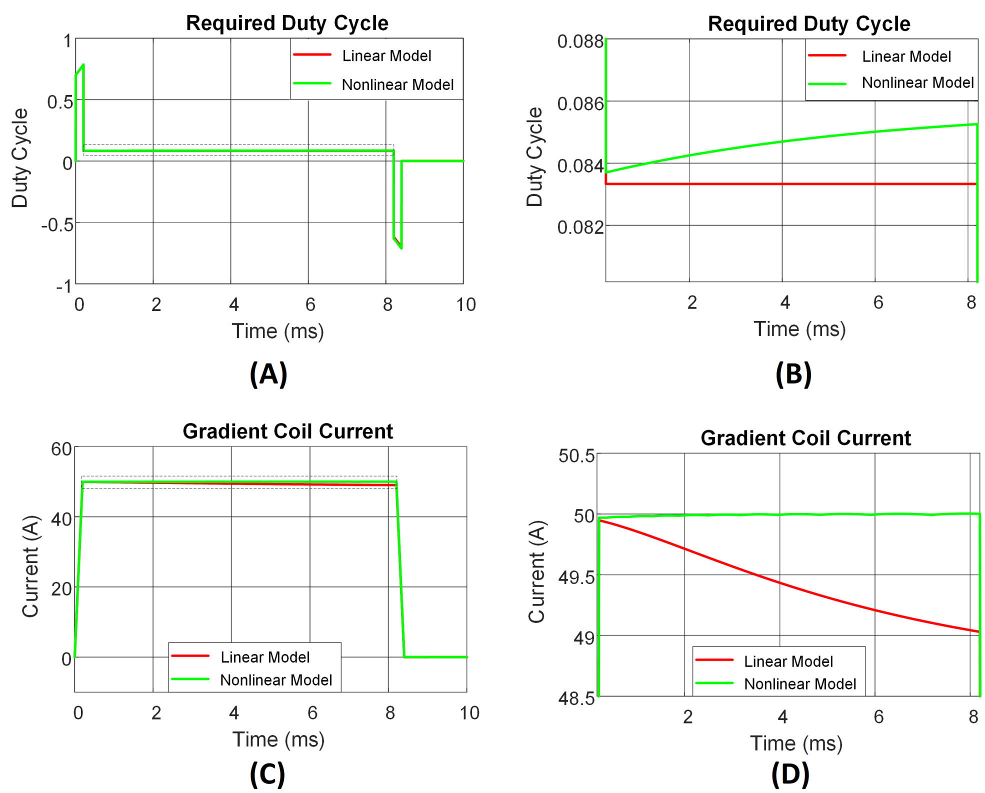

Figure 3.6: Simulation results: (**A**) Calculated required duty cycles for linear first-order and nonlinear second-order models. (**B**) a zoomed-in view of the flat-top region, which clearly shows the difference between the output of linear and nonlinear controllers. (**C**) The gradient coil's current after applying the duty cycles acquired in (A). It demonstrates that the nonlinear controller compensates for the current droop over the flat top region. (**D**) a zoomed-in view of C for the flat-top period.

The output currents (gradient coil currents) generated by the linear and nonlinear controllers are shown in Figures 3.6C and 3.6D. Due to the limited resolution of PWM signals, some undesirable low-frequency oscillations (8mA peak-to-peak amplitude) can be seen in the trapezoid plateau, as explained in the discussion. In the simulations, the error of integral for the linear controller is approximately 1.4%, whereas reduced 1000-fold to negligible levels (0.0014%) when the nonlinear controller is used.

3.3.3 Gradient Current Measurements

Figure 3.7 shows benchtop measurements of coil currents generated by linear and nonlinear controllers. Because there is no feedback loop to regulate the output currents, the current droop is visible in the flat-top region when using the linear controller; however, the nonlinear controller compensates for the droop. The gradient integral errors for the waveforms generated by linear and nonlinear controllers are 1.9% and 0.13%, respectively. The nonlinear controller outperforms the linear one by reducing the error of integral 14-fold, proving its droop compensation capability.

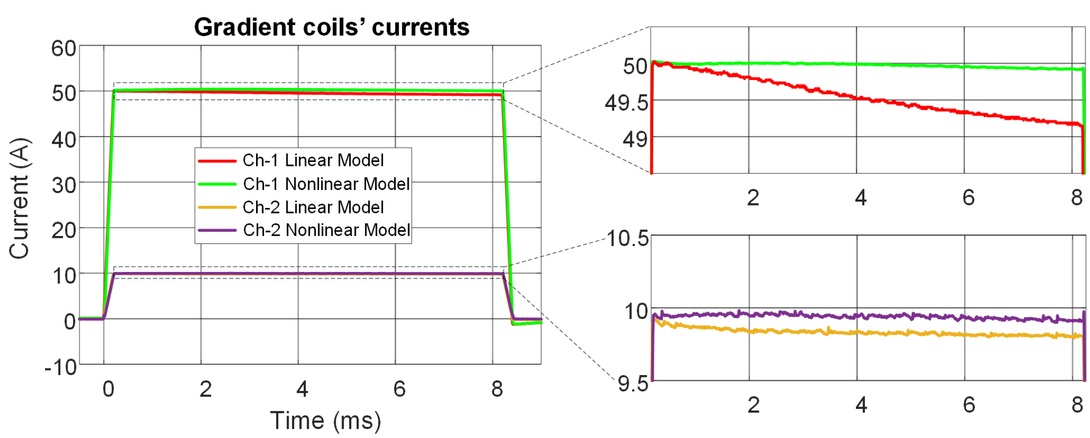

Figure 3.7: Experiment results. The comparison of the coils' currents generated using the linear and nonlinear models. The reference inputs are trapezoid waveforms with the amplitude of 50A and 10A for ch-1 and ch-2, respectively. Both channels have the same rise time (200μs).

Figure 3.8 depicts the gradient coil current generated by the nonlinear controller when the coil is placed inside the scanner bore, and as explained in section 2.2.7, the oscillatory response can be seen on the current (red waveform) as the gradient turns on and off. Applying a pre-modified input current obtained via the current transfer function suppresses the oscillatory behavior and generates an oscillation-free trapezoid (green waveform).

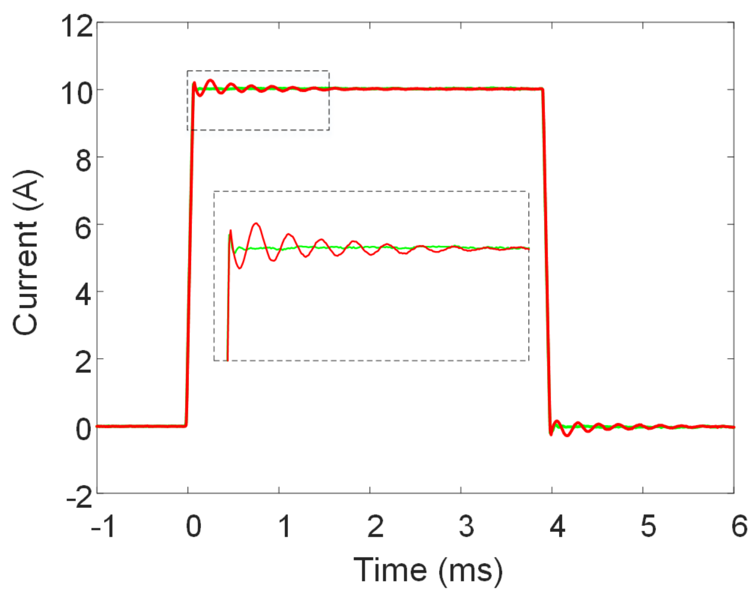

Figure 3.8: Oscillations on the current after switching on/off the gradient coil inside the scanner (the red waveform). These oscillations are removed by using the gradient current transfer function and modifying the input waveform accordingly (the green one).

3.3.4 MRI experiments

Figure 3.9 (first row) shows the phantom images acquired in the coronal plane. The reference image was obtained using the scanner gradients. The uncompensated/compensated image is taken with the home-built Z gradient coil that generates readout gradients using the linear/nonlinear controller. Droop in the readout gradient causes the gradient magnitude to deviate from its desired value, resulting in image deformation (shrinking) along the readout direction. Yellow arrows indicate these deformations. The nonlinear controller, which compensates for the droop and provides almost the desired gradient waveform, corrects these deformations. The difference images (uncompensated and compensated images are subtracted from the reference image) are shown in the second row. The line profiles of difference images show an error in the intensity of 6 pixels for the uncompensated image (red line), which is nearly corrected in the compensated image (green line). Although the intensity of images taken with our gradient coil is higher than the reference image in some areas, the main goal is to compare the performance of linear and nonlinear controllers. These images validate the claim that in a gradient system without feedback control, the gradient chain should be treated as a nonlinear system and use a nonlinear feed-forward controller to eliminate the GPA and power supply imperfections.

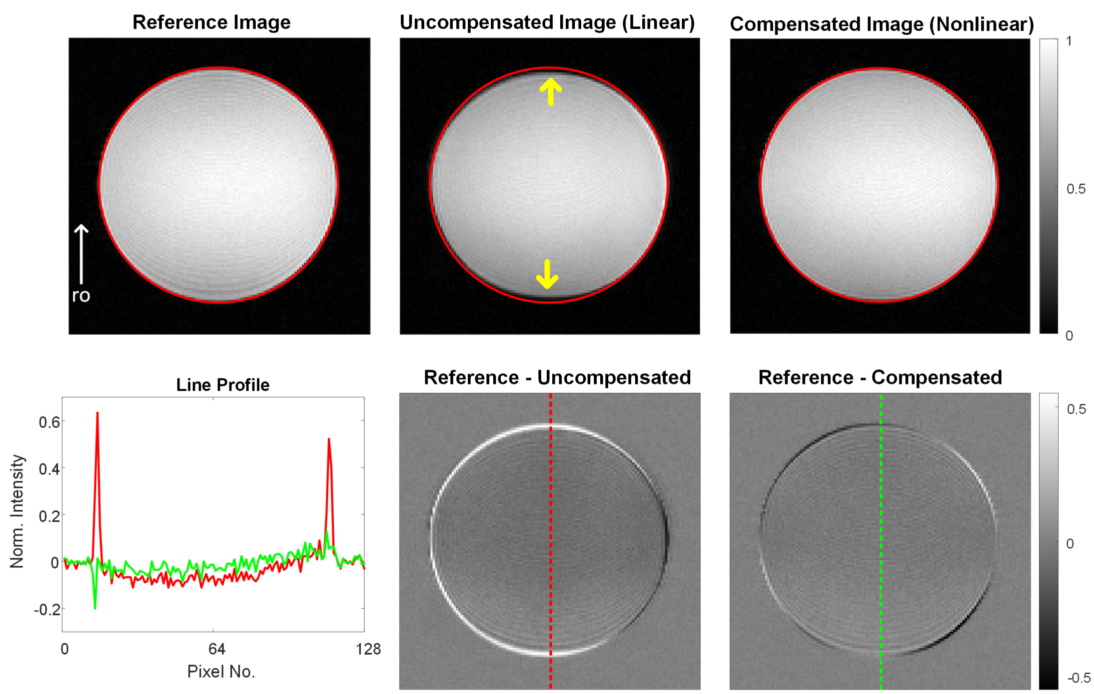

Figure 3.9: Phantom images acquired in the coronal plane using the GRE pulse sequence (single slice). The uncompensated and compensated images are taken by applying the currents provided with the linear and nonlinear models, respectively, as a readout gradient (in z direction, indicated by white arrow). The droop in the readout gradient when using the linear model results in image deformation (shrinking) indicated by yellow arrows. The normalized error images and the line profiles show a significant improvement in the image quality for the compensated image (acquired using the nonlinear model).

3.4 Discussion

In this study, a modified state-space averaging method was used to characterize the gradient system. The nonlinear effects of switching gradient power amplifiers were formulated, and a method to compensate for the current droop was proposed. The SSA method has been used in the literature [27] to model the transfer properties of the power converters by linearizing the equations around an operating point; however, to find an accurate model for the gradient system, we considered the nonlinear equations. The main assumption in this method is the approximation of the fundamental matrix by its first-order linear term, which is applicable in our case due to high-frequency PWMs. Using high-order terms will, of course, improve modeling accuracy; however, the first-order term is preferred to avoid the calculation complexity. In the circuit model, the amplifier switches (MOSFETs) are replaced by ideal switches and series resistances (Rds-on), the gradient coil is modeled as an inductance in series with a resistance, and the power supply stage is represented only with an ideal DC voltage source and an RC circuit. Considering the parasitic elements in the circuit model would result in a more accurate characterization. Therefore, the gradient system was modeled as a nonlinear, time-invariant system. The digital inverse of this model was used in the feed-forward path (open loop) to control the PWMs duty cycle and thus the output current.

The gradient system model and consequently the feed-forward controller (both linear and nonlinear models) are susceptible to the circuit parameters. The circuit model lumped elements are assumed to be constant in the operating bandwidth, but resistances may change due to temperature variation and affect the output gradient current. The feed-forward controller is also prone to external disturbances like eddy currents and mechanical vibrations. These issues are related to the gradient coil, but the focus of this work is on the investigation of nonlinearities associated with the GPA. Although resistances of the GPA switches (Rds-on) are also temperature-dependent, the coil resistance (including connection cables) is dominant, so the GPA thermal effects on the output current are negligible.

We used low duty cycle (5%) pulses in measurements to distinguish GPAs nonlinearity from the coil thermal effects. The thermal effects due to temperature-dependent resistances are mostly related to the gradient coil and not the amplifier; therefore, for high-duty cycle applications, the assessment of gradient coil thermal behavior is necessary. The coil thermal behavior can also be characterized, and temperature-dependent parameters of the feed-forward controller can be updated adaptively based on the thermal model.

Although a closed-loop feedback (PID) controller can achieve similar results on its own, it requires high precision current sensors, which significantly raises the system cost for array [15] or multi-coil [18] systems with increased channels. The performance of feedback and feed-forward controllers can also be compared, which is left for future investigations. The combination of feed-forward and feedback controllers [77] can also be used to eliminate residual errors caused by time-varying (temperature-dependent) parameters, eddy currents, and mechanical vibrations; in this case, the nonlinear feed-forward controller markedly reduces the load of the feedback loop.

High-resolution PWM signals [67] are essential for the proper functionality of the nonlinear controller. In some regions (for example, the trapezoid plateau), the difference in the duty cycle of consecutive PWMs is small, and if the PWM generation algorithm does not provide enough resolution to be sensitive to those slight variations, a series of PWMs will have the same duty cycle, resulting in the unwanted low-frequency oscillation at the output current. Here, the PWMs duty cycles are generated with 15 bits, corresponding to a temporal resolution of less than 80ps, minimizing those oscillations. The oscillations mentioned above are distinct from the current ripples caused by the switching nature of amplifiers [71].

One of the benefits of high-frequency switching PWMs is the reduction of output current ripples. As the switching frequency increases, the current ripples become small enough that LC filter stages at the GPA output are no longer required, resulting in additional cost savings. In the case of using ripple cancelation filters, the gradient system characterization should take into account the filter circuit model as well. Another potential advantage is the broadening of the operational bandwidth, even in closed-loop controllers. As a result of the shorter dwell time, gradient waveforms with higher slew rates (lower rise time) can be generated.

The nonlinear feed-forward controller is also applicable for varying loads. Because the feed-forward controller depends on the system model (circuit parameters), any changes in the parameters must be reflected into the feed-forward controller. For example, in the case of driving a group of coil elements with a single amplifier by means of switching circuits [78], coil-related parameters of the controller must be updated. This is easily accomplished by storing all coil parameters in the FPGA memory and loading the corresponding one when switching between coil elements occurs.

In the recently introduced array coils or multi-coil technique, gradient coils have lower inductances than conventional ones; thus, it is possible to achieve the required current waveforms (with desired amplitude and slew rate) by applying lower voltages. As the voltage/current ratio decreases, the current droop at the plateau region of trapezoid waveform increases, and minor distortions appear in the rise/fall portions. Applying higher voltages (to achieve the same current) might minimize the droop effect, but it increases the needed power and hardware cost. The proposed method compensates for the droop by adjusting the PWMs duty cycles while using the optimum supply voltages.

Sizeable high voltage capacitors (decoupling capacitors) connected in parallel to the power supplies are responsible primarily for high switching voltages and currents (rise/fall portions of the trapezoid). Since the maximum required voltage for the array coils is less than the conventional coils, smaller capacitors with lower voltage can be used. Although lowering the capacitor value may result in more droop, it does not affect the output current since the capacitor voltage droop is considered in the nonlinear model calculations. As a result, the proposed method allows for smaller capacitors, lowering system costs and physical space requirements without compromising output quality.

In our experiments, the proposed method was only tested on the Z gradient and the readout gradient of a simple GRE sequence as a proof of concept; however, we expect similar results and performance for X and Y gradients because the gradient chain circuit is the same for all three axes, and it can also be used to generate any gradient waveform and compensate for the current droops. The effect of droop in the gradient current waveforms can be more pronounced in other applications such as EPI and DWI, which requires long pulses or high gradient strength, resulting in signal drop and image artifacts.

Chapter 4

Adaptive Feed-forward Control of Gradient Currents Using Gradient Heating Prediction

Preface

First part of this chapter was presented at the Joint Annual Meeting of International Society for Magnetic Resonance in Medicine-European Society of Magnetic Resonance in Medicine and Biology [79]. The findings of second part were submitted and accepted for presentation at the Annual Meeting of International Society for Magnetic Resonance in Medicine in June 2023 [80]. Some aspects of this chapter including controller implementation, temperature measurements, and pulse sequence development are done with the help of Ege Aydin. This chapter's content is being prepared for publication in a journal, with Ege Aydin as the first author.

4.1 Introduction

Accurate gradient fields are mandatory for spatial encoding in MRI, and any deviation from predefined gradient waveforms results in image artifacts. One source of perturbation is gradient heating due to ohmic losses in the coils and power amplifier. The gradient heating increases the total resistance of the gradient system, which alters the current flowing through the coils if there is no feedback in the system. Feedback control based on measuring the output current can eliminate this perturbation [66,77]; however, it necessitates expensive current sensors. Feed-forward control [15, 51] based on the linear time-invariant (LTI) model is susceptible to thermal variations because of the underlying assumption of time invariance. As a result, model parameters deviate from the expected values. This work aims to model the thermal variation of gradient system to predict and update feed-forward control parameters. Two approaches are proposed: the first involves measuring the temperature of the coil windings and solving the thermal equation numerically, which can only predict gradient coil effects. Second, the electrical parameters are measured in order to model the gradient coil and power amplifier simultaneously. The proposed system is free from expensive current sensors, and therefore it reduces the cost of the gradient array technology.

4.2 Methods

4.2.1 First approach: Measuring the temperature

The LTI model used in feed-forward controllers is:

$$V(t) = L_C \frac{dI(t)}{dt} + R_C I(t) \tag{4.1}$$

The L_C and R_C parameters in this model are not time-dependent; however, this can be violated due to temperature variation. High currents flowing through the gradient coil cause a temperature rise in various parts of the gradient system, mainly in the coil winding. This increase affects the resistance of the gradient coil (R_C), which alters the output current. The well-known linear relationship between temperature and resistance is as follow [81]:

$$R_C(t) = R_C(t_0)\left(1 + \alpha\left(\theta(t) - \theta(t_0)\right)\right) \tag{4.2}$$

Here α is the temperature coefficient of copper wire. $R_C(t_0)$ and $\theta(t_0)$ are the initial values of coil's resistance and temperature, respectively.

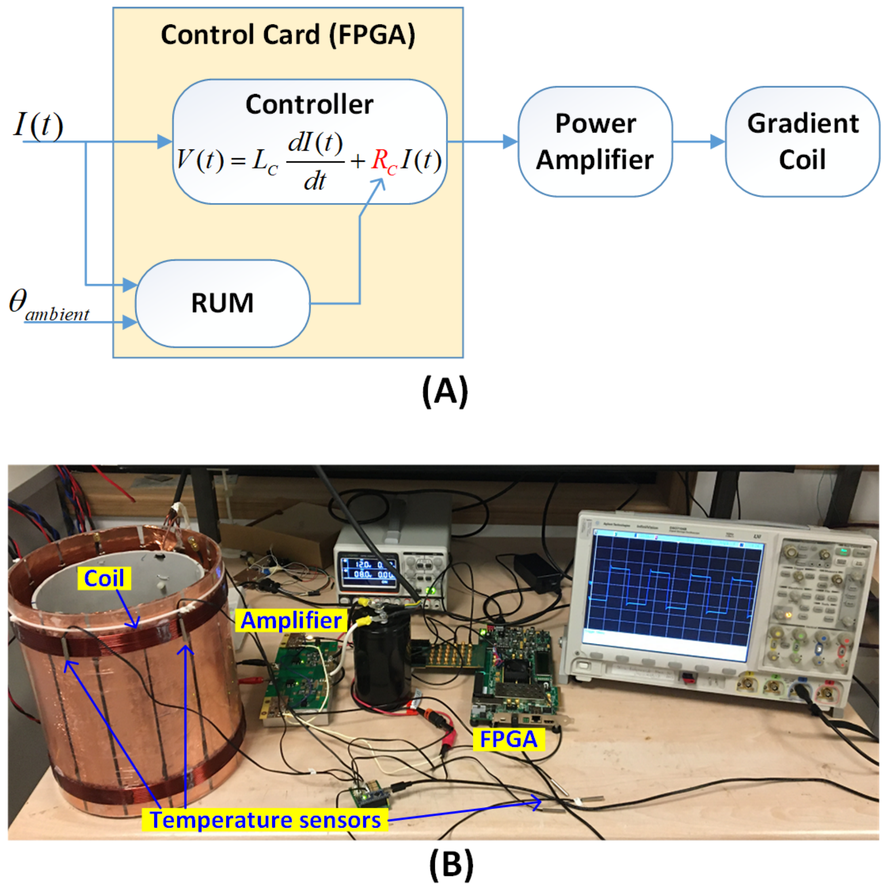

Figure 4.1: (**A**) the block diagram of gradient system with feed-forward controller, including the updating block. (**B**) Measurement setup. There are six temperature sensors; three of them measure the coil winding temperature, and the other three measure the ambient temperature. The average temperature is used in calculations.

To improve the controller performance, the R_C parameter in Equation 4.1 must be updated based on coil temperature. The thermal differential equation determines the temperature of a current-carrying conductor [82].

$$\frac{d\theta}{dt} = k_1 R_C(t) I^2(t) - k_2\left(\theta(t) - \theta_{ambient}\right) \tag{4.3}$$

The solution of this equation is an inverse exponential with a time constant of

$$\tau = \frac{1}{k_2 - k_1 \alpha R_C(t_0) I^2} \tag{4.4}$$

We measure the temperature variation of coil winding while applying a constant voltage to the coil to determine k_1 and k_2. The system block diagram and measurement setup are depicted in Figure 4.1. The resistance updating module (RUM) calculates the temperature and the coil's resistance based on an arbitrary input current waveform and ambient temperature, and updates the R_C parameter in the feed-forward controller. To demonstrate the efficiency of the proposed method, we drive the coil with a 5-minute continuous trapezoidal waveform (non-stop EPI readout, 30A peak current), with and without RUM, and measure the coil current at the start and end of the sequence. To distinguish temperature-dependent effects from the nonlinear imperfections, we also employ a nonlinear model [52] that compensates for the droop originating from system nonlinearities.

4.2.2 Second approach: Measuring electrical parameters

The system setup shown in Figure 4.1B can be modeled with total of three electrical parameters and the equivalent four thermal parameters (Figure 4.2). The electrical parameters $R_L(t)$, $R_{sw}(t)$, and L represent coil series resistance, lumped amplifier switch resistance, and coil inductance. The equivalent thermal model can be represented with R_T and C_T parameters. This is done separately for the lumped amplifier resistance and the coil resistance as they heat and cool at different rates. The thermal model is dependent on the real power loss on the gradient coil while the power is dependent on the thermal model output. Only when a constant current is applied, the thermal model becomes linear and a time constant can be calculated. The time constant equation (Equation 4.4) also implies a maximum current value, above which an exponential increase in temperature occurs.

A calibration sequence is used to determine the model parameters, in which a known arbitrary voltage waveform is applied to the gradient coil via the gradient amplifiers for 6 minutes. Snapshots of the voltage and current waveforms are taken during this time period. Since the electrical system model describes the voltage waveform as a linear combination of current and the time derivative of the current, the instantaneous R and L values can be calculated using the Gram matrix shown below.

$$\begin{bmatrix} \langle I(t), I(t)\rangle & \left\langle I(t), \frac{dI(t)}{dt}\right\rangle \\ \left\langle \frac{dI(t)}{dt}, I(t)\right\rangle & \left\langle \frac{dI(t)}{dt}, \frac{dI(t)}{dt}\right\rangle \end{bmatrix} \begin{bmatrix} R \\ L \end{bmatrix} = \begin{bmatrix} \langle V(t), I(t)\rangle \\ \left\langle V(t), \frac{dI(t)}{dt}\right\rangle \end{bmatrix} \tag{4.5}$$

For each voltage-current pair, the Gram matrix is solved to obtain $R_L(t)$ and L values. Additionally, a single voltage waveform is measured without connecting the coil to find the voltage drop over the amplifier. This allows us to obtain $R_L + R_{sw}$ and L values from the Gram matrix. Since this process is carried out over a 6-minute period, the change in resistance caused by the self-heating of the resistive elements can be observed. The thermal model parameters are fitted to the data using the Adam optimizer [83].

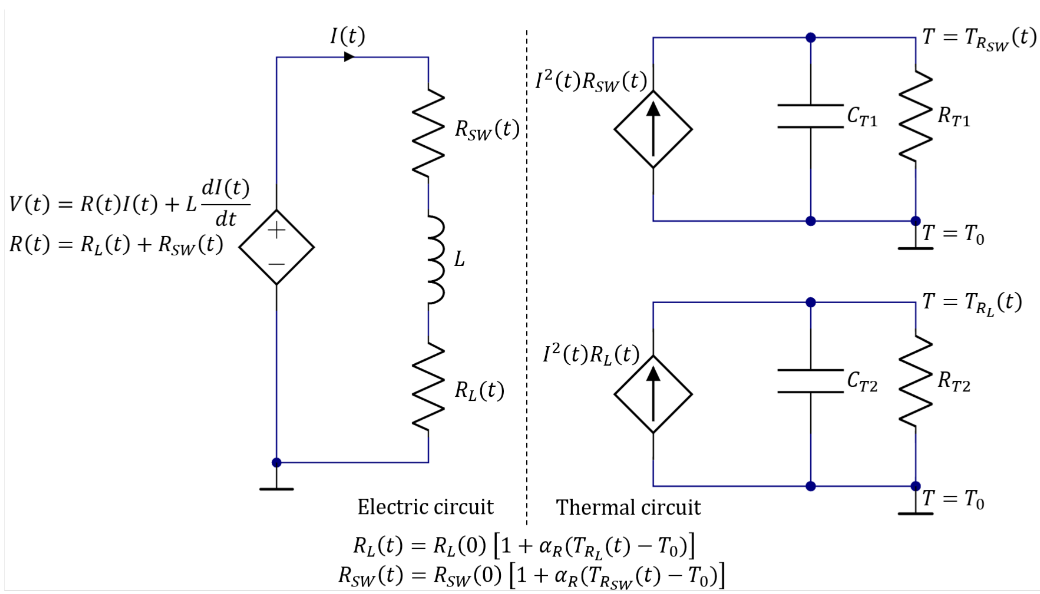

Figure 4.2: The total system model that is separated by the electrical and thermal parts. All temperatures given are effective temperatures stemming from the lumped model.

4.2.3 Controller implementation and MRI experiments

Because the thermal time constant is much larger than the electrical time constant, the thermal model operates independently and updates the resistance parameter of the feed-forward model. The feed-forward controller is implemented digitally on an FPGA evaluation board. The images are obtained using Siemens TimTrio 3T scanner. During the experiments, the scanner Z gradient is inactivated, and the provided Z gradient coil is used to generate the required readout gradients in the z-direction. A trigger pulse is taken from the scanner, synchronizing our applied gradient with the scanner gradients. Since an insert gradient coil is used, a shielded Tx/Rx birdcage coil is used for RF transmission and reception inside the gradient coil.

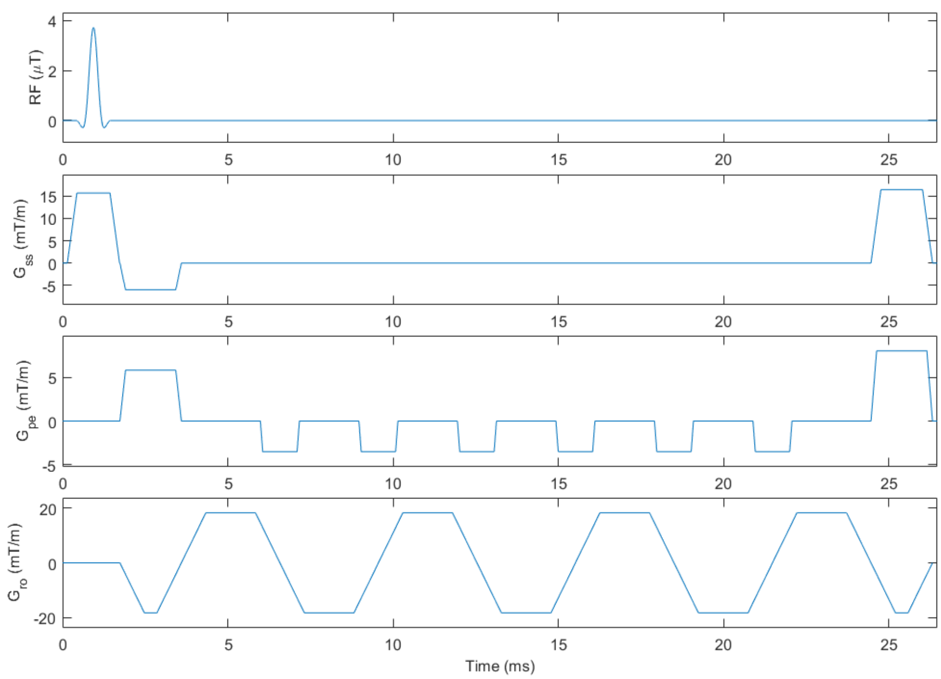

Figure 4.3: Part of a single TR for a single slice of the multi-shot EPI pulse sequence used for imaging. The next shot for the same slice is scanned 156 ms later, making the effective TR for a single slice 156 ms. The next slice is scanned immediately after, which allows maximum use of the readout gradient.

A multi-shot EPI sequence is used for the imaging, which is developed on the open-source Pulseq framework (Figure 4.3). The total scan time to acquire an image is 3.9 seconds (25 TR). One TR scans only 7 lines and lasts 156ms. A total of 6 slices are scanned within one TR. This results in a 25.3A RMS current while the entire sequence takes 6 minutes (92 images). For the phantom, a tomato is used as it is small enough to properly image while having an intricate internal shape that can expose artifacts caused by heat.

4.3 Results

Figure 4.4A depicts a good match between the measured and predicted temperatures of the coil winding, indicating the thermal equation's accuracy. The ambient temperature was 23.3 °C, and by applying a 25A DC current for 25 minutes, the temperature will reach its steady-state (66 °C). Figure 4.4B shows the coil resistance and the current flowing through the coil versus time for the LTI model without the updating feature. As a result of the gradient coil heating, the coil resistance increases, and the current decreases from its starting value. Our measurements show a 3.8% decrease in current, but it is higher for higher amplitude currents.

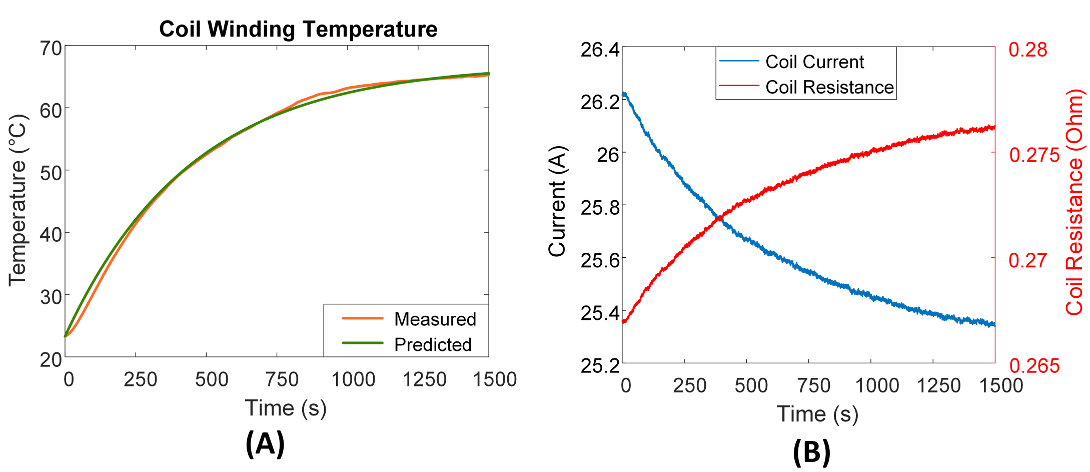

Figure 4.4: Measured and predicted coil temperature are shown in (**A**), demonstrating the accurate prediction of coil temperature variations using the thermal equation. (**B**) depicts the coil current and resistance versus time when a constant voltage is applied to the coil, which indicates an exponentially increase in the resistance and consequently decrease in the current.

Figure 4.5 shows a good agreement between the measured (red) and predicted (green) coil resistances. However, the residual errors could be caused by the heating of the gradient power amplifier, as we only considered coil winding resistance in the thermal equation calculation. The predicted coil resistances when applying a trapezoid current with 50A peak amplitude (10% duty cycle) and EPI readout waveform with 30A peak current are shown in Figure 4.5 (purple and yellow, respectively).

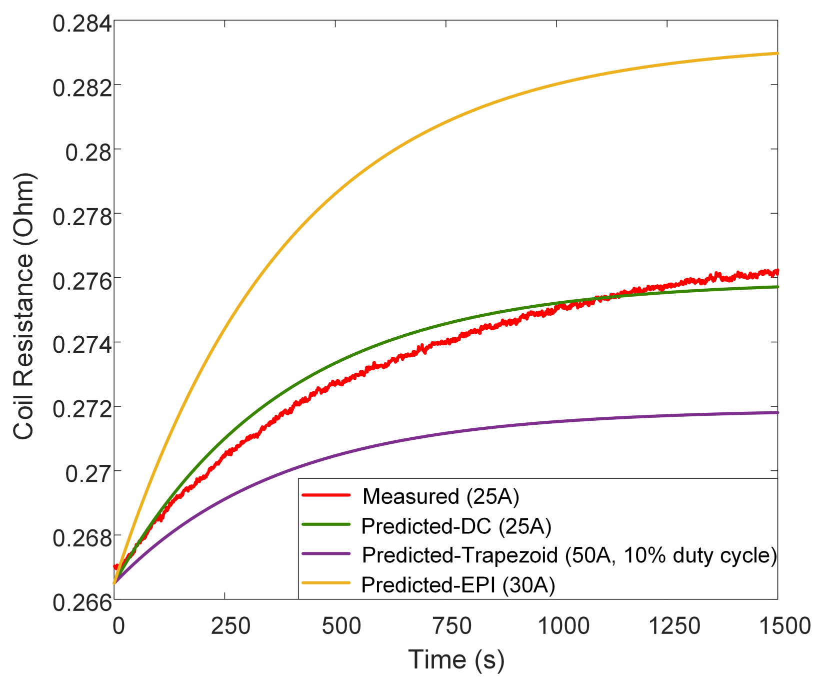

Figure 4.5: The red and green curves show the measured and predicted resistance, respectively. The difference between them is mainly due to the power amplifier heating, which is not considered in the prediction. Applying different current waveforms will result in different predictions; for example, a trapezoid (50A peak amplitude and 10% duty cycle) and EPI ($\pm$30A).

Figure 4.6 demonstrates the coil current measurements at the onset and after 5 minutes while applying the continuous trapezoidal waveform, with and without RUM. The coil's current begins with the desired waveform; however, with fixed model parameters, its amplitude gradually decreases due to gradient heating (Figure 4.6A). The reduction is greater than our predicted value because the power amplifier heating causes an additional reduction in the current. By activating the updating block, the feed-forward controller will be able to provide the desired current at the output, as shown in Figure 4.6B.

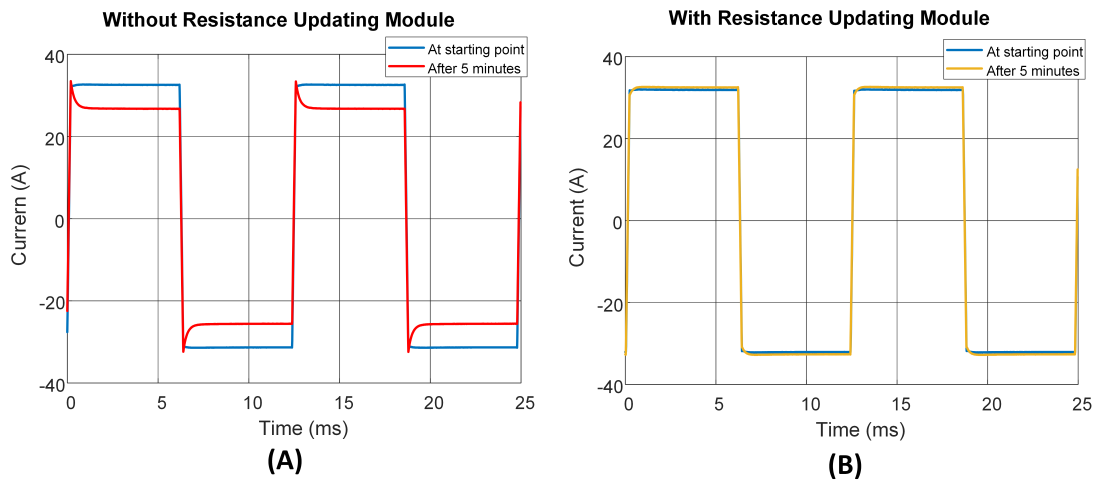

Figure 4.6: A 5-minute EPI waveform was applied to the coil, and the currents were captured at the start and end of the period. (**A**) show the currents without updating the coil resistance in the model, which results in a 17% reduction in the current amplitude after 5 minutes. Adding the updating feature will compensate for the reduction and provide the desired waveform during the operation period (**B**).

The results in Figure 4.4 through 4.6 are related to the first approach which illustrate the effect of gradient coil heating only. Similar results can be achieved for the second approach by including the gradient amplifier heating. The MRI experiments are conducted using the second approach. Figure 4.7 demonstrates that the image shrinks along the readout direction when the gradient coil and power amplifier heat up. Due to the heating, the gradient current reduces during the scan (because of temperature-dependent resistances). As a result, the width of the image reduces gradually.The object width is derived from the total pixel count in the readout direction over some threshold. Images and current waveforms are captured by 90 seconds apart. The current and the image width show around an 18% reduction in 6 minutes. In Figure 4.8, the thermal model compensates for the change in resistance, and the feed-forward controller can provide more reliable gradient currents. Therefore, the image size variations become minimal, with a 2% deviation in the current.

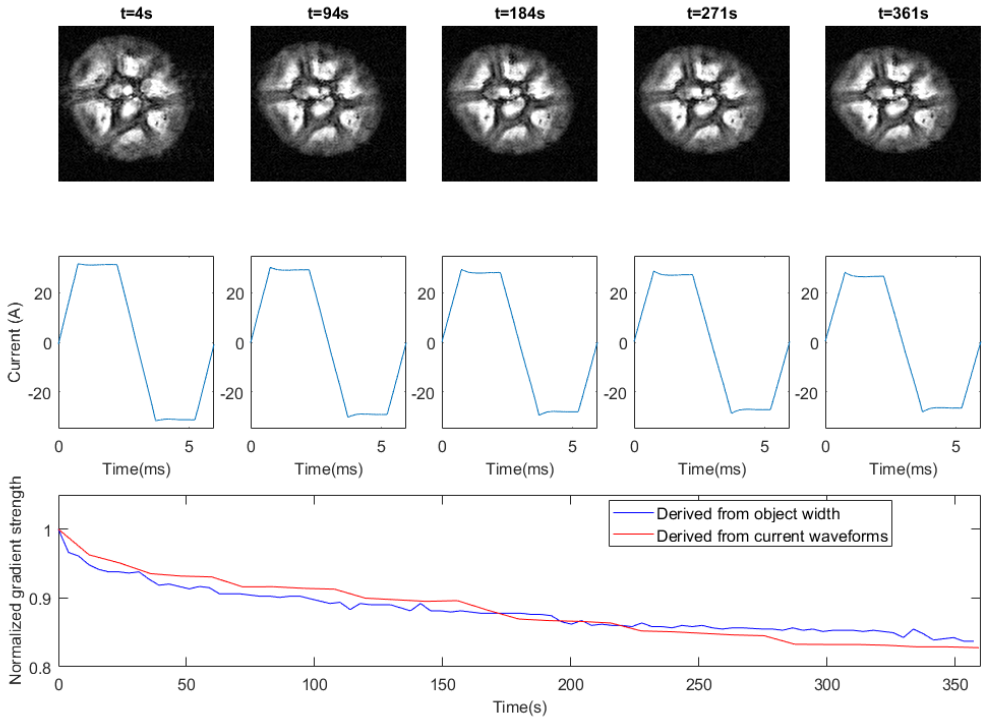

Figure 4.7: MRI experiment results without resistance prediction.

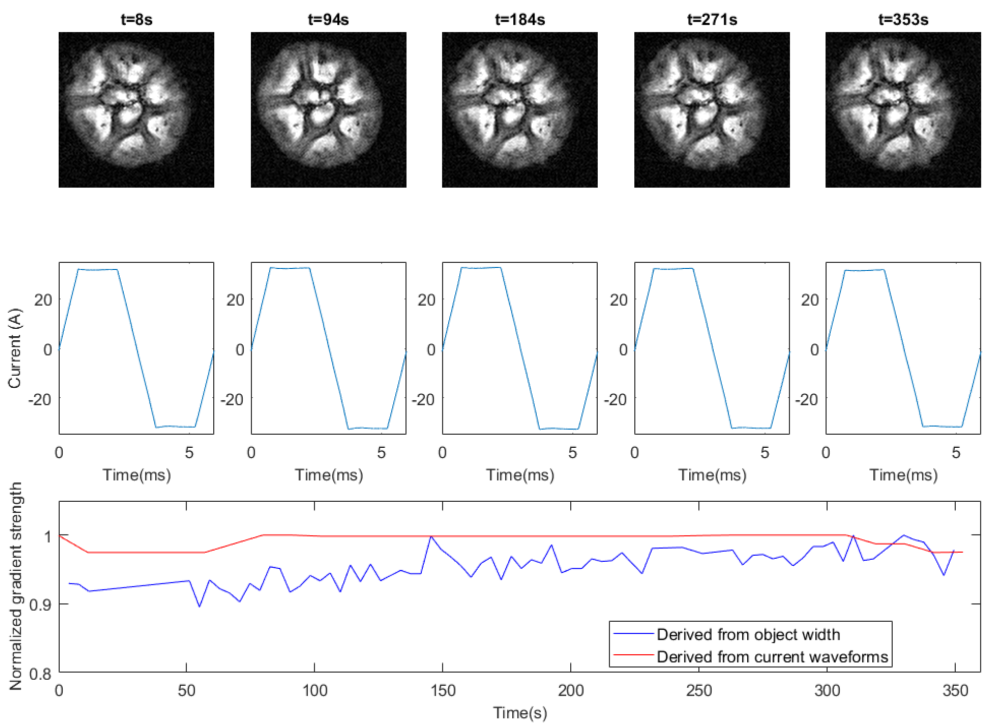

Figure 4.8: MRI experiment results with resistance prediction.

4.4 Discussion

In this chapter, the time-variant parameter of the feed-forward controller was updated by predicting the thermal behavior of the gradient coil and power amplifier. Measurements confirmed that the LTI model, which is prone to time-varying parameters, cannot provide accurate waveforms as variations in the resistive parts alter the output current. According to the results, any increase in resistive parts, decreases the output current and, consequently, the gradient field strength. Due to the deviation of generated readout gradient from the desired gradient, image deformations are visible in the readout direction. Such effects are more noticeable with dense pulse sequences that heat the system quickly, such as the ones used for fMRI applications. The proposed method updates the LTI model parameters to achieve the target gradient waveform. In order to further reduce the error in parameters prediction, higher order models can be implemented. Due to the lack of a water cooling system, measurements were conducted with currents less than 30A. We expect the accurate functionality of the proposed methods in the presence of cooling system, which will only change the rate of heat transfer and thus the system time constant.

Chapter 5

Discussion and Conclusion

In Chapter 2, we discussed how to use gradient array technology to minimize the induced electric field caused by switching gradient waveforms. Understanding and predicting peripheral nerve stimulation caused by gradient coils necessitates a thorough understanding of electromagnetic fields induction in the body and their interaction with nerve fibers. However, the maximum induced electric field is a commonly used measure of the PNS thresholds due to its simple determination from the input waveforms. Conventional coils are designed for a fixed ROL with a specific linearity error, and these parameters, which are important in determining the E-fields, cannot be changed after the coil is manufactured. Even after fabrication, an array design can be optimized using various combinations of feeding currents. Firstly, a Z gradient array coil was used to generate a target magnetic field within a flexible shape ROL while considering E-field thresholds as a constraint. The results demonstrated that induced E-field in a heterogeneous body model could be significantly reduced when the linear gradient is required in a small region (disk-shaped ROL). It was shown that E-fields could be reduced even further by including an E-field constraint in the optimization process. In this chapter, a limited set of volumetric pixels (2000 pixels with the highest E-field value) were used for the E-filed constraint to reduce the computational time, which may affect optimization performance. Secondly, a whole-body gradient array that included all three gradients (X, Y, and Z) was introduced. We developed an optimization problem with the peak induced E-field as the objective function and the current amplitudes as unknown parameters. The coil dimensions and winding pattern were fixed during the optimization, but other engineering metrics such as ROL, field linearity, torque, the magnetic field at the cryostat, and maximum applied current were flexible. By optimizing the currents, minimum E-field design was achieved for various cases: 1) whole-body imaging or standard mode operation, 2) small spherical ROL for head imaging with flexible linearity error, 3) disk-shaped ROL or slice-based gradient field generation, and 4) an off-center oblique slice. We did not attempt to optimize the gradient array coil design in this preliminary work. For example, coil dimensions, X and Y coil winding patterns, shielding performance, and power consumption are chosen in a manner similar to a conventional gradient coil designed by Sim4Life software. A simplified body model with uniform interior electrical properties was used for the E-field calculation in this study; however, similar performance is expected for heterogeneous body models. The optimization problem can be modified to maximize the gradient strength (with a constant slew rate) while considering the E-field (PNS) thresholds as a nonlinear inequality constraint. Alternatively, the gradient array coil can be optimized to achieve the highest possible gradient strength and slew rate without causing PNS.

As discussed in Chapter 3, providing accurate gradient coil currents might be challenging due to hardware imperfections. Conventional gradient systems use closed-loop feedback controllers to track the command input current precisely. Thus, they require high-precision high-cost current sensors. Gradient array systems utilize multiple gradient coils and hence need many current sensors for the feedback loop, which significantly increases the system cost. Therefore, feed-forward controllers might be preferable to avoid using measurement data and expensive current sensors. Because the gradient chain is generally nonlinear, using linear models cannot compensate for imperfections coming from nonlinearities. To address this issue, a nonlinear second-order model (feed-forward controller) was introduced for the gradient chain, including the gradient coil, gradient power amplifier, and power supply. The focus of this work was the investigation of nonlinearities associated with the GPA and compensation for GPA's imperfections rather than the gradient coil's. A new technique for generating high-switching and high-resolution pulse width modulation to drive power amplifiers was introduced to ensure the proper functionality of the proposed controller. Experimental measurements and MRI images depicted the performance of the feed-forward controller in nonlinear droop compensation. The gradient system model, and thus the feed-forward controller, is susceptible to the circuit parameters. The circuit model's lumped elements were assumed to be constant over the operating bandwidth, but resistances can change due to temperature variation, affecting the output gradient current.

To address the gradient heating issues, two approaches were proposed in Chapter 4. First, to consider time-varying parameters (temperature-dependent resistances) in the feed-forward controller, it is possible to measure the gradient coil temperature and update the controller coefficients in real-time. To accomplish this, the temperature variations of the system were measured once, and the variations of controller coefficients were predicted by solving the thermal equation based on the measurement data. In the second approach, the electrical parameters were measured in order to model the gradient coil and power amplifier simultaneously. A calibration sequence (arbitrary voltage waveform) was applied to the gradient coil via the gradient amplifiers for 6 minutes. Snapshots of the voltage and current waveforms were taken during this time period. For each voltage-current pair, the Gram matrix was solved to obtain the controller coefficients. Due to the lack of a water cooling system, measurements were conducted with currents less than 30A. We expect the accurate functionality of the proposed methods in the presence of a cooling system, which will only change the rate of heat transfer and, thus, the system time constant.

In this PhD thesis we focused on two main goals: first, gradient array coils were used to increase PNS thresholds by minimizing induced E-fields. Second, improving the hardware performance of gradient array technology and lowering its cost through the use of feed-forward controllers. Gradient systems are an essential part of magnetic resonance scanners because the spatial distribution of gradient fields encodes the spin locations. Converting conventional gradient coils into an array system necessitates some hardware challenges in exchange for a significant increase in gradient field design flexibility. In [16], some hardware challenges and solutions for a gradient array system were discussed. Most gradient coil design parameters can be adjusted even after fabrication with a gradient array coil simply by optimizing the feeding current. The choice of these parameters can significantly impact the performance of gradient coils. This means that existing MRI scanners can be upgraded to include array technology to provide more specialized and advanced functionalities. We only demonstrated the use of array design to reduce E-fields here; however, the optimization problem can be formulated for other objective functions such as maximum gradient strength, maximum slew rate, minimum peak linearity error, and minimum RMS current, depending on the requirements of a particular scan. The optimization problem can be performed offline for a variety of applications, and the resulting solutions can be stored in a look-up table; therefore, users can select the mode of operation based on the application. Hardware implementation of the gradient array system is challenging because of the high number of channels. Feed-forward controllers and low-cost GPAs are preferred for array design to reduce total system cost; however, controlling the gradient current becomes more complicated as the number of coils increases due to mutual coupling between the channels. Regarding our simulation results from Chapter 2, the maximum current that the hardware can supply limits the optimization performance. To address this issue, GPAs with high current can be used, raising the system cost. Alternatively, the coil winding can be modified so that a high number of turns are used instead of increasing the current.

In conclusion, this PhD thesis demonstrated the benefit and feasibility of gradient array technology to motivate studies in this field further and accelerate the clinical use of this technology.

Bibliography

[1] P. V. Prasad, “Functional mri of the kidney: tools for translational studies of pathophysiology of renal disease,” *American Journal of Physiology-Renal Physiology*, vol. 290, no. 5, pp. F958–F974, 2006.

[2] D. Hao, T. Ai, F. Goerner, X. Hu, V. M. Runge, and M. Tweedle, “Mri contrast agents: basic chemistry and safety,” *Journal of Magnetic Resonance Imaging*, vol. 36, no. 5, pp. 1060–1071, 2012.

[3] R. P. Monti, P. Hellyer, D. Sharp, R. Leech, C. Anagnostopoulos, and G. Montana, “Estimating time-varying brain connectivity networks from functional mri time series,” *NeuroImage*, vol. 103, pp. 427–443, 2014.

[4] K. Setsompop, R. Kimmlingen, E. Eberlein, T. Witzel, J. Cohen-Adad, J. A. McNab, B. Keil, M. D. Tisdall, P. Hoecht, P. Dietz, *et al.*, “Pushing the limits of in vivo diffusion mri for the human connectome project,” *Neuroimage*, vol. 80, pp. 220–233, 2013.

[5] R. Turner, D. Le Bihan, J. Maier, R. Vavrek, L. K. Hedges, and J. Pekar, “Echo-planar imaging of intravoxel incoherent motion.,” *Radiology*, vol. 177, no. 2, pp. 407–414, 1990.

[6] J. A. McNab, B. L. Edlow, T. Witzel, S. Y. Huang, H. Bhat, K. Heberlein, T. Feiweier, K. Liu, B. Keil, J. Cohen-Adad, *et al.*, “The human connectome project and beyond: initial applications of 300 mt/m gradients,” *Neuroimage*, vol. 80, pp. 234–245, 2013.

[7] J. P. Reilly, “Maximum pulsed electromagnetic field limits based on peripheral nerve stimulation: application to ieee/ansi c95. 1 electromagnetic

field standards," *IEEE transactions on biomedical engineering*, vol. 45, no. 1, pp. 137–141, 1998.

[8] J. P. Reilly, "Peripheral nerve stimulation by induced electric currents: exposure to time-varying magnetic fields," *Medical and Biological Engineering and Computing*, vol. 27, pp. 101–110, 1989.

[9] P. Glover, "Interaction of mri field gradients with the human body," *Physics in Medicine & Biology*, vol. 54, no. 21, p. R99, 2009.

[10] C. Ham, J. Engels, G. Van de Wiel, and A. Machielsen, "Peripheral nerve stimulation during mri: effects of high gradient amplitudes and switching rates," *Journal of Magnetic Resonance Imaging*, vol. 7, no. 5, pp. 933–937, 1997.

[11] B. Zhang, Y.-F. Yen, B. A. Chronik, G. C. McKinnon, D. J. Schaefer, and B. K. Rutt, "Peripheral nerve stimulation properties of head and body gradient coils of various sizes," *Magnetic Resonance in Medicine: An Official Journal of the International Society for Magnetic Resonance in Medicine*, vol. 50, no. 1, pp. 50–58, 2003.

[12] M. Davids, B. Guérin, M. Malzacher, L. R. Schad, and L. L. Wald, "Predicting magnetostimulation thresholds in the peripheral nervous system using realistic body models," *Scientific reports*, vol. 7, no. 1, p. 5316, 2017.

[13] R. Turner, "Gradient coil design: a review of methods," *Magnetic resonance imaging*, vol. 11, no. 7, pp. 903–920, 1993.

[14] N. K. Ertan, *Design and Applications of a Z-Gradient Array in Magnetic Resonance Imaging*. PhD thesis, Bilkent Universitesi (Turkey), 2019.

[15] K. Ertan, S. Taraghinia, and E. Atalar, "Driving mutually coupled gradient array coils in magnetic resonance imaging," *Magnetic resonance in medicine*, vol. 82, no. 3, pp. 1187–1198, 2019.

[16] K. Ertan, S. Taraghinia, A. Sadeghi, and E. Atalar, "A z-gradient array for simultaneous multi-slice excitation with a single-band rf pulse," *Magnetic resonance in medicine*, vol. 80, no. 1, pp. 400–412, 2018.

[17] M. Takrimi and E. Atalar, "A z-gradient array coil with a dedicated active-shielded array coil for mri," *Magnetic Resonance in Medicine*, vol. 88, no. 6, pp. 2718–2731, 2022.

[18] C. Juchem, O. M. Nahhass, T. W. Nixon, and R. A. de Graaf, "Multi-slice mri with the dynamic multi-coil technique," *NMR in Biomedicine*, vol. 28, no. 11, pp. 1526–1534, 2015.

[19] C. Juchem, T. W. Nixon, S. McIntyre, D. L. Rothman, and R. A. de Graaf, "Magnetic field modeling with a set of individual localized coils," *Journal of Magnetic Resonance*, vol. 204, no. 2, pp. 281–289, 2010.

[20] E. Smith, F. Freschi, M. Repetto, and S. Crozier, "The coil array method for creating a dynamic imaging volume," *Magnetic resonance in medicine*, vol. 78, no. 2, pp. 784–793, 2017.

[21] F. Jia, S. Littin, K. J. Layton, S. Kroboth, H. Yu, and M. Zaitsev, "Design of a shielded coil element of a matrix gradient coil," *Journal of Magnetic Resonance*, vol. 281, pp. 217–228, 2017.

[22] S. Littin, F. Jia, K. J. Layton, S. Kroboth, H. Yu, J. Hennig, and M. Zaitsev, "Development and implementation of an 84-channel matrix gradient coil," *Magnetic resonance in medicine*, vol. 79, no. 2, pp. 1181–1191, 2018.

[23] R. Kimmlingen, M. Gebhardt, J. Schuster, M. Brand, F. Schmitt, and A. Haase, "Gradient system providing continuously variable field characteristics," *Magnetic Resonance in Medicine: An Official Journal of the International Society for Magnetic Resonance in Medicine*, vol. 47, no. 4, pp. 800–808, 2002.

[24] H. Lenz, "Gradient amplifier with combined current regulation and differential control," Sept. 10 2002. US Patent 6,448,775.

[25] J. Mahdavi, M. R. Nasiri, A. Agah, and A. Emadi, "Application of neural networks and state-space averaging to dc/dc pwm converters in sliding-mode operation," *IEEE/ASME Transactions On Mechatronics*, vol. 10, no. 1, pp. 60–67, 2005.

[26] R. D. Middlebrook and S. Ćuk, "A general unified approach to modelling switching-converter power stages," *International Journal of Electronics Theoretical and Experimental*, vol. 42, no. 6, pp. 521–550, 1977.

[27] P. Ngamkong, P. Kochcha, K. Areerak, S. Sujitjorn, and K. Areerak, "Applications of the generalized state-space averaging method to modelling of dc–dc power converters," *Mathematical and Computer Modelling of Dynamical Systems*, vol. 18, no. 3, pp. 243–260, 2012.

[28] S. R. Sanders, J. M. Noworolski, X. Z. Liu, and G. C. Verghese, "Generalized averaging method for power conversion circuits," *IEEE Transactions on power Electronics*, vol. 6, no. 2, pp. 251–259, 1991.

[29] J. Xu and C. Lee, "Generalized state-space averaging approach for a class of periodically switched networks," *IEEE Transactions on Circuits and Systems I: Fundamental Theory and Applications*, vol. 44, no. 11, pp. 1078–1081, 1997.

[30] R. Babaloo, M. Takrimi, and E. Atalar, "Increasing peripheral nerve stimulation thresholds using gradient array coils," in *Proceedings of Joint Annual Meeting of ISMRM-ESMRMB. London, UK*, 2022.

[31] R. Babaloo, M. Takrimi, and E. Atalar, "Minimum electric field gradient array body coil with adjustable regions of linearity," in *Proceedings of Annual Meeting of ISMRM. Toronto, Canada*, 2023.

[32] T. K. Foo, E. Laskaris, M. Vermilyea, M. Xu, P. Thompson, G. Conte, C. Van Epps, C. Immer, S.-K. Lee, E. T. Tan, *et al.*, "Lightweight, compact, and high-performance 3 t mr system for imaging the brain and extremities," *Magnetic resonance in medicine*, vol. 80, no. 5, pp. 2232–2245, 2018.

[33] T. K. Foo, E. T. Tan, M. E. Vermilyea, Y. Hua, E. W. Fiveland, J. E. Piel, K. Park, J. Ricci, P. S. Thompson, D. Graziani, *et al.*, "Highly efficient head-only magnetic field insert gradient coil for achieving simultaneous high gradient amplitude and slew rate at 3.0 t (magnus) for brain microstructure imaging," *Magnetic resonance in medicine*, vol. 83, no. 6, pp. 2356–2369, 2020.

[34] J. A. Den Boer, J. D. Bourland, J. A. Nyenhuis, C. L. Ham, J. M. Engels, F. X. Hebrank, G. Frese, and D. J. Schaefer, "Comparison of the threshold for peripheral nerve stimulation during gradient switching in whole body mr systems," *Journal of Magnetic Resonance Imaging: An Official Journal of the International Society for Magnetic Resonance in Medicine*, vol. 15, no. 5, pp. 520–525, 2002.

[35] W. Irnich and F. X. Hebrank, "Stimulation threshold comparison of time-varying magnetic pulses with different waveforms," *Journal of Magnetic Resonance Imaging: An Official Journal of the International Society for Magnetic Resonance in Medicine*, vol. 29, no. 1, pp. 229–236, 2009.

[36] R. E. Feldman, C. J. Hardy, B. Aksel, J. Schenck, and B. A. Chronik, "Experimental determination of human peripheral nerve stimulation thresholds in a 3-axis planar gradient system," *Magnetic Resonance in Medicine: An Official Journal of the International Society for Magnetic Resonance in Medicine*, vol. 62, no. 3, pp. 763–770, 2009.

[37] M. Davids, B. Guérin, V. Klein, and L. L. Wald, "Optimization of mri gradient coils with explicit peripheral nerve stimulation constraints," *IEEE transactions on medical imaging*, vol. 40, no. 1, pp. 129–142, 2020.

[38] M. Davids, B. Guérin, A. Vom Endt, L. R. Schad, and L. L. Wald, "Prediction of peripheral nerve stimulation thresholds of mri gradient coils using coupled electromagnetic and neurodynamic simulations," *Magnetic resonance in medicine*, vol. 81, no. 1, pp. 686–701, 2019.

[39] P. B. Roemer, T. Wade, A. Alejski, C. A. McKenzie, and B. K. Rutt, "Electric field calculation and peripheral nerve stimulation prediction for head and body gradient coils," *Magnetic Resonance in Medicine*, vol. 86, no. 4, pp. 2301–2315, 2021.

[40] P. B. Roemer and B. K. Rutt, "Minimum electric-field gradient coil design: Theoretical limits and practical guidelines," *Magnetic resonance in medicine*, vol. 86, no. 1, pp. 569–580, 2021.

[41] M. Davids, B. Guerin, and L. L. Wald, "A huygens' surface approach to rapid characterization of peripheral nerve stimulation," *Magnetic resonance in medicine*, vol. 87, no. 1, pp. 377–393, 2022.

[42] P. R. Harvey and E. Katznelson, "Modular gradient coil: A new concept in high-performance whole-body gradient coil design," *Magnetic Resonance in Medicine: An Official Journal of the International Society for Magnetic Resonance in Medicine*, vol. 42, no. 3, pp. 561–570, 1999.

[43] S. S. Hidalgo-Tobon, M. Bencsik, and R. Bowtell, "Reducing peripheral nerve stimulation due to gradient switching using an additional uniform field coil," *Magnetic Resonance in Medicine*, vol. 66, no. 5, pp. 1498–1509, 2011.

[44] A. L. Hodgkin and A. F. Huxley, "Resting and action potentials in single nerve fibres," *The Journal of physiology*, vol. 104, no. 2, p. 176, 1945.

[45] V. Klein, M. Davids, L. R. Schad, L. L. Wald, and B. Guérin, "Investigating cardiac stimulation limits of mri gradient coils using electromagnetic and electrophysiological simulations in human and canine body models," *Magnetic resonance in medicine*, vol. 85, no. 2, pp. 1047–1061, 2021.

[46] IEC, "Medical electrical equipment—part 2-33: particular requirements for the basic safety and essential performance of magnetic resonance equipment for medical diagnosis," *Geneva: International Electrotechnical Commission 60601-2-33*, 2015.

[47] B. A. Chronik and B. K. Rutt, "Simple linear formulation for magnetostimulation specific to mri gradient coils," *Magnetic Resonance in Medicine: An Official Journal of the International Society for Magnetic Resonance in Medicine*, vol. 45, no. 5, pp. 916–919, 2001.

[48] M.-C. Gosselin, E. Neufeld, H. Moser, E. Huber, S. Farcito, L. Gerber, M. Jedensjö, I. Hilber, F. Di Gennaro, B. Lloyd, *et al.*, "Development of a new generation of high-resolution anatomical models for medical device evaluation: the virtual population 3.0," *Physics in Medicine & Biology*, vol. 59, no. 18, p. 5287, 2014.

[49] R. A. Lemdiasov and R. Ludwig, “A stream function method for gradient coil design,” *Concepts in Magnetic Resonance Part B: Magnetic Resonance Engineering: An Educational Journal*, vol. 26, no. 1, pp. 67–80, 2005.

[50] M. Takrimi and E. Atalar, “A novel method to estimate and control the eddy power loss within the cryostat: A co-simulation approach to tune z-gradient array coil,” in *Proceedings of Annual Meeting of ISMRM. Toronto, Canada*, 2023.

[51] R. Babaloo, S. Taraghinia, and E. Atalar, “Droop compensation of gradient current waveforms in gradient array systems,” in *Proceedings of the 29th Annual Meeting of ISMRM, Virtual Exhibition*, 2021.

[52] R. Babaloo and E. Atalar, “Nonlinear droop compensation for current waveforms in mri gradient systems,” *Magnetic Resonance in Medicine*, 2022.

[53] P. S. Kundur and O. P. Malik, *Power system stability and control*. McGraw-Hill Education, 1994.

[54] H. Lenz, “Circuit arrangement, gradient amplifier, and method for compensating for nonlinearities of an amplifier output stage,” Feb. 20 2018. US Patent 9,897,673.

[55] T. Scheel and C. Hattrup, “Gradient amplifier with compensation for dead time and forward voltage,” July 17 2018. US Patent 10,024,937.

[56] A. E. Campbell-Washburn, H. Xue, R. J. Lederman, A. Z. Faranesh, and M. S. Hansen, “Real-time distortion correction of spiral and echo planar images using the gradient system impulse response function,” *Magnetic resonance in medicine*, vol. 75, no. 6, pp. 2278–2285, 2016.

[57] J. Rahmer, P. Mazurkewitz, P. Börnert, and T. Nielsen, “Rapid acquisition of the 3d mri gradient impulse response function using a simple phantom measurement,” *Magnetic Resonance in Medicine*, vol. 82, no. 6, pp. 2146–2159, 2019.

[58] S. J. Vannesjo, N. N. Graedel, L. Kasper, S. Gross, J. Busch, M. Haeberlin, C. Barmet, and K. P. Pruessmann, “Image reconstruction using a gradient

impulse response model for trajectory prediction," *Magnetic resonance in medicine*, vol. 76, no. 1, pp. 45–58, 2016.

[59] S. J. Vannesjo, M. Haeberlin, L. Kasper, M. Pavan, B. J. Wilm, C. Barmet, and K. P. Pruessmann, "Gradient system characterization by impulse response measurements with a dynamic field camera," *Magnetic resonance in medicine*, vol. 69, no. 2, pp. 583–593, 2013.

[60] S. J. Vannesjo, Y. Duerst, L. Vionnet, B. E. Dietrich, M. Pavan, S. Gross, C. Barmet, and K. P. Pruessmann, "Gradient and shim pre-emphasis by inversion of a linear time-invariant system model," *Magnetic resonance in medicine*, vol. 78, no. 4, pp. 1607–1622, 2017.

[61] S. Kronthaler, J. Rahmer, P. Börnert, M. R. Makowski, B. J. Schwaiger, A. S. Gersing, and D. C. Karampinos, "Trajectory correction based on the gradient impulse response function improves high-resolution ute imaging of the musculoskeletal system," *Magnetic Resonance in Medicine*, vol. 85, no. 4, pp. 2001–2015, 2021.

[62] T. Knopp, S. Biederer, T. F. Sattel, M. Erbe, and T. M. Buzug, "Prediction of the spatial resolution of magnetic particle imaging using the modulation transfer function of the imaging process," *IEEE transactions on medical imaging*, vol. 30, no. 6, pp. 1284–1292, 2011.

[63] M. Stich, T. Wech, A. Slawig, R. Ringler, A. Dewdney, A. Greiser, G. Ruyters, T. A. Bley, and H. Köstler, "Gradient waveform pre-emphasis based on the gradient system transfer function," *Magnetic resonance in medicine*, vol. 80, no. 4, pp. 1521–1532, 2018.

[64] J. Sabate, L. J. Garces, P. M. Szczesny, Q. Li, and W. F. Wirth, "High-power high-fidelity switching amplifier driving gradient coils for mri systems," in *2004 IEEE 35th Annual Power Electronics Specialists Conference (IEEE Cat. No. 04CH37551)*, vol. 1, pp. 261–266, IEEE, 2004.

[65] J. A. Sabate, R. S. Zhang, L. J. Garces, P. M. Szczesny, Q. Li, and W. F. Wirth, "High fidelity, high power switched amplifier," Oct. 3 2006. US Patent 7,116,166.

[66] J. A. Sabaté, R. R. Wang, F. Tao, and S. Chi, "Magnetic resonance imaging power: High-performance mva gradient drivers," *IEEE Journal of Emerging and Selected Topics in Power Electronics*, vol. 4, no. 1, pp. 280–292, 2015.

[67] V. Acikel, A. Dogan, F. E. Filci, G. Cansiz, and E. Atalar, "High resolution pwm generation for high frequency switching gradient amplifier control," in *Proceedings of the 27th Annual Meeting of ISMRM, Montréal, Québec, Canada*, 2019.

[68] C. Z. Cooley, J. P. Stockmann, T. Witzel, C. LaPierre, A. Mareyam, F. Jia, M. Zaitsev, Y. Wenhui, W. Zheng, P. Stang, *et al.*, "Design and implementation of a low-cost, tabletop mri scanner for education and research prototyping," *Journal of Magnetic Resonance*, vol. 310, p. 106625, 2020.

[69] N. Evetts and M. S. Conradi, "Low-cost gradient amplifiers for small mri systems," *Journal of Magnetic Resonance*, vol. 335, p. 107127, 2022.

[70] S. Taraghinia, V. Acikel, R. Babaloo, and E. Atalar, "Design and implementation of high switching frequency gradient power amplifier using egan devices.," in *Proceedings of the 29th Annual Meeting of ISMRM, Virtual Exhibition*, 2021.

[71] J. Sabate, M. Schutten, R. Steigerwald, Q. Li, and W. F. Wirth, "Ripple cancellation filter for magnetic resonance imaging gradient amplifiers," in *Nineteenth Annual IEEE Applied Power Electronics Conference and Exposition, 2004. APEC'04.*, vol. 2, pp. 792–796, IEEE, 2004.

[72] S. Taraghinia, K. Ertan, and E. Atalar, "Minimum current ripple in the gradient array system by applying optimum-phase pulse-width modulation pattern," in *Proceedings of the 25th Annual Meeting of ISMRM, Honolulu, Hawaii*, 2017.

[73] S. Taraghinia, K. Ertan, and E. Atalar, "Efficient ripple current reduction in gradient array system using optimized-phase control signals with one stage lc filter," in *Proceedings of the 34th Annual Meeting of ESMRMB, Barcelona, Spain*, 2017.

[74] G. Yao, C. Mechefske, and B. Rutt, "Characterization of vibration and acoustic noise in a gradient-coil insert," *Magnetic Resonance Materials in Physics, Biology and Medicine*, vol. 17, no. 1, pp. 12–27, 2004.

[75] T. W. Nixon, S. McIntyre, D. L. Rothman, and R. A. de Graaf, "Compensation of gradient-induced magnetic field perturbations," *Journal of Magnetic Resonance*, vol. 192, no. 2, pp. 209–217, 2008.

[76] L. Ryner, P. Stroman, T. Wessel, D. Hoult, and J. Saunders, "Effect of oscillatory eddy currents on mr spectroscopy," in *Proc 6th Annual Meeting ISMRM, Sydney*, vol. 1903, 1998.

[77] R. Babaloo, S. Taraghinia, V. Acikel, M. Takrimi, and E. Atalar, "Digital feedback design for mutual coupling compensation in gradient array system," in *Proceedings of the 28th Annual Meeting of ISMRM, Virtual Exhibition*, 2020.

[78] S. Kroboth, K. J. Layton, F. Jia, S. Littin, H. Yu, J. Hennig, and M. Zaitsev, "Optimization of coil element configurations for a matrix gradient coil," *IEEE Transactions on Medical Imaging*, vol. 37, no. 1, pp. 284–292, 2017.

[79] R. Babaloo, E. Aydin, and E. Atalar, "Adaptive feed-forward control of gradient currents using gradient heating prediction," in *Proceedings of Joint Annual Meeting of ISMRM-ESMRMB. London, UK*, 2022.

[80] E. Aydin, R. Babaloo, and E. Atalar, "Thermal model in feedforward control of the gradient array system in mri," in *Proceedings of Annual Meeting of ISMRM. Toronto, Canada*, 2023.

[81] D. Halliday, R. Resnick, and K. S. Krane, *Physics, Volume 2*. John Wiley & Sons, 2010.

[82] P. Böckh and T. Wetzel, *Heat transfer: basics and practice*. Springer Science & Business Media, 2011.

[83] D. P. Kingma and J. Ba, "Adam: A method for stochastic optimization," *arXiv preprint arXiv:1412.6980*, 2014.

[84] C. Juchem, S. U. Rudrapatna, T. W. Nixon, and R. A. de Graaf, "Dynamic multi-coil technique (dynamite) shimming for echo-planar imaging of the human brain at 7 tesla," *Neuroimage*, vol. 105, pp. 462–472, 2015.

[85] R. S. Pengelly, S. M. Wood, J. W. Milligan, S. T. Sheppard, and W. L. Pribble, "A review of gan on sic high electron-mobility power transistors and mmics," *IEEE Transactions on Microwave Theory and Techniques*, vol. 60, no. 6, pp. 1764–1783, 2012.

Appendix A

Digital Feedback Design for Mutual Coupling Compensation in Gradient Array System

Preface

The contents of this chapter were presented at the the 28th Annual Meeting of International Society for Magnetic Resonance in Medicine [77]. ASELSAN supplied the current sensors and gradient power amplifiers used in this study.

A.1 Introduction

Gradient array systems have been used to generate dynamically controllable magnetic field profiles [14, 15, 20, 22]. In these systems, multiple gradient coils are driven individually by independent gradient power amplifiers (GPAs). The accuracy of the gradient current waveforms has a significant effect on the image quality and providing gradient coil currents with high fidelity might be challenging due to mutual coupling between coils, GPA imperfections, and time-varying parameters in the gradient hardware. Although considering first-order model of the system in feed-forward including mutual coupling provides adequate currents to the coils [15], residual errors due to measurement errors in the determination of the model parameters, not considering GPAs parameters in the model, high order effects and time-varying parameters can still decrease the accuracy of coil currents time-courses. A closed-loop feedback can be used to overcome these imperfections [24]. In this work, a digital real-time (proportional–integral–derivative) PID controller is designed to compensate for the mutual coupling effect which is not corrected by the feed-forward model. The controller also degrades the current waveforms sensitivity to the time-varying parameters and undesired external disturbances like droop in the supply voltage.

A.2 Methods

The schematic and block diagram of the gradient array system are shown in Figure A.1. A typical trapezoid current waveform is used to drive two channels of Z gradient array coils. The hardware limitations are considered in designing current waveforms. The first-order model including the mutual coupling provides the required voltage. This model acts like a multi-input-multi-output (MIMO) proportional-derivative (PD) controller in the open-loop configuration. The parameters were determined by measuring self-inductance, mutual-inductance, and resistance of coils.

$$\begin{bmatrix} v_1(t) \\ v_2(t) \end{bmatrix} = \begin{bmatrix} L_1 & M \\ M & L_2 \end{bmatrix} \begin{bmatrix} \frac{di_1(t)}{dt} \\ \frac{di_2(t)}{dt} \end{bmatrix} + \begin{bmatrix} R_1 & 0 \\ 0 & R_2 \end{bmatrix} \begin{bmatrix} i_1(t) \\ i_2(t) \end{bmatrix} \tag{A.1}$$

The close-loop feedback PID controller is used in parallel with the feed-forward model which will update the required voltage to minimize the error between the desired input and measured output. The transfer function analysis can be used for the determination of the PID parameters.

$$I_m(s) = \left[\mathrm{I} + G_c(s)G_p(s)\right]^{-1} \left[G_m(s)G_p(s) + G_c(s)G_p(s)\right] I_d(s) \tag{A.2}$$

(A)

(B)

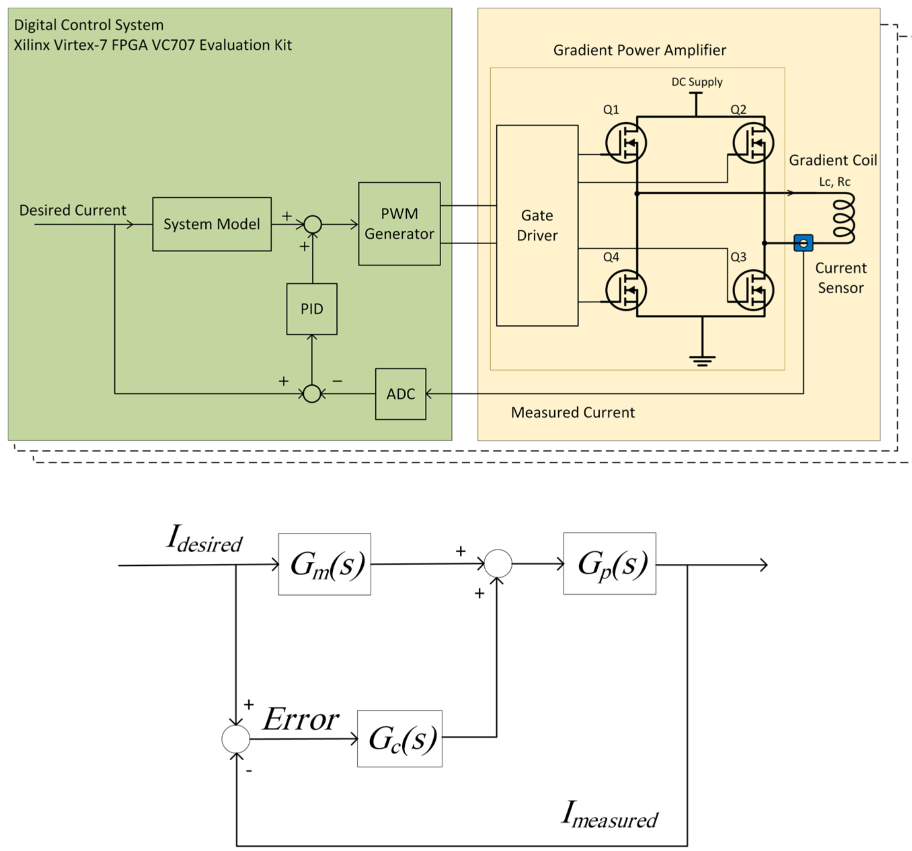

Figure A.1: (**A**) the schematic of the gradient array system. A combination of feed-forward and feedback provides the desired voltage. Generated PWM signals will amplify and apply to the gradient coil. The analog data coming from the current sensor will be digitized and used in the feedback loop. (**B**) All the system can be shown by 3 transfer function blocks in the frequency domain. $G_p(s)$ contains all the analog part. $G_m(s)$ and $G_c(s)$ are the model of system and controller transfer functions, respectively.

Where, $G_m(s)$, $G_p(s)$, and $G_c(s)$ are transfer functions for the system model, gradient coil with amplifier and PID controller respectively. Assuming no mutual coupling and single-input-single-output PID, the transfer function for the channel 1 is as follow:

$$\frac{I_{m1}(s)}{I_{d1}(s)} = \frac{G_{m1}(s)G_{p1}(s) + G_{c1}(s)G_{p1}(s)}{1 + G_{c1}(s)G_{p1}(s)} \tag{A.3}$$

$G_{m1}(s)$ is the first-order model of channel 1 which is the inverse of $G_{p1}(s)$ in the ideal case. Assuming $G_{m1}(s)G_{p1}(s) \approx 1$, to have an accurate regulation on the channel-1 current, $|G_{c1}(s)G_{p1}(s)| \gg 1$. Therefore, by increasing the gain of the controller (G_{c1}) at the operating frequency, the measured current approaches to the desired one. The PID block changes the desired voltage in a real-time fashion which results in a change in the duty cycle of PWM signals. This derivation can be extended to a MIMO controller with considering the mutual coupling.

The transfer function analysis reveals two things, (a) if the model of system can be determined exactly, there is no need for the feedback loop. However, in the real case, the imperfections and measurement errors affect the system which cannot be modeled, (b) considering mutual coupling in the system model is not compulsory and the feedback loop can compensate for it.

The whole control system was designed digitally using the Xilinx VC707 FPGA board. The PWM signals were generated with 15-bit resolution and duty cycles can be controlled in the range of picosecond. A home-built full-bridge power amplifier with 1MHz effective switching frequency is used to provide the desired voltages and currents at the output. The coil currents were measured by fluxgate current sensor (IT 205-S).

A.3 Results

To demonstrate the advantage of the proposed method, simulation results for two channels with 100A input current are compared using feed-forward only, feedback only, and a combination of feed-forward and feedback (Figure A.2). The second order behavior of a gradient coil with an amplifier is taken into account, and a 2% error is added to the model parameters to represent measurement errors. The Ziegler-Nichols method is used to tune PID coefficients. Figure A.2 shows that feed-forward alone cannot compensate for system uncertainties; feedback alone cannot correct rising and falling portions due to mutual coupling; however, feed-forward plus feedback provides nearly perfect regulation of output currents. Figure A.3 illustrate experimental results that are consistent with simulations. Due to hardware limitations, the experiments use a maximum current of 25A.

Image simulations are also performed to demonstrate the effectiveness of each

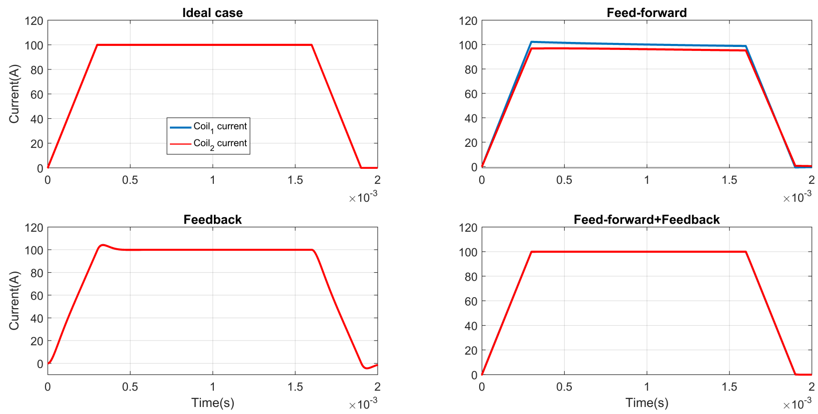

Figure A.2: Simulations: gradient coil current for feed-forward only, feedback only, and feed-forward+feedback controllers.

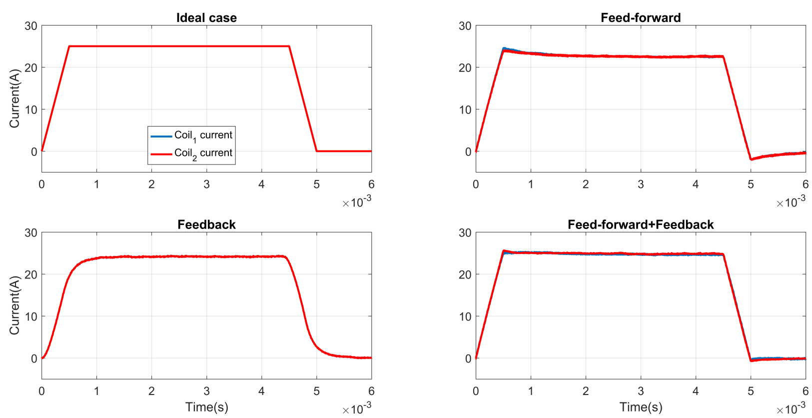

Figure A.3: Experiments: gradient coil current for feed-forward only, feedback only, and feed-forward+feedback controllers.

controller (Figure A.4). For this purpose, a gradient echo sequence (single slice) with the under test waveforms as a readout gradient is used. The maximum normalized error for feed-forward only and feedback only is 64% and 10%, respectively. However, for feed-forward plus feedback the maximum normalized error is 0.56%, which shows a significant improvement.

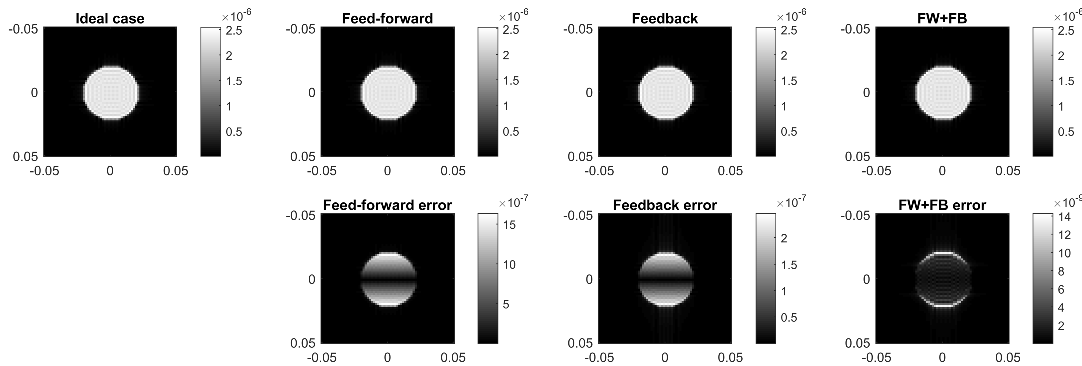

Figure A.4: Image simulations, ideal case and for each controller (first row), difference images (second row).

A.4 Discussion

In this work, to compensate the mutual coupling and undesired imperfections, a real-time digital PID controller design is proposed. The feedback loop in combination with the feed-forward PD model provides the desired voltage which has to be applied to the coils. The PID controller can adjust the PWMs duty cycle in order to minimize the error between the desired and measured current. Although adding PID can make the correction for the undesired distortions, the stability of the system has to be considered in the presence of the controller. To have a perfect current regulation, the gain of controller has to be high which may cause instability in the system or exceeds the GPAs limitation.

Appendix B

Design and Implementation of High Switching Frequency Gradient Power Amplifier Using eGaN Devices

Preface

The contents of this chapter were presented at the 29th Annual Meeting of International Society for Magnetic Resonance in Medicine [70]. The LC low pass filter is designed and tested by Soheil Taraghinia. The GPA functionality has been tested with the help of Volkan Acikel and Soheil Taraghinia.

B.1 Introduction

Switching H-bridge gradient power amplifiers (GPAs) are the most popular systems in the MRI scanners. The MR image quality highly depends on the fidelity of the output current. The pulse width modulation (PWM) switching frequency in a conventional GPA is about 100 kHz. This is achieved by interleaving multiple amplifier stages with IGBT modules or using new generation silicon carbide (SiC) switching devices and fewer power stages [66]. The attenuation of ripple currents and switching noises is necessary to prevent image quality degradation. Multiple stages of LC low pass filters, coupled-inductor-based ripple cancellation [71], and optimum-phase PWM signals [72, 73] are the most common methods to attenuate ripple currents. Recently developed gradient arrays and high order active shimming systems [84] draw attention due to their flexibility and promising applications. In this work, a single-stage gradient amplifier prototype with 150V/50A voltage and current ratings and 1MHz effective PWM frequency is put into practice by utilizing new generation e-mode gallium nitride (eGaN) power transistors. A single-stage LC low pass filter to attenuate the 1MHz ripple current is designed and implemented.

B.2 Methods

By the introduction of SiC and eGaN transistors, conventional designs, implementing IGBT or Si modules can be upgraded accordingly. Compared to SiC devices, eGaN transistors have the advantage of 3-5 times higher electron mobility [85]. The eGaN transistors can operate in high-voltage, high-temperature, and high-frequency reliability. Furthermore, a gradient array's power requirement is significantly less for each channel compared to conventional systems [15]. Therefore, we fabricated a 150V/50A one-stage full-bridge GPA for an insert gradient array system utilizing two parallel eGaN for high- and low-sides separately (Figure B.1). A center-aligned 500kHz PWM signal is used that results in a 1MHz effective PWM frequency. Floating supplies are designed for both high- and low-sides to supply gate-driver ICs. Deadtime between high side and low side switches are implemented to prevent shoot-through. A Virtex-7 family (VC707) evaluation board is used to generate high-resolution PWM pulses [67]. The half-bridge module is placed on a heat sink, which is air-cooled.

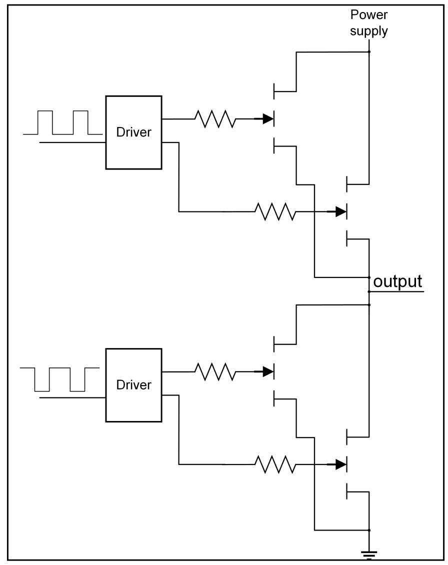

Figure B.1: Simplified circuit diagram of 150V/50A half-bridge for gradient array applications using eGaN transistors. Two parallel transistors are used as a switching element. Two of these modules are used for one full bridge driver.

The size of passive components, the amount of phase shift introduced to the control loop, the inductance value used in the filter compared to the inductance of the load, and simplicity are the essential filter design parameters. Figure B.2 depicts a single-stage differential LC filter used at the output of the H-bridge driver. Since the ripple current frequency is at 1MHz, the filter's cut-off frequency is adjusted to about 50kHz, allowing high bandwidth for gradient amplifier and sufficient ripple current attenuation.

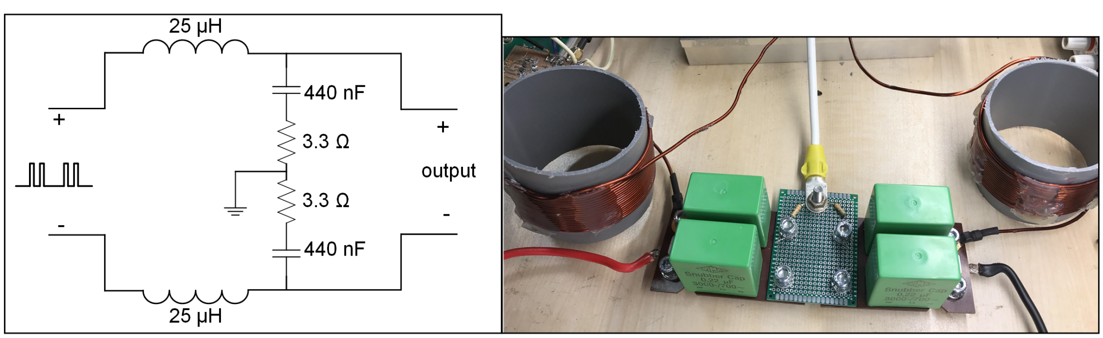

Figure B.2: Circuit diagram and fabricated differential one stage LC filter. Cut-off frequency is about 50kHz to attenuate ripple current with 1MHz frequency. Capacitor values are decreasing towards our switching frequency which degrades attenuation ratio.

B.3 Results

Figure B.3A shows the measured control PWM signals and switched 150V pulses at the H-bridge amplifier's output without load and LC filter at 1MHz effective frequency. In Figure B.3B, the thermal camera capture exhibits the transistors' temperature, indicating that the high switching did not reduce efficiency.

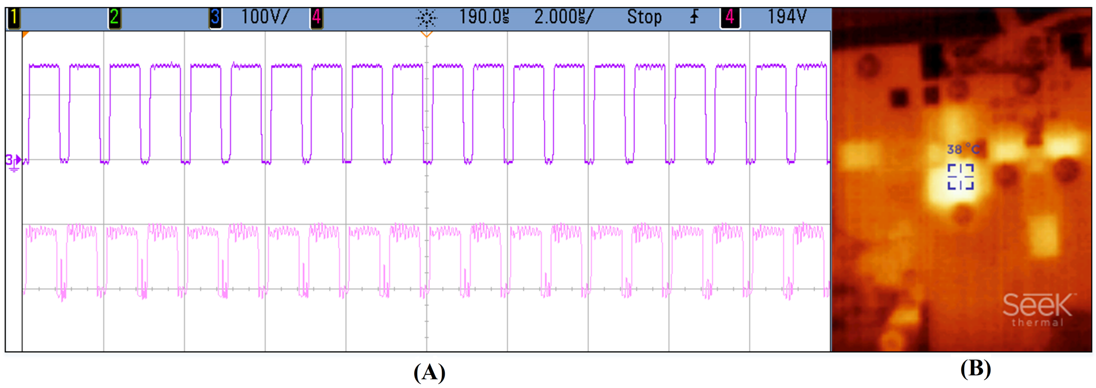

Figure B.3: (**A**) Measured PWM signals at the input (bottom) and output (top) of the H-bridge with 150V supply without load at 1MHz effective switching frequency. (**B**) Temperature increase of GaN transistors to 38°C from room temperature for about five minutes of operation condition in (A).

Figure B.4A depicts a trapezoidal current waveform flowing in a 410μH coil with 50A flat-top current and 200μs rise/fall time with filter. Temperature increase for five minutes of operation with a 10% duty cycle is shown in Figure B.4, indicating good thermal conductivity. Figure B.5 shows a zoomed version of the current and voltage waveform in Figure B.4 applied to the coil with and without an LC filter. Good ripple current attenuation and minimum gradient current distortion are achieved.

B.4 Discussion

In this work, the feasibility of using eGaN transistors for high switching frequency H-bridge current driver for gradient array applications was shown. Cascade and

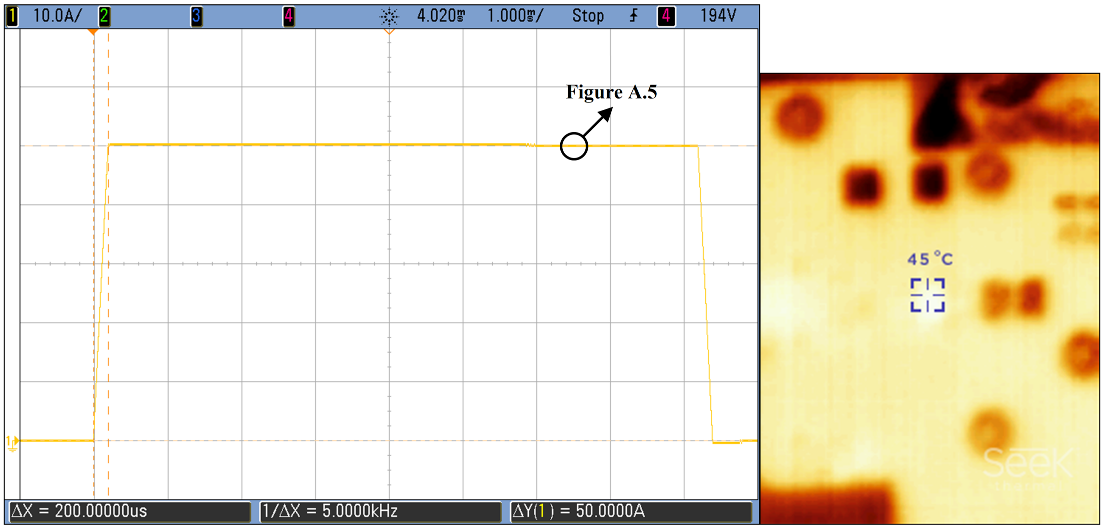

(A) **(B)**

Figure B.4: (**A**) Measured trapezoidal current waveform with 50A flat top amplitude and 0.25A/μs slew rate with filter. (**B**) Temperature of eGaN transistors to 45°C from room temperature for the current on (A) with 10% duty cycle and five minutes of operation. Zoomed version of the current is shown in Figure B.5

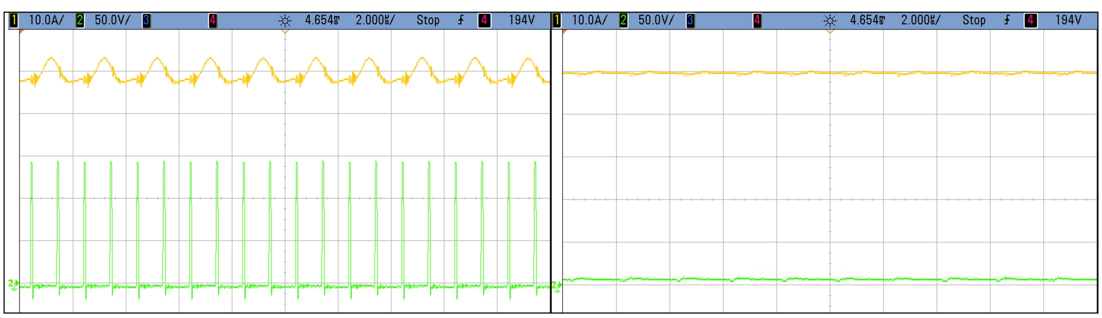

(A) **(B)**

Figure B.5: Zoomed current (top) and voltage (bottom) applied to the coil without (**A**) and with (**B**) filter. Peak-to-peak ripple current is reduced more than twelve times by using the LC filter. Small resistance of the coil (about 200$m\Omega$) requires small voltage levels and PWM duty cycle.

parallel configurations can be utilized in order to deliver higher current and voltage with high effective PWM frequencies. Although the fabricated H-bridge modules are designed to be capable of 400V/100A operation ratings, smaller ratings were tested to be on the safe side. Ripple currents with high frequencies resulted in moderate filter requirements. The voltage needed to achieve the desired slew rate is reduced due to smaller inductance values in the filter. The capacitors' self-resonance frequency must be high enough to maintain the filter's effectiveness at switching frequencies. Since the closed-loop control system was not utilized in this configuration, the filter's effect on the control loop was not evaluated, and it will be considered future work.